PLASMA SIMULATIONS OF EMISSION LINE REGIONS IN HIGH ENERGY ENVIRONMENTS

By

Chris T. Richardson

A DISSERTATION

Submitted to
Michigan State University
in partial fulfillment of the requirements
for the degree of

Astrophysics and Astronomy - Doctor of Philosophy

2013

ABSTRACT

PLASMA SIMULATIONS OF EMISSION LINE REGIONS IN HIGH ENERGY ENVIRONMENTS

By

Chris T. Richardson

This dissertation focuses on understanding two different, but in each case extreme, astrophysical environments: the Crab Nebula and emission line galaxies. These relatively local objects are well constrained by observations and are test cases of phenomena seen at high-z where detailed observations are rare. The tool used to study these objects is the plasma simulation code known as Cloudy. The introduction provides a brief summary of relevant physical concepts in nebular astrophysics and presents the basic features and assumptions of Cloudy. The first object investigated with Cloudy, the Crab Nebula, is a nearby supernova remnant that previously has been subject to photoionization modeling to reproduce the ionized emission seen in the nebula's filamentary structure. However, there are still several unanswered questions: (1) What excites the H_2 emitting gas? (2) How much mass is in the molecular component? (3) How did the H_2 form? (4) What is nature of the dust grains? A large suite of observations including long slit optical and NIR spectra over ionized, neutral and molecular gas in addition to HST and NIR ground based images constrain a particularly bright region of H_2 emission, Knot 51, which exhibits a high excitation temperature of ∼3000 K. Simulations of K51 revealed that only a trace amount of H_2 is needed to reproduce the observed emission and that H_2 forms through an uncommon nebular process known as associative detachment. The final chapters of this dissertation focus on interpreting the narrow line region (NLR) in low-z emission line galaxies selected by a novel technique known as mean field independent component analysis (MFICA). A mixture of starlight and radiation from an AGN excites the gas present in galaxies. MFICA separates galaxies over a wide range of ionization into subsets of pure AGN and pure star forming galaxies allowing simulations to reveal the properties responsible for their observed variation in ionization. Emission line ratios can constrain the spectral energy distribution, excitation mechanism, abundances and physical conditions present in these galaxies, while the large data set allows many weaker emission lines to be used as consistency checks. By integrating over a wide range of densities and radii from the excitation source, the variation in ionization for AGN can be represented as change in the central concentration of clouds in the NLR. Preliminary analysis from modeling star forming galaxies indicates that the same interpretation might apply to galaxies without an AGN in which gas is excited by starlight.

To my Bob.

ACKNOWLEDGMENTS

I would especially like to thank my adviser Jack Baldwin for his patience, his generosity, the clarity of his advice and his support of my career goals.

To Mom and Dad, Nan and Bob, you have all played a larger part in this dissertation than you will ever know.

To Carolyn, thank you for your never ending support and reassurance. Traveling through this process together has been unforgettable. By the way, we have cats.

To Brian O'Shea, thank you for your guidance, mentorship and candid advice throughout my graduate career.

To Gary Ferland, Ed Loh, James Allen, Paul Hewett, Charles Kuehn, Andy Fabian and Philippe Salomé, thank you for your hard work and dedication to these projects.

To my friends, thank you for your support and years of laughter.

Thank you to the Michigan State University High Performance Computing Center and the Institute for Cyber Enabled Research for providing the computational facilities and support necessary to run many of the models in this work.

Thanks to Christopher Waters for the LaTeX class used to format this dissertation.

TABLE OF CONTENTS

LIST OF TABLES

LIST OF FIGURES

1 A Brief Introduction to Nebular Astrophysics

This chapter is meant to give a brief overview of the main physical concepts in nebular astrophysics needed to understand subsequent chapters: photoionization equilibrium, thermal equilibrium and emission line diagnostics. These concepts were developed many decades before this work and therefore this summary draws upon the more complete introductions presented in several textbooks including Spitzer (1978), Tielens (2005), Osterbrock & Ferland (2006). Certain physical processes, such as hydrodynamics, are omitted or briefly presented for simplicity and so the reader is urged to seek these references and others for a more complete understanding. The astrophysical code known as Cloudy has long been the industry standard for self-consistently incorporating all of these physical processes, and many more, to model gaseous clouds over a vast range of ionization and physical conditions and predict the emitted spectrum. A brief summary of the assumptions, reliability and user input for Cloudy are introduced.

1.1 Photoionization Equilibrium

Photoionization equilibrium or the balance between photoionization and recombination of ions with electrons determines the ionization structure of nebulae. The generalized equation for photoionization equilibrium is

$$n(X^i) \int_{\nu_i}^{\infty} \frac{4\pi J_\nu}{h\nu} a_\nu(X^i) d\nu = n(X^{i+1}) n_e \alpha(X^i, T) \quad [\mathrm{cm}^{-3}\ \mathrm{s}^{-1}] \tag{1.1}$$

where X^i is an element X with ionization i, ν_i is the ionization threshold frequency, J_ν is the mean intensity, a_ν is the ionization cross section and α is the recombination coefficient. The left side of the equation give the volumetric photoionization rate, or the number density of X^i atoms multiplied by the ionizing flux and photoionization cross section. This is balanced by the right side of the equation, which represents the volumetric recombination rate, or number density of X^{i+1} multiplied by the electron density and the recombination coefficient. Note, the incident radiation field sets the photoionization rate while the temperature sets the recombination rate. To a rough approximation $\alpha \sim T^{-1}$, so as the temperature decreases the rate of recombination increases.

Photons with $\lambda < 512$ Å or $h\nu > 13.6$ eV ionize hydrogen and originate from a variety of objects including the surface of hot stars (e.g. O stars), pulsars generating synchrotron emission, and radiation from active galaxies. Hydrogen is by far the most abundant element in the universe and its simplicity allows a relatively basic physical treatment that can provide insight about the typical scales in nebular astrophysics. If we consider a pure hydrogen nebula, Equation 1.1 gives,

$$n(\mathrm{H}^0) \int_{\nu_i}^{\infty} \frac{4\pi J_\nu}{h\nu} a_\nu(\mathrm{H}^0) d\nu = n_p n_e \alpha(\mathrm{H}^0, T) \tag{1.2}$$

where the proton (H_0) number density $n_p = n_e$. From the Einstein coefficients we can see that the lifetime of an electron in an excited level of hydrogen is $1/A_{ij} = t_{ij} \sim 10^{-8} - 10^{-4}$ s. If we evaluate the left side of Equation 1.2 for a typical nebula, the photoionization timescale, t_{photo} is $\sim 10^8$ s for the $1\mathrm{s}^2\mathrm{S}$ ground state, therefore, to first approximation, all photoionizations of hydrogen are from the $1\mathrm{s}^2\mathrm{S}$ ground state.

The recombination timescale for the 1s^{2}S level is given by

$$t_{rec} = \frac{1}{n_e \alpha(\mathrm{H}^0, T)} \tag{1.3}$$

where $n_e \sim 10$ cm^{-3} and $\alpha \sim 2.0 \times 10^{-13}$ cm^{-3} s^{-1} for a typical completely ionized nebula with $T \sim 10^4$ K. This gives $t_{\mathrm{rec}} = 5 \times 10^{11}$ s or approximately 10^4 years, so a freshly ionized hydrogen atom will remain ionized for quite some time before recombining with a free electron, only to quickly be ionized again. It follows under these conditions that the neutral fraction of hydrogen will be very small and therefore these regions are called H II regions, where H II stands for H$^+$. Electrons in H II regions thermalize to a Boltzmann distributions very quickly since the cross section for $e^- + e^-$ is orders of magnitude larger than that for photoionization. Typical elastic $e^- + e^-$ timescales are

$$t_{e,e} \approx 10^4 \left(\frac{E_e}{1\mathrm{eV}}\right)^{3/2} \frac{1}{n_e} \quad [\mathrm{s}] \tag{1.4}$$

where E_e is the energy of the electron. Taking the values above, $n_e \sim 10$ cm^{-3} and $T \sim 10^4$ K, we get $t_{e,e} \sim 10^3$ s which is much shorter than both the photoionization and recombination time.

The mean free path of an ionizing photon is roughly the size of a typical H II region. We can parameterize the neutral fraction by defining ξ such that $n(\mathrm{H}^0) = \xi n(\mathrm{H})$. When the bulk of the ionized hydrogen begins to transition to neutral hydrogen, we can take $\xi = 0.5$. The mean free path can then be evaluated as

$$l \approx \frac{1}{n(\mathrm{H}^0) a_\nu} \tag{1.5}$$

where $n(\mathrm{H}^0) = 5$ cm^{-3}, since $n(\mathrm{H}) = 10$ cm^{-3}. For the 1s^{2}S ground state ionization cross section for hydrogen is $\sim 6 \times 10^{-18}$ cm^{-2}. Evaluating the mean free path gives $l \sim 3 \times 10^{16}$ cm which is a typical size of an H II region. Thus after this depth, ionizing photons will on average be absorbed and the hydrogen transitions from ionized to neutral.

1.2 Thermal Equilibrium

The overwhelmingly dominant heating mechanism in nebulae and emission line galaxies occurs through photoionization of H and He. Photons with energy $h\nu$ ionize atoms with an ionization potential $h\nu_0$, which produces a photoelectron with energy $h(v-v_0)$. As shown in the previous section, this photoelectron then elastically collides with thermal electrons. Every photoionization is followed by a recombination, which cools the gas. Therefore the energy difference between an ionizing photoelectron and the photons released during recombination with a thermalized electron, including the subsequent cascade of the captured electron to the ground state, represents the net energy injected into the gas by photoionization.

Assuming photoionization equilibrium, representing this numerically we have

$$Q_{net} = \frac{3}{2}kT_i n_e n(X^i)\alpha(X^i,T) - n_e n(X^i)kT\beta(X^i,T) \quad [\text{erg cm}^{-3}\ \text{s}^{-1}] \tag{1.6}$$

where β is recombination cooling coefficient, which depends on the recombination cross section. The heating and recombination cooling rates are proportional to the number densities of each ion; therefore heavy elements can be omitted from these processes due to their low abundances relative to H and He, and $Q_{net} \approx Q_{net}(\text{H}) + Q_{net}(\text{He})$.

However in spite of their low abundance, cooling from ion $-$ electron collisions of heavy elements is important to the overall thermal structure due to their low ionization potential. Other collisions, such as ion $-$ ion and ion $-$ proton, are inefficient due to coulomb repulsion. Collisions between electrons and ions are efficient for metals and make the largest contribution to overall cooling in nebulae.

It is simplest to consider a two level atom. Even with this simplification, the details of collisionally excited line radiation are complex and therefore we will jump straight to the final form of the cooling rate to consider the implications of this form of cooling. The cooling rate from collisions is then,

$$C = n_e n_1 h\nu_{21} \frac{\omega_2}{\omega_1} e^{-h\nu_{21}/kT} \left(1 + \frac{n_e q_{21}}{A_{21}}\right)^{-1} \tag{1.7}$$

where $h\nu_{21}$ is energy required raise the electron from level 1 to level 2, q_{21} is the rate coefficient [cm^3 s^{-1}], ω_1 and ω_2 are the statistical weights for levels 1 and 2 respectively, and A_{21} is Einstein coefficient for spontaneous emission. As $n_e \to 0$, all collisions are followed by radiative de-excitations and collisional de-excitation is unimportant. However as $n_e \to \infty$, collisional de-excitation is non-negligible and suppresses the cooling rate. In this limit, the cooling rate is simply the thermal equilibrium value.

The physical meaning from all of this is that electrons collide with metal ions, which excites the bound electrons to higher energy states. If the electron density is low enough then an excited electron de-excites to a lower energy state and the emitted photon escapes the nebula, thereby cooling the gas. This is called the low-density limit (LDL). But, if the electron density is high enough, then a second free electron could collide with an excited ion and cause collisional de-excitation. In this case, the second free electron carries the energy back into the gas and there is no net cooling in the nebula. This is called the high-density limit (HDL).

For a two level atom, the transition from LDL to HDL is defined by,

$$n_{\text{crit}} = \frac{A_{21}}{q_{21}} \tag{1.8}$$

where n_{crit} is the critical density. So, high densities are defined as any density above the critical density, where collisionally excited line emission is suppressed. After this limit, any further increases in ne will have a reduced impact on emission compared to increases in n_e below the critical density.

Finally, the highly simplified final form of thermal equilibrium in most nebulae can be thought of as $Q_{net}(\mathrm{H}, \mathrm{He}) \approx C(\text{metals})$ where $Q_{net}(\mathrm{H}, \mathrm{He})$ is the net heating rate from H and He after taking into account recombination cooling, and $C(\text{metals})$ is cooling rate from metals due to electron $-$ ion collisions.

1.3 Physical Conditions from Observations

In nebular astrophysics, understanding phenomena is often characteristic of the inverse problem in astronomy: we know the emitted spectrum and we want to know the conditions that are able to produce it. Emission line ratios can probe several properties of nebulae, but covering all of these properties in detail is beyond the scope of this introduction. However, constraining electron temperatures and electron densities using emission line ratios are two techniques used in the following chapters, so we discuss them here.

As mentioned in Section 1.2, the ground states of metal ions are populated due to collisional excitation. For a given ion, upper levels with differing excitation energies but with similar critical densities give rise to a temperature indicator. Specifically, the upper levels of O III (i.e. O^{++}) and N II are observed in the optical and are the most common indicators of nebular temperature. For example, the [O III] λ4363 line populates an upper level while [O III] λ4959 and [O III] λ5007 (the ratio of which is fixed by atomic physics) populate an intermediate level. Therefore, the ratio [O III] λ4363 / [O III] $\lambda\lambda$4959, 5007 constrains the electron temperature. Plugging in the necessary atomic data for these lines we find,

$$\frac{j_{\lambda 4959} + j_{\lambda 5007}}{j_{\lambda 4363}} = \frac{7.90 e^{3.29\times 10^4/T}}{1 + 4.5 \times 10^{-4} n_e T^{-1/2}} \tag{1.9}$$

where j represents the emissivity [erg s^{-1} cm^{-3} sr^{-1}] of each respective emission line. As expected, this ratio is highly sensitive to the temperature and weakly dependent on the electron density.

Conversely, an ion with similar upper level excitation energies but differing rate coefficients or spontaneous emission coefficients gives rise to an electron density indicator. One example of this occurs with the emission lines [S II] λ6716 and [S II] λ6731. In LDL ($\sim$ 10^2 cm^{-3}), the ratio [S II] λ6716/λ6731 is simply a constant determined by the ratio of their statistical weights, $\omega_{6716}/\omega_{6731} = 1.5$. The statistical weight signifies how many electrons a level can hold. The [S II] ratio is greater than unity, since [S II] λ6716 has a larger statistical weight and, in the case of LDL, collisional de-excitations are unimportant. In HDL ($\sim$ 10^5 cm^{-3}), the [S II] ratio is also constant, but now collisional de-excitation does play role and thus the radiative transition probabilities do as well. Now, the constant is determined by $(\omega_{6716}A_{6716})/(\omega_{6731}A_{6731}) = 0.44$.

Therefore, between LDL and HDL, the [S II] ratio smoothly decreases from a constant value to smaller constant value. In between these limits, the electron density can be inferred from the observed [S II] ratio. As the electron density increases from LDL, the [S II] λ6731 emission line becomes stronger relative to [S II] λ6716 since the lifetime of an excited electron is smaller for the transition resulting in the [S II] λ6731 emission line. Eventually however, the density becomes high enough that both [S II] lines have Boltzmann populations and thus their ratio approaches a constant.

1.4 Plasma Simulations with Cloudy

Cloudy (Ferland et al. 2013)[1] is an open source, plasma simulation code that self-consistently calculates the ionization, thermal and chemical structure of an astrophysical cloud and, most importantly, predicts the emitted spectrum. Cloudy can reliably simulate an astrophysical plasma with temperatures in the range of $10^0 - 10^8$ K and densities in the range $10^{-9} - 10^{15}$ cm^{-3}. For temperatures above 10^8 K, electrons and ions decouple and this functionality is currently not included in version c10.00.

Cloudy assumes that the gas considered is in steady state. This is usually an accurate assumption for temperatures above 10^4 K. The recombination timescale is generally much longer than the ionization or electron thermalization timescale and yet is still much shorter than the age of the nebula in question. However, in molecular regions, reaction timescales such as those for associative detachment (Section 2.4.2) can be longer than the age of the nebula indicating that a time dependent calculation is needed.

Cloudy divides the cloud into many zones, in each of which the physical conditions are approximately constant. The equations governing conservation of energy, conservation of charge and statistical equilibrium are solved self-consistently with a minimal set of free parameters. Thus, a large set of observables is generated with the parameters usually constrained by observations. Only the chemical composition, shape and intensity of the incident radiation field, geometry, equation of state and boundary conditions must be specified to initiate a simulation. The boundary condition criterion often entails a temperature, column density or cloud thickness restriction.

Simulations with Cloudy can be performed in several seconds or can take several days, depending on the complexity of the atoms and molecules included. The advent of high performance computing allows the computation of massive grids of plasma

---

[1] http://www.nublado.org/

simulations at the price of a single simulation. Cloudy comes equipped with an "embarrassingly parallel" mode that allows a single model to run every computer core supplied. When simulations finish running, new simulations still in the queue run on newly available cores resulting in a very simple yet efficient algorithm. The simulations presented in the following chapters relied heavily on this functionality.

2 The Nature of the H_2 Emitting Gas in the Crab Nebula

Understanding how molecules and dust might have formed within a rapidly expanding young supernova remnant is important because of the obvious application to vigorous supernova activity at very high redshift. In previous papers we have mapped the Crab Nebula in a roto-vibrational H_2 emission line, and then measured the molecular excitation temperature for a few of the brighter H_2-emitting knots that we have found to be scattered throughout the Crab Nebula's filaments. We found that H_2 emission is often quite strong, correlates with optical low-ionization emission lines, and has a surprisingly high excitation temperature. Here we study Knot 51, a representative, bright example. It is a spatially isolated structure for which we have available long slit optical and NIR spectra covering emission lines from ionized, neutral, and molecular gas, as well as HST visible and SOAR Telescope NIR narrow-band images. We present a series of Cloudy simulations to probe the excitation mechanisms, formation processes and dust content in environments that can produce the observed H_2 emission. There is still considerable ambiguity about the geometry of Knot 51, so we do not try for an exact match between model and observations. Rather, we aim to explain how the bright H_2 emission lines can be formed from within a cloud the size of Knot 51 that also produces the observed optical emission from ionized and neutral gas. Our models that are powered only by the Crabs synchrotron radiation are ruled out because they are not able to reproduce the observed strong H_2 emission coming from thermally populated levels. The simulations that come closest to fitting the observations (although they still have conspicuous discrepancies) have the core of Knot 51 almost entirely atomic with the H_2 emission coming from just a trace molecular component, and in which there is extra heating. In this unusual environment, H_2 forms primarily through H^- by associative detachment rather than by grain catalysis. In this picture, the 55 H_2-emitting cores that we have previously catalogued in the Crab have a total mass of about 0.1 $M_\odot$, which is about 5% of the total mass of the system of filaments. We also explore the effect of varying the dust abundance. We discuss possible future observations that could further elucidate the nature of these H_2 knots.[1]

2.1 Introduction

The Crab Nebula (hereafter "the Crab) presents a unique opportunity to study not only the properties and evolution of a very young supernova remnant which is not yet interacting with the ISM, but also in a more general way the details of the physical processes that occur in filamentary condensations exposed to a harsh environment of high-energy photons and particles. The relative proximity of the Crab, at a distance $d \sim 2.0$ kpc (Trimble 1968), and the well-known date of the explosion, 1054 A.D. (Duyvendak 1942; Mayall & Oort 1942), allow detailed observations and constraints. The Crab filaments have been the subject of many previous investigations (see the review articles by Davidson & Fesen 1985 and by Hester 2008). The Crabs synchrotron radiation field has been taken into account as the energy source for the emitting regions, but not the effects of the high-energy particles that must also be present. Most of this previous work has concentrated on the ionized gas, generally with the aim of using optical emission lines to measure the chemical abundances in the aftermath of the supernova explosion. H_2 molecules are also present in the Crab, as was shown by the pioneering infrared observations and spectroscopy by Graham,

---

[1] This chapter is almost entirely taken word for word from Richardson et al. (2013a)

Wright & Longmore (1990; hereafter G90). Those measurements were made with quite low (20" FWHM) angular resolution in just three locations.

We have been carrying out a much more detailed study of the molecular content of the Crab, mapping most of the nebula at sub-arcsec angular resolution in the NIR H_2 2.12 μm emission line, and tying those results together with both existing and new spectra and images over a wide range of wavelengths. In our first paper in this series (Loh, Baldwin & Ferland 2010; hereafter Paper I), we investigated the brightest H_2 feature, Knot 1, for which the molecular content was estimated to be M_{mol} 5×10^{-5} $M_{\odot}$. We arrived at this estimate under the assumption that the H_2 emission is collisionally excited in a predominately molecular core. Then, in Loh et al. (2011) (hereafter Paper II) we presented our full near-infrared imaging survey made with the Spartan Infrared Camera on the 4 m SOAR telescope. We detected 55 compact (1-2" diameter) knots, spread across much of the face of the Crab, that radiate strongly in the H_2 2.12 μm line. We showed that the positions of these knots correlate strongly with compact, low-ionization regions that are conspicuous in Hubble Space Telescope (HST) [S II] $\lambda\lambda$6720 images; [S II] and also [O I] are H_2 tracers. The low-ionization regions are found on or next to the bright filaments seen in higher ionization lines such as [O III] λ5007. We used optical spectra to measure radial velocities of most of the [S II] features. Then in Paper III in this series (Loh et al. 2012), we used K-band spectra to measure the H_2 excitation temperature of 7 of the brightest knots. From the ratio of the S(1) 2-1 and S(0) 1-0 lines we found T_{exc} $2000 - 3000$ K, which we argue is also the kinetic gas temperature in the regions where H_2 lines form under the conditions present in the Crab (Ferland 2011). These temperatures are just below the dissociation temperature of H_2.

There is also dust in the Crab, as can be seen both from the weak thermal dust emission peak at 80 μm in the Crabs continuum spectrum (Marsden et al. 1984), and from the presence of many small dust globules seen in silhouette against the

Crabs synchrotron continuum (Fesen & Blair 1990, Hester et al. 1990). The mass of dust in the filaments is uncertain, ranging from 10^{-3} $M_\odot$ (Temim et al. 2006, 2012; Hester 2008) to 0.2 $M_\odot$ (Gomez et al. 2012). However, the gas to dust ratio could vary considerably between the filament cores and the ionized gas, and different regions could have both different abundances and different dust-to-gas ratios. Sankrit et al. (1998) estimate a dust-to-gas mass ratio in the cores that is a factor of 10 above the ISM value.

The ionized, neutral and molecular gas and the dust are distributed throughout a complex system of filaments that extend down into the synchrotron plasma and hence must be bombarded from all sides by intense synchrotron radiation and also by the high-energy particles that emit the synchrotron radiation. A more complete understanding of the nature of these filaments and condensations would shed light on a number of open questions including: (1) What is the excitation process that produces the strong molecular hydrogen emission? Photoionization, shocks, dissipative MHD waves, and high-energy particles are all possible energy sources. (2) What are the properties of the grains that formed in the cores of the filaments? The Crab serves as a test bed for understanding grain formation in high-redshift galaxies where short-lived massive stars and supernovae must produce the observed dust. (3) What are the molecular processes that occur in this hostile environment? In the ISM H_2 commonly forms by grain catalysis, a process dependent on temperature and composition of the grains, but is that true in an environment like the Crab? Many H_2 knots do not show dust extinction. Could H_2 form without dust? (4) What is the true mass of the filaments? Molecular gas is less emissive than ionized gas and thus the molecular regions of the filaments could contain a substantial amount of mass. (5) The Crab filaments appear to be nearby, well-resolved prototypes of the physically much larger filaments seen in the IGM of cool-core galaxy clusters (Fabian et al. 2008). Both show a low-ionization spectrum, have similar geometries, and are surrounded by ionizing particles. The Crab can serve as a test bed for understanding the physics of the cluster filaments.

In this paper, we explore the physical conditions in the gas that produces the H_2 emission. We aim to build on the pioneering first look at this problem by G90. Our approach is to fit photoionization models, supplemented by other sources of heating and ionization, to our extensive observations of a single knot, using the plasma simulation code Cloudy (Ferland et al. 1998) to explore the H_2 excitation mechanisms, formation processes, level populations and the role of dust in the molecular core.

While previous studies have addressed the structure of ionized skins on the filaments (Pequignot & Dennefeld 1983, Sankrit et al. 1998), none have included the molecular cores. In addition, our observations provide us with more detailed constraints than have been used in previous modeling efforts. Many papers have explored a wide range of possible abundances and argued that point-to-point abundance variations within the Crab filament system are quite plausible (e.g. Davidson 1978; Davidson 1979; Pequignot & Dennefeld 1983; Henry and MacAlpine 1982; MacAlpine and Satterfield 2008; Satterfield et al. 2012). Our study uses a wider variety of optical emission lines and focuses on a more spatially compact feature (a knot) than the filaments considered in other papers.

The brightest H_2 knot in our catalog, Knot 1, is not the best candidate for this study. It suffers from lying in a confused region of the Crab. It is immediately adjacent to, and probably physically associated with, the much more extensive bright highly-ionized filament FK-10 (Fesen & Kirshner 1982), but FK-10 does not have strong H_2 emission while Knot 1 is not at all conspicuous in high ionization lines such as [O III] $\lambda5007$ (Paper I). It is unclear where the boundaries lie between these two rather different types of emission regions. In addition, the radial velocities determined from our long-slit optical spectra show that there is considerable other material at different points along the same line of sight, and that the strong [S II] emission from

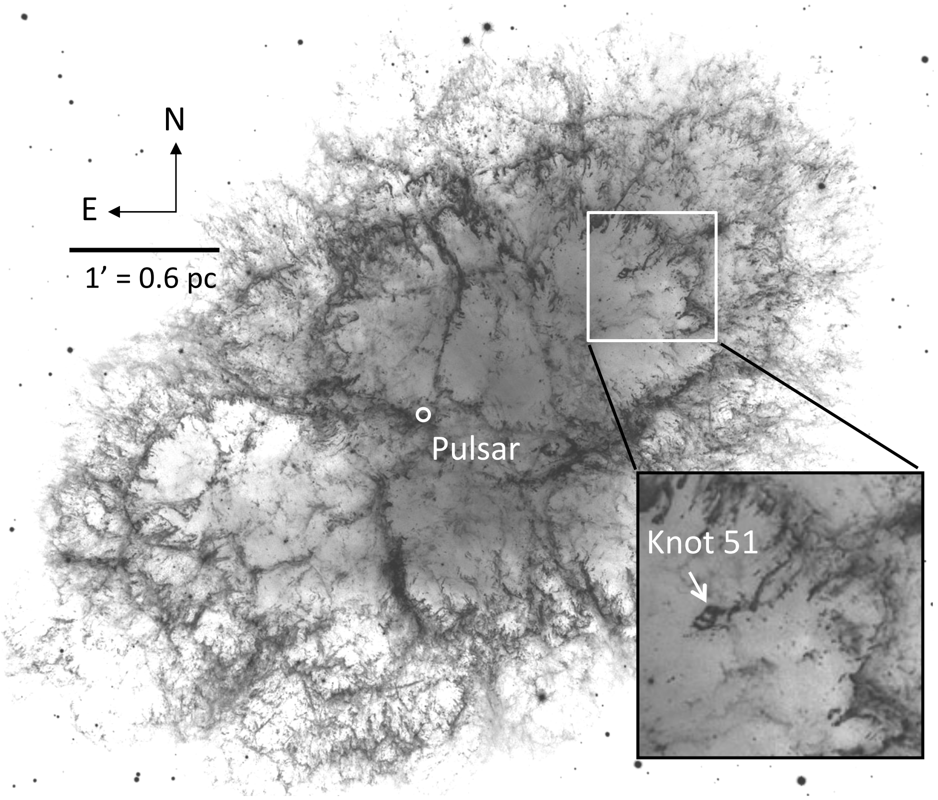

Figure 2.1 Positions of Knot 51 and the pulsar, shown on grey-scale rendering of the well-known HST composite color image made with F502N, F631N and F673N filters (courtesy of NASA, ESA and J. Hester, Arizona State University; StScI News Release 2005-37).

Knot 1 comes from material with a very complex velocity field.

We instead study a much simpler region, Knot 51 (K51) from our catalog in Paper II. Figure 2.1 shows that K51 lies near the tip of a long tendril of filamentary gas. Both K51 and the tendril have small radial velocities, indicating that they lie approximately halfway through the nebula, where the direction of expansion is in the plane of the sky. The tendril is actually a pair of elongated features extending back down into the synchrotron plasma from one of the large-scale filaments that wraps around the outer surface of the synchrotron plasma. The two join into a single tendril before reaching K51. As we discuss below, the velocity structure in this region shows that there is minimal contamination from foreground or background filaments. The situation is still not ideal, because as is described below there is a second H_2 knot immediately adjacent to K51 that is part of the same filament, but this is the cleanest case that we can find.

The following sections first present the available observations of K51, and then describe a series of Cloudy models that explore a large parameter space with the goal of reproducing the observed H_2 2.12 μm emission along with the observed lines of neutral and ionized atomic species. We do not aim to produce an accurate model of the knot, in part because the existing observations do not uniquely specify the geometry of the molecular region (higher spatial resolution data are needed) or reveal the total molecular inventory (sub-mm observations are needed). Rather, this paper is a plausibility study whose goal is to identify what general type of model can account for the existing suite of observations. The observations of ionized and neutral species in K51 serve as a guide to the overall structure of a typical condensation, but in spite of being the simplest case, K51 is still a rather complicated structure for which we do not attempt to fit all details of the observations.

In our previous papers we had assumed that the H_2 emission comes from a predominantly molecular core of some type. The simulations presented here show that in the unusual environment of the Crab it is instead possible that the observed H_2 emission can be produced by a trace H_2 component in what is basically a very extended H^0 zone. Although dust is clearly present in the particular case of K51, grains are not actually required to form H_2 in this environment, because of the high electron density where atomic hydrogen is present, which results in an enhanced efficiency of the H^- route. Finally we outline the types of observations that would be needed to further constrain physical models of the atomic or molecular regions.

2.2 Observational Data

We assembled a wide variety of observations of K51 in order to constrain the nature of its ionized, neutral and molecular gas, and its dust content. These include space- and ground based images at visible, near-infrared (NIR) and mid-infrared wavelengths, together with ground-based visible and NIR spectra.

2.2.1 Narrow-Band Emission Line Images

Figure 2.2 shows a series of visible and NIR images, all on the same scale, in boxes covering the same 10" (0.097 pc) square patch on the Crab. These are magnified images of the region shown in the insert on Figure 2.1. They include K51 as well as Knot 50, which lies 3.4" away. The pair of small white crosses on each image mark the position of the peak H_2 emission from the two knots.

The H_2 image is in the 2.12 μm line and is from our data described in Papers I and II, taken with the Spartan Infrared Camera on the SOAR Telescope. It has 0.7" FWHM angular resolution. The [S II] $\lambda\lambda$6716+6731, [O I] λ6300, [O III] λ5007, Hβ and continuum images are from HST archival data in which the 0.1" pixels undersample the HST point spread function. Since the Crabs expansion causes significant proper motion of the knots, for each filter we have only summed together HST data taken at a single epoch (Table 2.1). Following the procedure described in Paper II, the world coordinate system of each co-added HST image was then rescaled around the center of the Crab's expansion to adjust it to the same epoch (2009 Dec) as our ground-based H_2 images. This allows for an accurate comparison of the Knots morphology as seen at different wavelengths, smeared only by actual time evolution of its internal structure.

The HST continuum image will be discussed below. The emission-line images in Fig 2.2 show that in H_2 emission, K51 appears slightly elliptical with a roughly Gaussian surface brightness distribution. The [O III] emission has a conspicuous hole

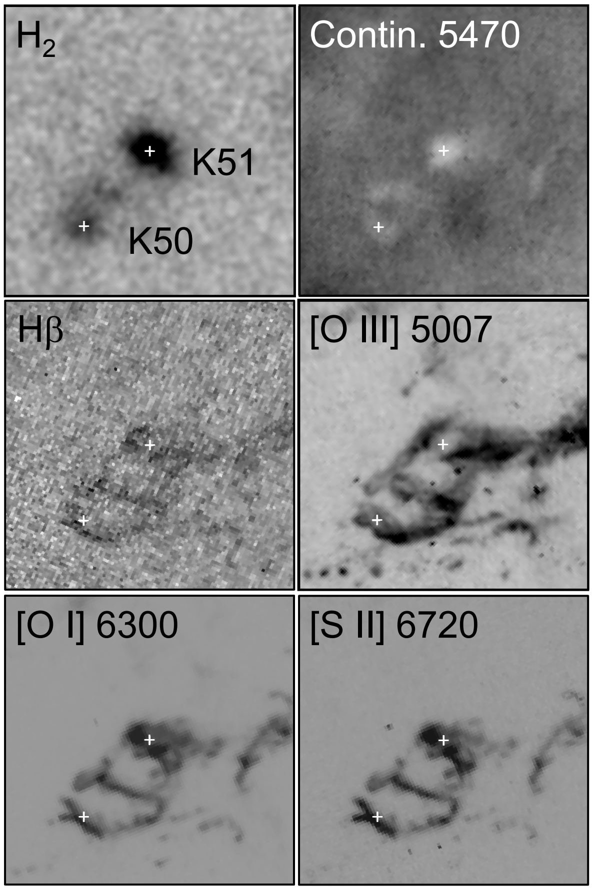

Figure 2.2 Images of Knots 50 and 51 through various filters. All boxes are 10"×10" and cover the same area on the sky with N up and E to the left. The pair of small white crosses on each image mark the position of the peak H_2 emission from the two knots. The H_2 image is from our ground-based imaging, the others are HST archival images. The [S II] $\lambda\lambda$6720 and [O I] λ6300 emission traces the H_2 2.12 μm emission.

at the position of the H2 centroid and a pair of bright patches on opposite sides of that hole, and then is strong along the filament that runs up to the north-west to join onto the main system of high-ionization filaments seen in Figure 2.1. The Hα, [S II] and [O I] images all not only show the same structure to either side of the molecular core that is seen in the [O III] image, but also have emission from the position of the H_2 central core. This follows the general pattern reported by Sankrit et al. (1998) and others, in which low-ionization cores are surrounded by more extended high-ionization halos.

Table 2.1: Archival HST Images

Line	Filter	No. Images	Total Expo. (s)	Dates
Hβ	F487N	2	4000	1994 Feb 2
[O III] λ5007	F502N	2	5200	2000 Jan 26
[O I] λ6300	F631N	2	3900	2000 Jan 26
[S II] λ6720	F673N	2	2600	2000 Jan 26
Continuum	F547N	2	11600	1994 Mar - 1995 Dec

In addition, all of the visible-wavelength lines are also emitted by a circular ring to the SE (lower left in Figure 2.2) of K51 that includes H_2 Knot 50 on the ring's far edge, and additional fainter H_2 emission from along the ring.

2.2.2 Spectra

Our grid of long-slit optical spectra taken with the Kitt Peak National Observatory (KPNO) 2.1 m telescope covers Knots 50 and 51 (Paper II). The spectrum covers the wavelength range $\lambda\lambda$3700-7400 Åat 6.3 Åresolution, with a 3.8" slit width and 2.7" FWHM resolution along the slit. Figure 2.3 (left panel) shows the slit position of the spectrum that crosses Knots 50 and 51, and next to it (in the center two panels) on the same spatial scale are two segments of our KPNO 2D spectrum, showing the various velocity systems in that region of the Crab. Our NIR spectrum across the two knots (from Paper III) is shown in the right-hand box.

The emission lines from Knots 50 and 51 have the same radial velocities, v_{helio} 130 km s^{-1}. Regions along the slit close to the two knots also show emission, especially in [O III], from the front and rear sides of the Crab's expanding shell with v_{helio} roughly ± 1000 km s^{-1}. The blueshifted component of this additional gas falls outside the HST passbands for the emission-line images. The +1000 km s^{-1} component will

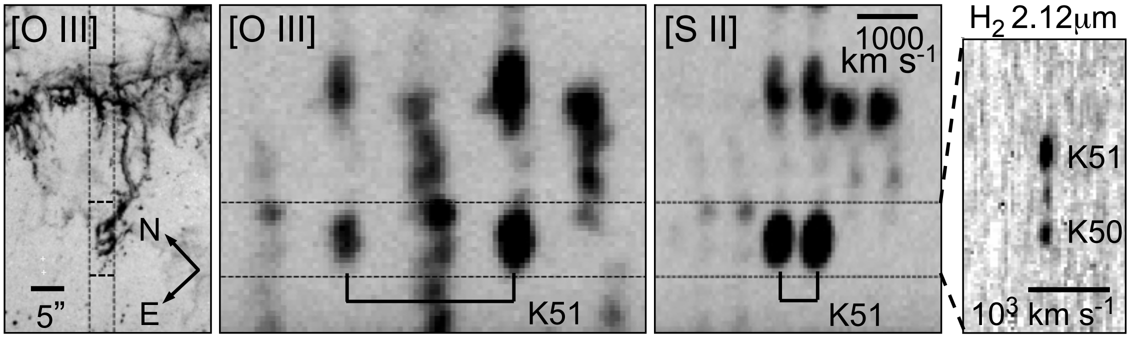

Figure 2.3 HST [O III] image (left panel) with vertical lines showing the area covered by our KPNO spectrum with its 3.8” wide slit. The two small white crosses mark the positions of Knots 50 (lower) and 51 (upper). Portions of the KPNO spectrum are shown in the middle two panels, aligned vertically with the HST image. The 11.2” region extracted along the slit is indicated by the horizontal lines, and the solid-lined goal posts mark the wavelengths of the [O III] $\lambda\lambda$4959, 5007 and [S II] $\lambda\lambda$6716,6731 doublets from Knot 51 (blended along the slit with Knot 50). The velocity scale is the same in the two central panels, with velocity increasing to the right. Our NIR spectrum, taken through a 0.4” wide slit and with the scale on the sky magnified relative to the other images, is shown in the right panel. The higher spatial resolution of the NIR spectrum clearly separates Knots 50 and 51, and shows that they have the same radial velocity.

contribute to the line emission seen in the HST images, but the line-of-sight to K51 is relatively uncontaminated. The spectrum shows that Knots 50 and 51 are at nearly the systemic velocity of the Crab. In addition, where adjacent KPNO slit positions not shown here cross parts of the long double-tendril of emission reaching down to K51 from the NW, the spectra show that the gas all along that tendril has the same radial velocity as K51. From this we deduce that Knots 50 and 51 and the tendril are all part of the same physical structure that is moving mostly in the plane of the sky, and therefore must lie very close to halfway through the overall Crab Nebula.

Knots 50 and 51 are not spatially resolved in our optical spectrum, so we measured them together by extracting a 1D spectrum that covers the 11.2 arcsec region along the slit marked on Figure 2.3. We also extracted spectra over smaller lengths along the slit trying to isolate Knots 50 and 51, and confirmed that those spectra do not have any major differences between them in their emission-line intensity ratios. Here we have chosen to use the combined spectrum because we know that we have included the total flux from the sum of the two knots.

The measured line strengths relative to Hβ and the Hβ flux are listed in Table 2.2. The table also lists line strengths corrected for reddening assuming $A_V = 1.46$ mag (Davidson & Fesen 1985) and a standard Galactic extinction curve. This dereddening is intended to remove the effects of extinction from the ISM along our line of sight to the Crab. The resulting Hα/Hβ ratio is 2.96, very close to the Case B value, implying that there is little additional internal reddening of the Balmer lines. The last column of Table 2 lists the estimated percentage uncertainties for the lines measured from the KPNO spectrum, including the effects of blending, sky subtraction and systematic error in the flux calibration in addition to the pixel-to-pixel signal:noise. Table 2.2 also lists line strengths relative to Hβ for the total H_2 2.12 μm and Brγ fluxes for Knots 50 and 51 combined together (since the optical line strengths are for the sum of the two knots). These H_2 and Brγ line strengths were measured from our NIR images. The H_2 line strength is taken from Table 2 of Paper II and has an estimated uncertainty of 10% including the random errors and the uncertainties in the sky subtraction and flux calibration. The Brγ line strength was measured for the aperture used for the Hβ spectrum, since the emission occurs over a larger region. The dereddened Brγ/Hβ intensity ratio derived from combining the optical spectra and NIR images is $I(\mathrm{Br}\gamma)/I(\mathrm{H}\beta) = 0.027$, in good agreement with the value 0.028 for Case B. However, it should be noted that the Brγ line is very weak (see Figure 3 of Paper II) and so it is not as well measured as H_2 or the optical lines.

Finally, we converted the reddeningcorrected fluxes to surface brightness. The line emission comes from a much smaller area on the sky than is included in our extracted spectrum (Figure 2.3, left panel). The HST images in Figure 2.2 show that the Hβ signal:noise ratio is too low to be able to tell exactly where that line comes from, and that the [O III] line comes from a somewhat more extended area than [S II] or [O I].

Table 2.2: K51 Observed and Dereddened Emission Line Fluxes

Line	Observed $F(Line)/F(\mathrm{H}\beta)$	Dereddened $I(Line)/I(\mathrm{H}\beta)$	Estimated Uncertainty(%)
[O II] $\lambda3727$	7.38	12.48	25
[Ne III] $\lambda3869$	1.59	2.55	10
[Ne III] $\lambda3967$	0.38	0.58	50
[Fe V] $\lambda4071$	1.34	1.96	50
H I $\lambda4340$	0.42	0.54	25
[O III] $\lambda4363$	<0.25	<0.32	50
He I $\lambda4471$	0.16	0.19	50
He II $\lambda4686$	0.28	0.31	25
H I $\lambda4861$	1.00	1.00	-
[O III] $\lambda4959$	2.45	2.35	5
[O III] $\lambda5007$	7.31	6.87	5
[Fe II] $\lambda5159$	0.08	0.07	50
[N I] $\lambda5198$	0.17	0.15	25
He I $\lambda5876$	0.65	0.46	25
[O I] $\lambda6300$	5.06	3.29	10
[O I] $\lambda6363$	1.78	1.14	10
[N II] $\lambda6548$	3.06	1.88	20
H I $\lambda6563$	4.82	2.96	10
[N II] $\lambda6584$	9.35	5.71	10
[S II] $\lambda6716$	8.62	5.10	10
[S II] $\lambda6731$	11.25	6.64	10
He I $\lambda7065$	0.25	0.14	50
[Ar III] $\lambda7136$	1.27	0.69	25
[Fe II] $\lambda7155$	0.26	0.14	50

Table 2.2 (cont'd)

Line	Observed $F(Line)/F(\mathrm{H}\beta)$	Dereddened $I(Line)/I(\mathrm{H}\beta)$	Estimated Uncertainty(%)
[O II] λ7320	0.35	0.18	50
[O II] λ7330	0.28	0.15	50
[Ni II] λ7377	1.24	0.63	25
H_2 2.12 μm	0.62	0.14	10
Brγ 2.17μm	0.12	0.03	50
MIPS 24μm (21-26μm)	57.	11.	-
PACS blue (57-83μm)	260.	50.	-
PACS green (79$-$121μm)	120.	23.	-

Observed flux through full aperture: $F(\mathrm{H}\beta) = 1.04 \times 10^{-14}$ erg cm^{-2} s^{-1}.

Dereddened flux through full aperture: $I(\mathrm{H}\beta) = 5.4 \times 10^{-14}$ erg cm^{-2} s^{-1}.

Dereddened 15% of 3.8”$\times$ 11.2”: $S(\mathrm{H}\beta) = 8.4 \times 10^{-15}$ erg cm^{-2} s^{-1} arcsec^{-2}.

For purposes of comparison to the simplified models discussed below, we assume that all lines come from the area within our spectroscopic aperture that emits [S II] $\lambda\lambda$6716, 6731, which is 6.4 arcsec^2. This is the projected area on the sky, so for comparison to our Cloudy simulations our measured surface brightness corresponds to a plane-parallel sheet of material seen face on. The relative dereddened line strengths listed in Table 2.2, scaled to the Hβ surface brightness listed in the footnotes to the table, are the primary constraints on the models that we will describe below. Although the line strengths are derived from the sum of the two knots, the conversion to surface brightness allows us to treat them as if they came just from Knot 51.

We also have a NIR long-slit spectrum across Knots 50 and 51, taken with the Ohio State Infrared Imager/Spectrometer (OSIRIS) on the 4 m SOAR Telescope (Paper III). For K51 it shows enough H_2 lines for us to measure an H_2 excitation temperature T_{H2} = 2837±200 K. For comparison, previous studies have shown that the ionized gas has a considerably higher kinetic temperatures, $T_{ion} \sim$ 15,000 K. The 1D-extracted spectrum is shown in Paper III, but here in the last panel of Figure 2.3 we show the 2D image of the region around the 2.12 μm line. The line has a heliocentric radial velocity v_{helio} = 108±5 km s^{-1}, in reasonable agreement with the value $v_{helio} \sim$ 130 km s^{-1} quoted above which was measured from the [S II] lines. This further establishes the spatial connection between the ionized and molecular gas. The 2D NIR spectrum shown in Figure 2.3 has 0.7 arcsec spatial resolution, which is high enough to show that Knots 50 and 51 clearly do have the same velocities and in fact may be connected by a bridge of emission. We did not attempt to combine the H_2 line fluxes measured from this spectrum with the measurements from our optical spectrum, because the NIR spectrum was taken through a slit only 0.4" wide with a somewhat uncertain placement on the knot.

2.2.3 Dust Absorption Features

The HST intermediate-band continuum image shown in Figure 2.2 is of interest because it shows obvious dust absorption (which appears white in our reverse grey-scale image) coincident with K51. We wished to measure the depths of these features in order to find the dust extinction. However, the raw data through the F547M filter include an appreciable contribution from the night sky, which must first be subtracted off. We measured this by using the few existing F547M images that include the outer parts of the Crab together with areas that clearly are outside of the Crab's synchrotron emission region (as determined by comparison to Space Telescope Science Institute Digitized Sky Survey visible and Two Micron All Sky Survey NIR images). This let us produce several individual sky-corrected images, but they did not provide high signal:noise coverage of the K51 region, so were not by themselves suitable for this study. However, we were able to use them to calibrate the sky-subtracted surface brightness at a number of points where the synchrotron continuum is not contaminated by emission from filaments. A further problem is that the sky level varied over time. For each image used in our final co-added continuum image, we measured the surface brightness at a series of fiducial points on the nebula that do not include filaments, and worked out flux offsets for each image which then were subtracted to remove relative differences in the sky level. After making those corrections, we combined the images and then finally subtracted a suitable offset from the co-added image so that it has the same surface brightness at each calibration spot as is measured from our individual sky-corrected images. This produced the sky-subtracted continuum image used here. At the position of K51, this sky correction amounts to 44% of the average level of the continuum at points not in the dust features.

The deepest part of the dust absorption feature at K51 has 69% of the flux level of the adjacent (sky-subtracted) continuum regions. We need to account for the fact that K51 is embedded in the synchrotron emitting gas. As noted above, the radial velocity of K51 shows that it must lie approximately half-way through the synchrotron-emitting region, so for our best estimate we subtracted off half of the continuum level to account for emission in our direction originating between us and the knot. After this correction the K51 absorption feature has a central depth of 62%.

There is uncertainty in this measurement due to the patchy distribution of the synchrotron emission. To estimate the effect of this on our extinction measurement, we integrated the continuum brightness along many 2"-wide lines that lie in the plane of the sky and perpendicular to the long axis of the nebula, and formed ratios of the light coming from either side of the midpoint of the nebula. The RMS scatter in these ratios was 5%, which we used as an estimate of the uncertainty in the fraction of the continuum emission that comes from in front of K51, along our line of sight through the knot.

The extended source complicates the conversion from the measured 1.05 mag dip, to the usual A_V, which includes scattering as well as absorption. In the approximation that K51 is surrounded by a uniform light source and the optical depth is small, scattering into the line of sight compensates for scattering out of the line of sight, and A_V is larger by a factor of (1-albedo)$^{-1}$. This correction gives us the extinction that is usually compared to the gas column density $N_{\rm H}$ and which is what would be observed for a sheet of absorbing material in front of a background point source, so we will designate the corrected value as A_{V-pnt}. At 5470 Å, the albedo is 0.77, 0.67, and 0.81 for the LMC, $R_V = 3.1$, and $R_V = 5.5$ extinction curves given by Draine (2003), corresponding to $A_{V-pnt} = 4.6$, 3.2, and 5.5 mag, respectively. The actual grain composition and size distribution in the Crab is unknown. In the Cloudy models described below, we have arbitrarily chosen the Orion Nebula grain distribution used by Baldwin et al. (1991), for which the albedo at 5470 Åis 0.6. This corresponds to $A_{V-pnt} = 2.6$ mag, which for consistency we use as our observed value for comparison to the models even though it is at the low end of the range of possible A_{V-pnt}. This is about the depth where H_2 initially forms in PDRs (Tielens & Hollenbach 1985). However, the combination of the unknown grain properties and the uncertain and possibly very large correction needed to the observed absorption depth means that the extinction measurement is only a very marginal constraint.

There is also weaker dust absorption associated with the ring that includes Knot 50. Here the central depths indicate $A_{V-pnt} \sim 0.6-1.3$ mag for the same range of assumptions about the albedo of the dust.

2.2.4 Mid-IR Images

There are also archival mid-IR images of the Crab available at 24 μm [*Spitzer* Multiband Imaging Spectrometer (MIPS)], 70 μm [*Herschel* Photodetector Array Camera & Spectrometer (PACS) blue] and 100 μm (*Herschel* PACS green). These clearly detect the Knot 50+51 complex, but at such low angular resolution that it is unresolved with no measurable structural details. The Knot 50+51 complex is blended with the smeared-out images of surrounding structures, but we have crudely measured the total excess flux from the Knot 50+51 complex above what is our best estimate of the underlying synchrotron continuum. The results for each of these passbands are listed in Table 2. In principal, the wavelength covered by these images should include the thermal emission from the dust in K51; a thermal spectrum peaking at about 80 μm is seen in the integrated light of the Crab (e.g. Marsden et al. 1984) and the models presented below predict dust emission with the correct temperature to produce that emission. Knowing the strength of this feature for K51 together with the A_{V-pnt} would place interesting constraints on the nature of the dust formed in the Crab (e.g. Sankrit et al. 1998). However, the Cloudy models described below and the spectra shown by Temim et al. (2012) indicate that the emission from the knots in these bands should be completely dominated by the [O IV] 25.9 μm and [Fe II] 26.0 μm emission lines for the Spitzer MIPS band, and by [O I] 63.2 μm for both Herschel bands.

2.2.5 Intensity of the Radiation Field Striking the Filaments

The incident ionizing flux over the 1−5 Ryd energy range is the crucial input parameter for our Cloudy models. Wu (1981) made careful measurements of the Crab's continuum flux down to 1550 Å, from which it is only a modest extrapolation to 912 Å(1 Ryd). Using Wu's Figure 2, which shows the measured fluxes corrected for extinction E(B−V) = 0.5 ($A_V = 1.55$ for a standard Galactic reddening curve) and scaled to include the full Crab Nebula, we found log $F_\nu(912\ \text{Å}) = -22.71$ and $\nu F_\nu = 6.5 \times 10^{-8}$ erg s^{-1}. Assuming a distance of 2 kpc, this gives $\nu L_\nu = 3.1 \times 10^{37}$ ergs s^{-1} at 912 Åand an integrated ionizing photon luminosity $Q(\mathrm{H}) = 1.7 \times 10^{48}$ photons/sec.

We used that $Q(\mathrm{H})$ value to calculate the incident flux on a slab of gas that is facing the center of the Crab. For the radial position of K51 (approximately 80% of the way from the center to the edge), and assuming a spherical nebula of radius 1.7 pc with uniform volume emissivity in the synchrotron continuum, this predicts an incident ionizing photon flux on the slab $\log(\phi(\mathrm{H})) = 9.7$ (in units of photons s^{-1}) on the front face, and $\log(\phi(\mathrm{H})) = 9.0$ on the back face. The emission from the photoionized region would be dominated by the front face, so we used the higher value of $\phi(\mathrm{H})$ as a point of comparison with our models.

The actual flux incident on K51 is fairly uncertain. An ambiguity in our incident flux calculation is that the synchrotron emission obviously is not uniformly distributed throughout the Crab (as is clear from the HST visible-passband continuum image, for example), plus there could be local beaming effects. The face of the slab will preferentially see the emitting regions directly out in front of it. Also, the incident flux on the slab has a d^{-3} dependence on the distance d to the Crab, which according to Trimble (1973) is probably about 2 kpc but really only is known to lie in the approximate range 1.5−2.3 kpc.

In addition, there are factor-of-three differences between different published luminosity values for the Crab at 1 Ryd. The broad-band SED constructed by Atoyan & Aharonian (1996; and shown in the review article by Hester 2008) smoothly follows the predicted synchrotron SED across the 1−4 Ryd region and corresponds to the lower 1 Ryd luminosity. Atoyan & Aharonian state that this part of their composite spectrum is from Wu (1981). However, the results actually shown in Wu's paper indicate the three times higher value that we have used here. This produces a local bump above the synchrotron spectrum, as is shown in Figure 1 of the review article by Davidson & Fesen (1985).

Wu's result was substantiated by later near-UV observations by Hennessy et al. (1992). We have checked, and the difference in shapes between these two possible

SEDs does not affect the model calculations we present below. It is really only the luminosity at 1 Ryd that matters. In summary, we found that a reasonable guess at the ionizing continuum flux is in the neighborhood of $\log(\phi(H)) = 9.7$ (in units of photons s^{-1} below 912 Å), but with considerable uncertainty.

2.2.6 Adopted Error Bars

This section has described our best estimates of a number of observed parameters that we will next use to constrain simulations of K51, but it is important to keep in mind the rather large uncertainties. Although K51 is the simplest case we could find, it still has a complicated, poorly-known geometry, which limits our interpretation of the measured emission lines strengths. For example, the Hβ line strength is measured to 5-10% accuracy, and so is the H_2 2.12 μm line strength, so their intensity ratio in Table 2.2 is listed as being known to about 10% accuracy. However, these lines come (at least in part) from physically different regions of the K51 complex so it is very hard to know how to compare the measured intensity ratio to the predictions from the models discussed below in which K51 is described as a very simple plane-parallel slab. The same is true for comparisons between emission lines from high-ionization species to those from low ionization or neutral species; the actual spatial arrangement is far more complicated than that in our simplified models.

The conversion to surface brightness is also uncertain. The deduced surface brightness uses the projected area of the Knot 50+51 complex as if it were a thin sheet seen face-on. If instead the same observed flux in the lines from the ionized gas comes from a thin ionized shell on the surface of a spherical core containing the H_2, there would be a factor of 2 times more surface area. The measured emission-line surface brightness also could easily include limb-brightening effects, due to us sighting down a part of the knot's surface that is especially bright because it faces the strongest continuum source. This would affect the lines that are powered by continuum radiation, but it is unclear whether or not the H_2 would have this same limb brightening.

In addition, the reddening correction is based in part on measurements of the [S II] intensity ratio made by Miller (1973) at a different point on the Crab. We assume that this corresponds to overlying reddening along the line of sight to the Crab, and have not attempted to correct for internal reddening despite the clear presence of dust within K51. The uncertainties in the geometry also affect our estimates of the incident flux.

All of this emphasizes that we are trying to hit a poorly defined target, which must be kept in mind as we describe our Cloudy simulations in the following sections. For our comparisons of the simulations to the observations involving surface brightness, we will regard a factor of two agreement to be adequate, in order to account for the geometrical ambiguities. In contrast, the actual observational error bars are appropriate to use for some key emission-line intensity ratios, such as the ratios between different H_2 lines that were simultaneously observed through the same spectrograph slit.

2.3 Cloudy Simulations of Knot 51

We define a successful model of K51 as one that reproduces the observed emission-line surface brightness including the ionized, neutral and molecular species, from within the observed volume of K51. This includes the thermally populated H_2 levels discussed in Paper III. Additionally, the line emissivities of [O I] and [S II] should spatially correlate with H_2 as is seen in the narrow-band images shown in Paper II. The key issue is to identify the physics that leads to the strong H_2 emission observed from the Crab knots.

2.3.1 General Methodology

For our modeling of K51, we used the open-sourced plasma simulation code Cloudy (Ferland et al. 1998), version 10.00. In one self-consistent calculation, Cloudy tracks the microphysics and ionization structure through the H^+, H^0 and H_2 zones. This is ideal for modeling these knots within the Crab, for which we have emission-line measurements from all three regions. We assumed that K51 is in steady state, meaning that the timescale for any dynamical changes is much longer than that of any of the atomic processes involved. The implications of this assumption are discussed in Section 4.

The filaments are illuminated by the hard synchrotron radiation field, which we refer to as the incident continuum. For simplicity, we used the synchrotron spectrum averaged over the whole nebula, by digitizing the spectrum shown in Figure 1 of Davidson & Fesen (1985). However we note that the observed SED depends on position, being harder in the central regions and softer in the outer regions (Mori et al. 2004). All models also include the effects of a cosmic ray energy density representing at least the Galactic background level. The "ionizing particles" model discussed below has a far higher cosmic ray energy density representing the particles that produce the Crab's synchrotron continuum emission (see §3.5).

We assumed a plane parallel geometry for all models, because it is the simplest case and the actual geometry is unknown. Since the actual knot is illuminated from all sides, all models are constrained to have a thickness of $10^{16.5}$ cm, which is half the observed width on the sky of K51. The synchrotron continuum penetrates successive H^+, H^0, and H_2 layers. The outer, ionized regions attenuate the incident continuum, eventually allowing H_0 and H_2 to form. A similar analysis has been conducted by Sankrit et al. (1998), but using a cylindrical geometry, a smaller suite of observational constraints, and, most importantly, not considering molecular gas.

We included the H_2 molecule described by Shaw et al. (2005) in our calculations.

This model includes all rotational/vibrational levels within the ground electronic state, and the six lowest electronic excited states that are coupled to the ground state. Photoexcitations, collisional excitation and deexcitation, bound-bound transitions, ortho-para conversion, collisional dissociation, high energy effects and the chemistry network are all included, self consistently with other properties of the gas. These calculations also include the model Fe II atom described by Verner et al. (1999).

The Crab contains dust, as is evident from the thermal emission feature peaking at ∼80 μm in the SED of the full Crab Nebula (Glaccum et al. 1982; Marsden et al. 1984) and from the dust absorption features seen scattered across the face of the Crab in visible and IR images (Fesen & Blair 1990; Hester et al. 1990). Sankrit et al. (1998) estimated that the Crab filaments might contain up to an order of magnitude greater dust/gas ratio than the ISM, and recent Herschel results (Gomez et al. 2012) appear to confirm this when averaged over a large area on the sky. However, we do not have a strong constraint on the actual dust/gas ratio in the particular knot K51, so we adopted as our default value the ISM dust/gas ratio (although we did check the effect of varying this ratio in our final models; see §3.6).

Dust provides extinction that shields the molecular regions from the incident continuum. Furthermore, dust acts as a catalyst for H_2 formation. We adopted the rate given in Cazaux & Tielens (2002) for formation of H_2 through grain catalysis. We assumed the same mix of silicate and graphite grains and grain size distribution used by Baldwin et al. (1991) to represent the Orion Nebula dust.

2.3.2 H_2 Emission in Non-Equilibrium Environments

One major goal of our models is to reproduce the observed H_2 emission strength and thermal level populations presented in Paper III. The H_2 lines are very strong relative to nearby H I lines, and the excitation diagrams indicate a temperature of around 3000 K.

H_2 emission can be produced by a variety of processes (see Chapter 8 and Appendix 6 in Osterbrock & Ferland 2006; hereafter AGN3). Starlight fluorescent excitation is important in H II regions like the Orion Nebula. The strength of the H_2 emission relative to H I recombination lines is determined by the shape of the SED, as discussed in Paper III, with harder SEDs producing weaker H_2/H I ratios. The SED in the Crab is exceptionally hard, but the measured (H_2 2.12 μm)/Brγ intensity ratio is also large. Paper III shows that with the Crab's SED, UV fluorescence photoexcitation and H I recombination will produce a $\sim$3 dex smaller H_2/H I intensity ratio than is seen in the Crab. Fluorescent excitation is negligible in Crab filaments.

X-rays and ionizing particles penetrating into knots' cores are possibilities. These actually behave in a very similar manner (AGN3 Chapter 8). An ionizing particle entering cool atomic or molecular regions will dissociate and ionize the gas. A newly created free electron has a large amount of energy and creates a shower of secondary suprathermal electrons with a typical energy of about 40 eV. These can excite emission lines, heat the gas, and create further ionization / dissociation. X-rays would produce very similar results. In the central regions of the knots the lower-energy ionizing photons have been removed by the photoelectric opacity of the outer layers, and the penetrating photons have high energy, roughly 10 keV (Figure 2.4). Inner shells of the heavy elements absorb such high-energy photons. The photoelectron has a large kinetic energy, and the inner-shell hole produces additional high-energy Auger electrons. The result is a shower of secondary electrons producing heating, ionization, and excitation.

The net effect of the secondary electrons produced by X-rays or ionizing particles depends on the degree of ionization of the gas. Collisions between the secondary suprathermal electrons and thermal electrons will change kinetic energy into heat since electron electron collisions are elastic. In this case the H2 emission will be the result of collisional excitations by thermal electrons and the level populations

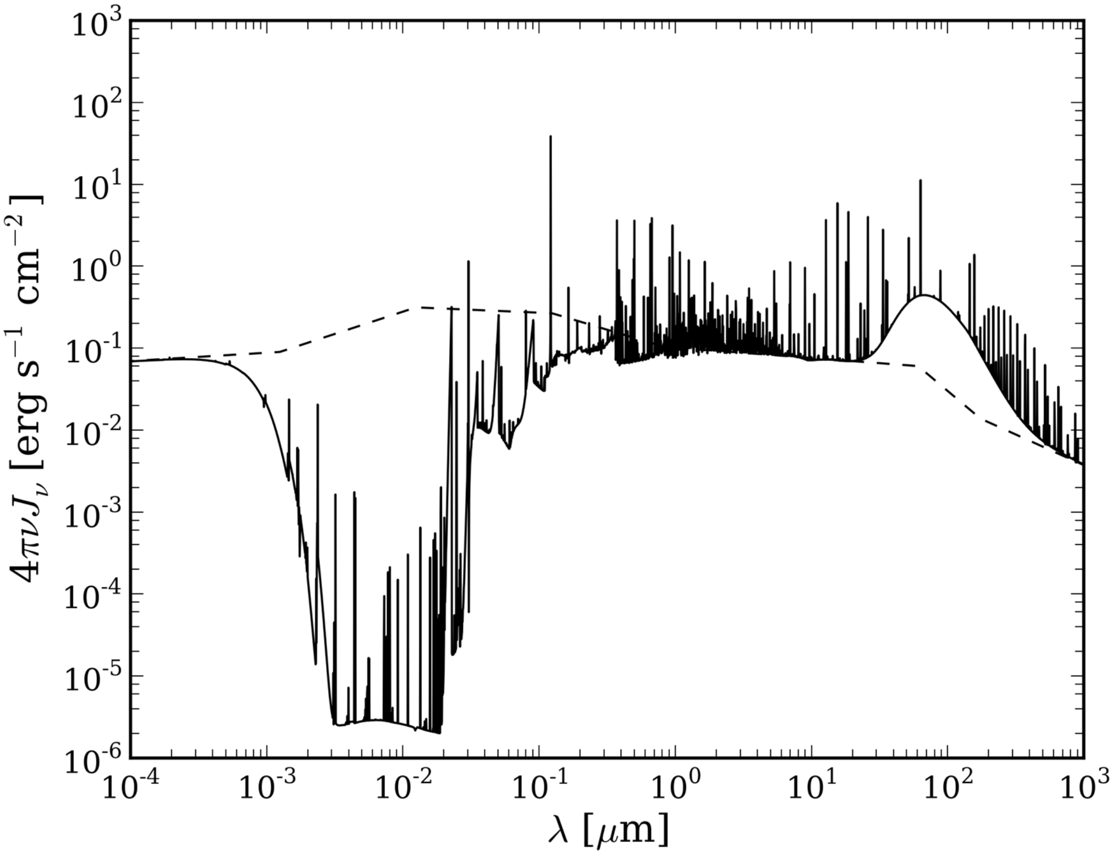

Figure 2.4 The spectral energy distribution in the center of the knot, including the transmitted synchrotron continuum, for the dense core model (solid line). The dashed line is the incident continuum. X-rays with energies $E = 1 - 10$ keV, corresponding to $\lambda = 10^{-3} - 10^{-4}\mu$m, penetrate deep into the core of the knot and are preferentially absorbed by the inner shells of heavy elements. This produces high-energy Auger electrons and a shower of secondaries which then heat, ionize and excite the gas. This is the mechanism responsible for producing H_2 emission in the dense core model.

will appear thermal. When there are few free electrons the energy of the secondary electrons is used to heat, ionize, and excite the gas. Direct excitation of the H2 electronic Lyman-Werner bands will produce non-thermal emission that is nearly identical to that produced by fluorescent excitation. The result in this case will be a highly non-thermal excitation diagram.

Other sources of heat such as shocks or dissipative MHD waves are possible. These generate heat that raises the gas kinetic temperature. The resulting H_2 emission will be thermal if the density is high enough the H_2 level populations will have an excitation temperature equal to the gas kinetic temperature. At lower densities the level populations will appear thermal but at a temperature that is smaller than the kinetic temperature.

In the following subsections we describe a series of Cloudy models that systematically test for these different possible H_2 excitation mechanisms.

2.3.3 A Basic X-ray Photoionization Model in Pressure Balance

We first computed a series of Cloudy models with constant total pressure, photoionized by the Crab's hard synchrotron continuum. The inward pressure of the absorbed synchrotron radiation and the gas pressure at the illuminated face are balanced by the gas pressure within the cloud. The gas is basically in hydrostatic equilibrium (Baldwin et al. 1991). The goal here was to establish a base-line model that would at least properly represent the H^+ zone for a simple case.

Setting the Ionization Parameter

First, the ionizing photon flux, $\phi(H)$, and the initial hydrogen density, n_H, were adjusted so that the model reproduces the observed Hβ surface brightness and the density-sensitive [S II] $\lambda6716/\lambda6731$ ratio (AGN3). The Crab's filaments are made of material expelled from the interior of the progenitor star, and therefore can have very unusual abundances which are known to vary from point to point. As our starting point we adopted the chemical abundances from Model 3 of Pequignot & Dennefeld (1983), which represents gas in the helium−rich band, along with a solar Fe abundance and a solar Ar abundance. For reference, these initial abundances are listed here in Column 2 of Table 3.

For a solar composition H or He absorb most hydrogen-ionizing photons, and there is a simple linear relationship between $\phi(H)$ and the Hβ surface brightness (AGN3). For highly enhanced abundances, such as those found in the Crab, this is not the case

Table 2.3: K51 Chemical Abundances

Element	Initial Abundances by Number[1]	Final Abundances by Number[1]	Final Abundances Mass Fraction[2]	Final Abundances[2] Relative to Solar
He	-0.16	-0.53	-0.27	0.28
C	-2.80	-3.40	-2.66	0.02
N	-3.84	-4.25	-3.45	-0.37
O	-2.62	-3.28	-2.42	-0.16
Ne	-3.11	-3.74	-2.78	0.07
Mg	-4.10	-4.70	-3.66	-0.43
Si	-	-5.05	-3.95	-0.79
S	-4.38	-4.71	-3.55	-0.16
Cl	-	-7.33	-6.11	-0.79
Ar	-5.60	-5.32	-4.06	0.09
Fe	-4.49	-4.61	-3.20	-0.25

[1] Relative to H.

[2] Fraction of total mass.

since heavy elements also remove ionizing photons. The ϕ(H) required to reproduce the Hβ surface brightness does depend on the heavy-element composition. As noted previously in §2.5, the observations suggest that logϕ(H) is roughly 9.7, but with considerable uncertainty. This can be varied to some extent to match observations. This set of abundances gave an optimal value of $\log(\phi(\mathrm{H})) = 10.06$ and $\log(n_{\mathrm{H}}) = 2.97$ cm^{-3}.

Abundances in Ionized Gas

Determining abundances is not the primary motivation for this work, rather we are trying to understand why there is strong H_2 emission. There is an extensive literature about the abundances in the ionized gas, and we do not have useful measurements of the [O III] temperature indicator that would be needed to accurately determine abundances for K51. However, there are known to be point-to-point abundance variations within the Crab (see the introduction), so we did need to carry out a rough determination of the overall metal abundances.

A preliminary adjustment was made to the abundances of O, N, Ne, S, and Ar using the optimizer included within Cloudy to match to match the strengths of [O II] λ3727, [Ne III] λ3869, [O III] λ4959, [O III] λ5007, [N II] λ6584, [S II] λ6716, [S II] λ6731 and [Ar III] λ7135 to within a factor of two. The Fe abundance was not allowed to vary because doing so would have greatly slowed the calculations, so we varied the Fe abundance to match [Fe II] λ7155 after using the optimizer. Silicon and chlorine, for which no lines are observed, were included because of their importance to the chemistry network but with solar abundances. The helium abundance was scaled linearly to match the line strengths of He II λ4686 and He I λ5876. The derived He/H is a bit lower than found in some other regions of the Crab such as the helium−rich belt, but within the range of values reported elsewhere. The model reproduces the observed He II / He I ratio. This ratio is mainly sensitive to the shape of the SED (AGN3; Chapter 2), suggesting that the Davidson SED is a reasonable fit to reality. The values of $\phi(\mathrm{H})$ and n_{H} were iterated to maintain the observed Hβ surface brightness and [S II] intensity ratio.

These preliminary models still produced [O III], [Ne III] and [Ar III] forbidden lines that were systematically too weak relative to Hβ, so further abundance adjustments were required. Increasing the heavy element abundances will not produce stronger forbidden lines in photoionization equilibrium. These lines are among the strongest gas coolants so raising their abundances will only make the gas cooler, the so-called "thermostat effect. However, decreasing all metal abundances raises the gas temperature and shifts the cooling to the optical. This produces stronger optical forbidden lines. Figure 2.5 shows how surface brightness predictions, along with the H_2 temperature and S II ratio, vary as a function of scaling all metal abundances by a given factor.

As the metal abundances decrease, the forbidden line strengths increase until the cooling shifts to collisional excitation of Lyman hydrogen lines. The strengths of these forbidden lines are quite sensitive to the gas temperature. The best abundance set produces T_e =12500 K in the O^{++} -emitting zone of the ionized gas, very similar to previous modeling results (Davidson 1979, Henry & MacAlpine 1982, Sankrit et al. 1998). Unfortunately, our observations do not detect the [O III] λ4363 line, which could directly measure the temperature. The continuum in this region is both noisy and contaminated by emission from other velocity systems, so only a poor upper limit can be obtained. The models predict that the line should be a factor of two or more below that upper limit.

The best abundance set obtained from this process and used throughout the remainder of this paper is listed in Column 3 of Table 2.3. It corresponds to scaling all metal abundances down by a factor of 4 relative to those obtained in the preliminary optimization. These abundances lie between the most metal poor (Henry &

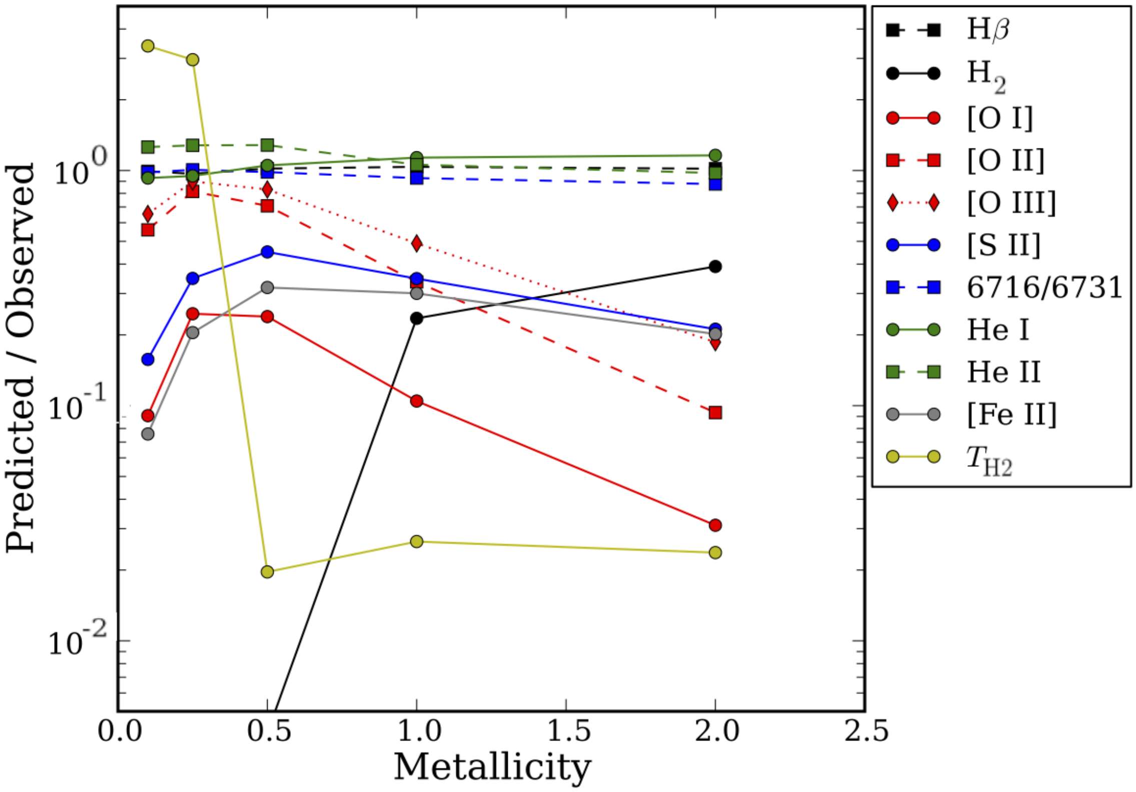

Figure 2.5 The effect of scaling metallicity in our constant pressure model, by number relative to the abundances obtained from our preliminary round of abundance optimization. As the metallicity decreases, the electron temperature rises and cooling shifts to the optical. The net effect is an increase in the optical forbidden line strengths. We adopt a scaling of 0.25, which gives the best fit to the higher ionization lines. For interpretation of the references to color in this and all other figures, the reader is referred to the electronic version of this dissertation.

MacAlpine 1982) and metal rich (Pequignot & Dennefeld 1983) abundance sets found in previous studies.

Sensitivity to the Ionizing Flux

A change in $\phi(H)$ affects the ionization structure of the knot and also the strengths of higher ionization lines, in particular, [O III] $\lambda5007$ and He II $\lambda4686$. Larger values of $\phi(H)$ cause regions that form these lines to extend deeper into the knot. In Figure 2.6a we show the sensitivity of various quantities with respect to the ionizing flux for the constant pressure model. The ionizing flux cannot increase since it leads to the H^+ region becoming substantially larger thereby overestimating [O III] λ5007 and He II λ4686. Decreasing ϕ(H) doesn't provide enough ionizing photons and all lines get weaker, except for the H_2 2.12 μm line which becomes bright.

Despite producing strong H_2 emission, this low ϕ(H) model is not able to predict the observed H_2 level populations. This is illustrated in Figure 2.7b, which compares the observed H_2 level population diagram to the predicted diagram for a constant-pressure model with log(ϕ(H)) =9.66. The observed populations in Knot 51, and also in the other 6 knots observed for Paper III appear thermal, but the higher-energy

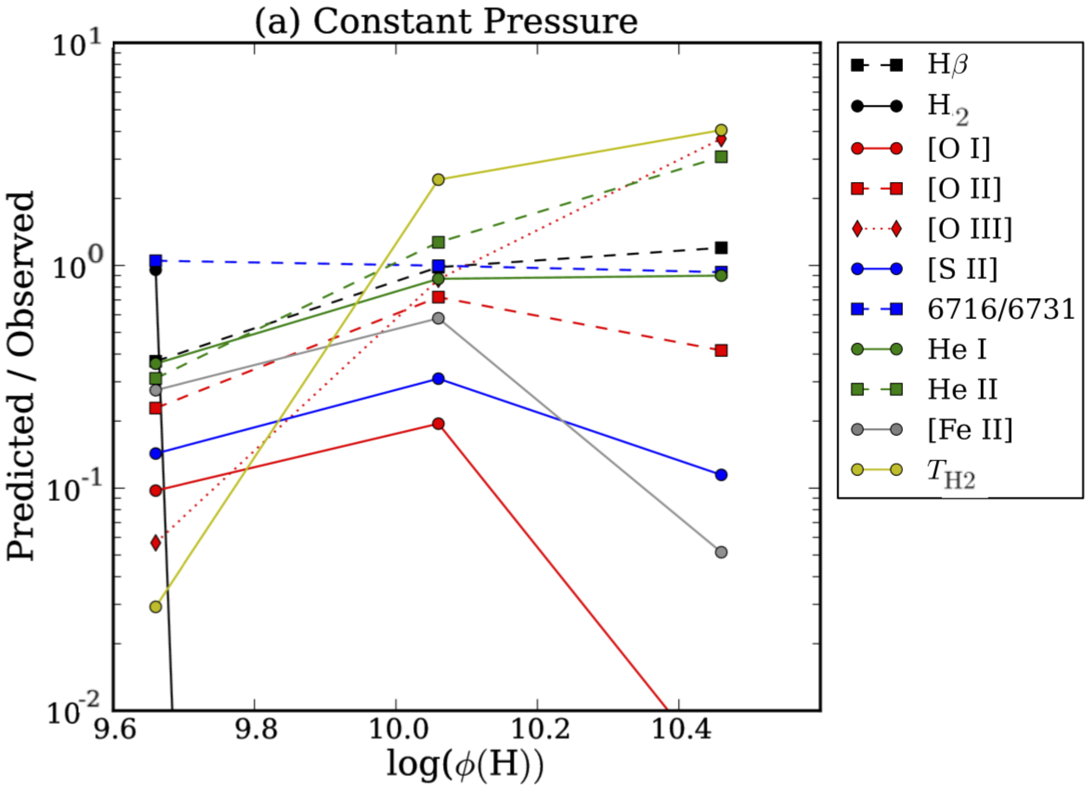

Figure 2.6 The predicted/observed ratios of surface brightness or intensity ratios of key emission lines and of T_{H2}, as a function of the ionizing flux ϕ(H), for the constant-pressure case (a), dense core case (b), temperature floor case (c), and ionizing particles case (d). In the ionizing particles case, Hβ and He I depend only weakly on ϕ(H) because ionizing particle heating accounts for over 50% of the surface brightness. In both cases the H_2 weighted core temperature is set almost entirely by the extra heating in the core rather than by the ionizing flux.

Figure 2.6 (cont'd)

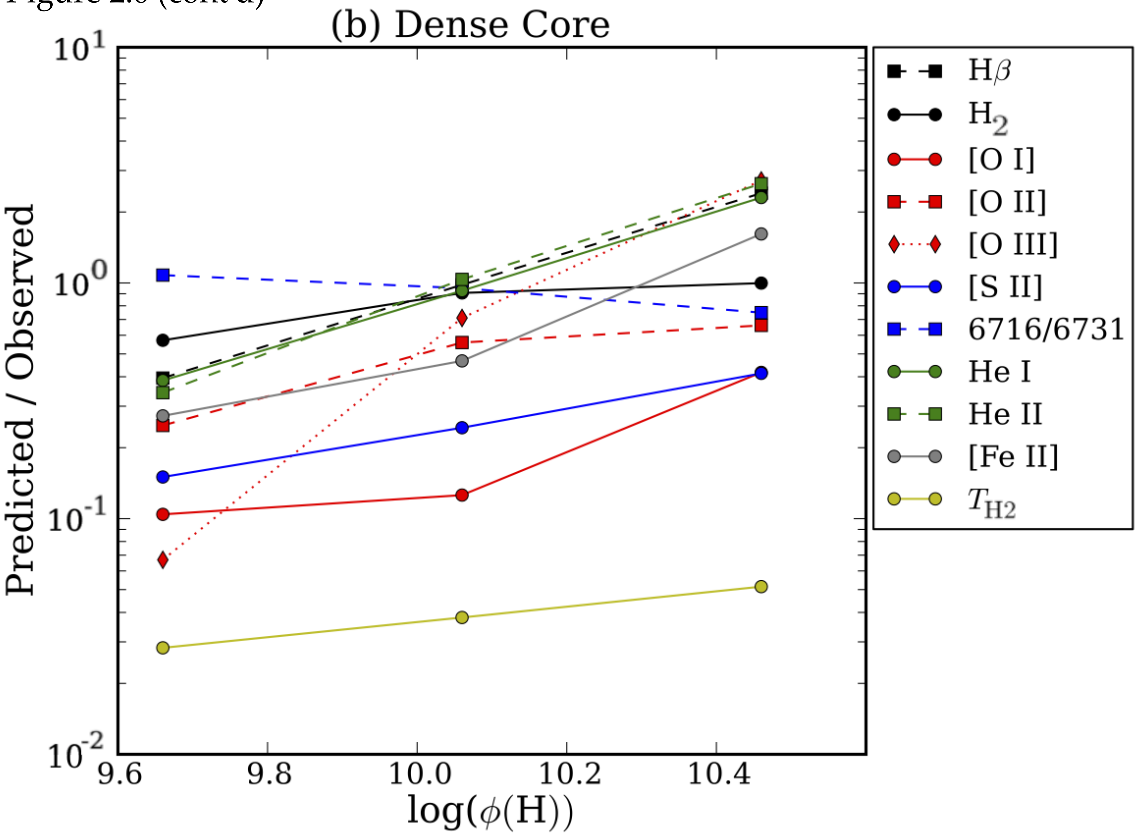

Figure 2.6 (cont'd)

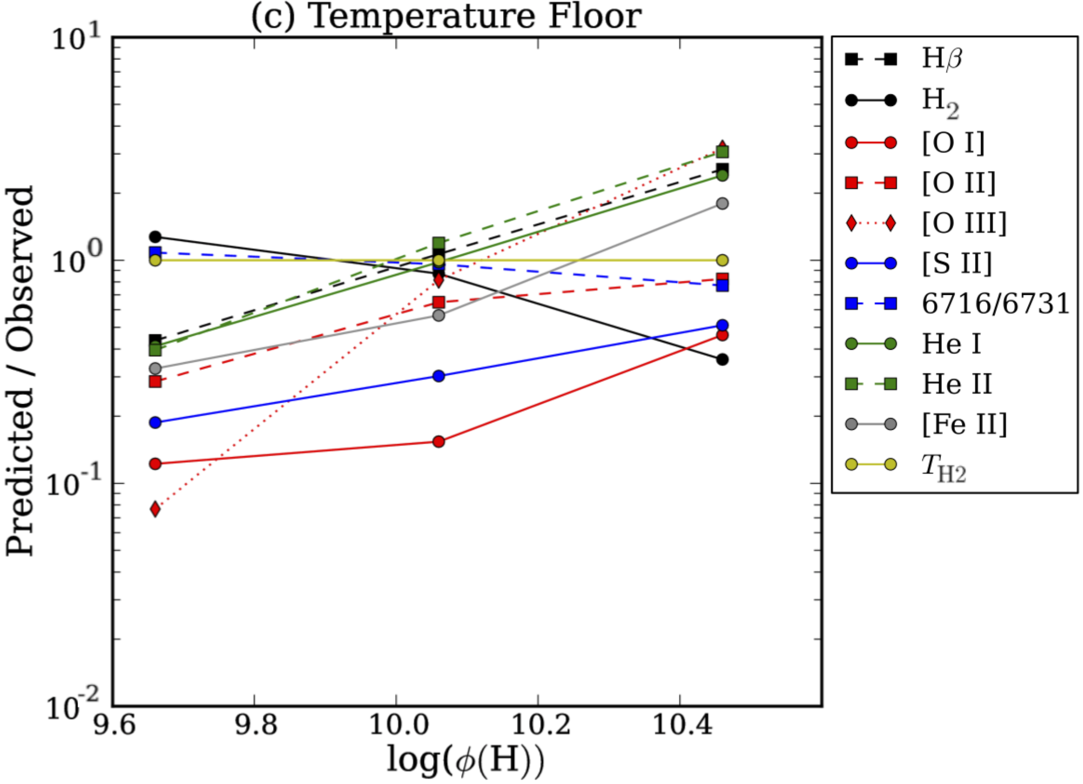

Figure 2.6 (cont'd)

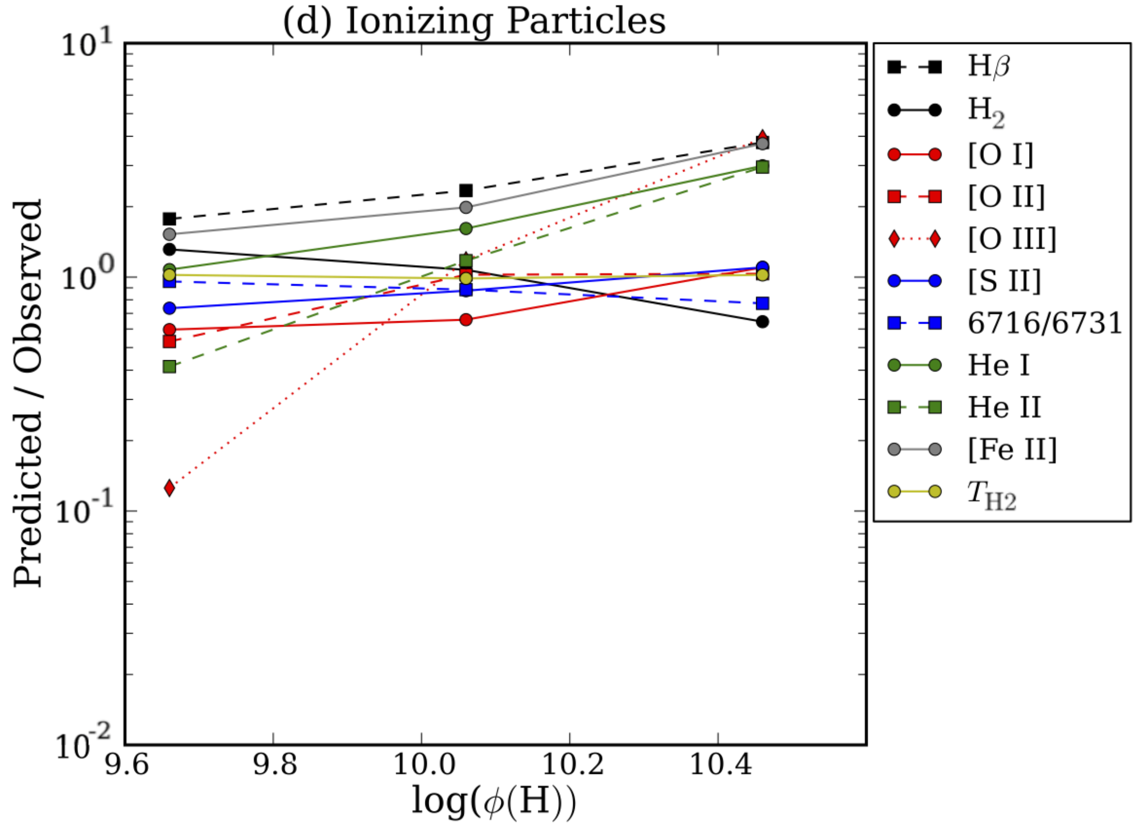

levels in this series of models have a decidedly non-thermal population. This produces a predicted H_2 spectrum that is very different from what is observed. The Cloudy simulation includes all known resonance and fluorescence processes, and reproduces the relative intensities given by Le Bourlot et al. (1995), Sternberg & Neufeld (1999), and Black & van Dishoeck (1987) (see figure 21 of Shaw et al. (2005)) when the same input parameters are used, so Cloudy is able to correctly handle the physical conditions found here.

The strong 2.12 μm emission in the low$-\phi$(H) constant pressure model is obtained by combining a very high column density of H_2 (nearly 10^{21}cm^{-2}) with a core that is very dense. The lower temperature is the result of the high density since the cooling per unit volume depends on the square of the density. The observed H_2 emission in this case is the result of secondary electron excitation of electronic H_2 levels that

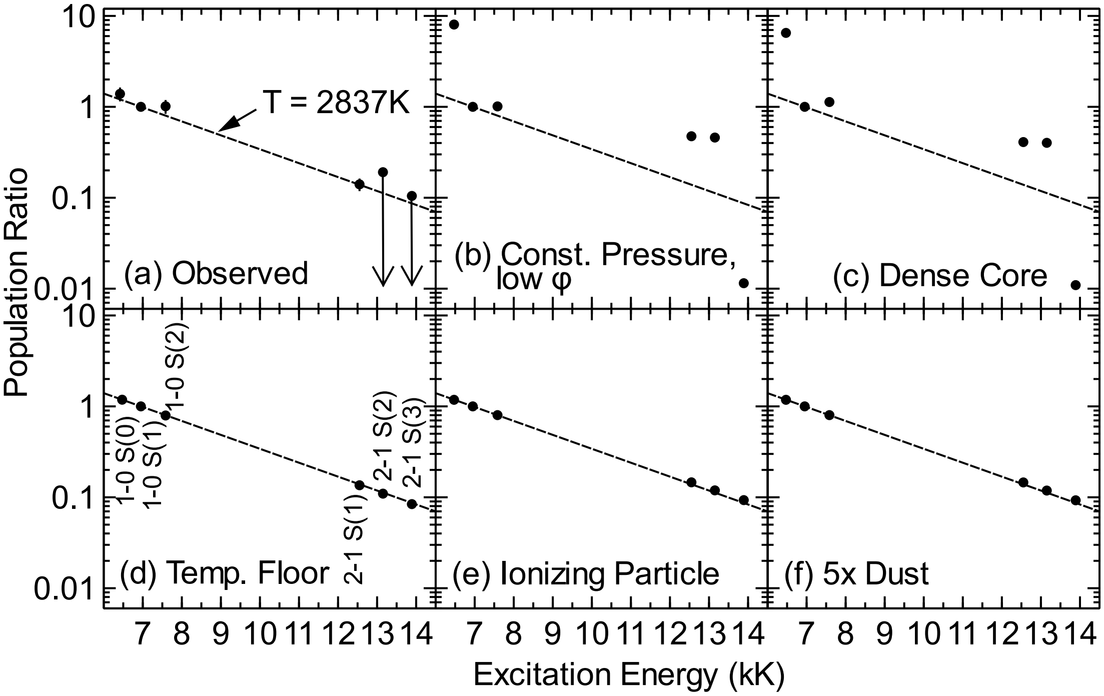

Figure 2.7 Observed and predicted H_2 level populations, normalized to the 1-0 S(1) 2.12 μm line. Panel (a): observed values for Knot 51 (from Paper III), showing four detected H_2 lines with error bars, and upper limits for two undetected lines. Panels (b), (c), (d), (e) and (f): predicted values for five models, showing that the constant-pressure model (here with $\log(\phi(\mathrm{H})) = 9.66$) and dense core model (here with $\log(n_{\mathrm{core}}) = 6.0$) do not fit the observations, while the temperature floor, ionizing particles, and 5x Dust models do fit.

produces a fluorescence spectrum very similar to starlight pumping. This results in a highly nonthermal excitation diagram, in conflict with the observations, which together with the weakness of the lines from the H^+ zone rules out this low ϕ(H) model.

Final Constant Pressure Model

The constant pressure model that best fits the H^+ zone has $\log(\phi(\mathrm{H})) = 10.06$ and metal abundances decreased by a factor of 4 from our initial values. We explore it further here. The physical conditions, line emissivities, and hydrogen structure for this model as a function of depth into the cloud are shown in Figure 8a. The top panel shows the number density of the indicated hydrogen state as a fraction of the total hydrogen density including all states. The middle panel provides the electron temperature as well as the electron and hydrogen number densities.

The depth dependence of the emissivity, or net emission produced per unit volume at each point and escaping the cloud, is given in the bottom panel of Figure 8a. The surface brightness in each of these lines is not shown in the figure, but is found by integrating the line's emissivity over all depths through the cloud. Examination of Fig. 8a shows that in the constant-pressure model the gas is mostly ionized with very little H_0 and no fully molecular zone. The remaining parts of Figure 8 show additional models that will be discussed below.

To quantify the comparison to observations, Table 2.4 shows the ratio of the predicted/observed surface brightness of various emission lines, and also some key Cloudy input parameters, for this and the series of additional models described below. The models are compared to the observations by considering predicted/observed surface brightness ratios for each separate line in order to give a clearer picture of which lines are properly reproduced by which models in a situation where the strength of Hβ (typically used as the denominator in tables of emission-line strengths) also varies from model to model. A value of twice the predicted A_{V-pnt} is used in Table 2.4 because our models only are computed to the center of the knot, while the observed extinction is for all the way through the knot.

The constant-pressure model matches the observed surface brightness of the higher-ionization forbidden lines and of the recombination lines to within ±30%. However, the [O III], [Ne III] and [Ar III] lines are still systematically 10-20% too weak relative to Hβ, suggesting a residual energy balance problem.

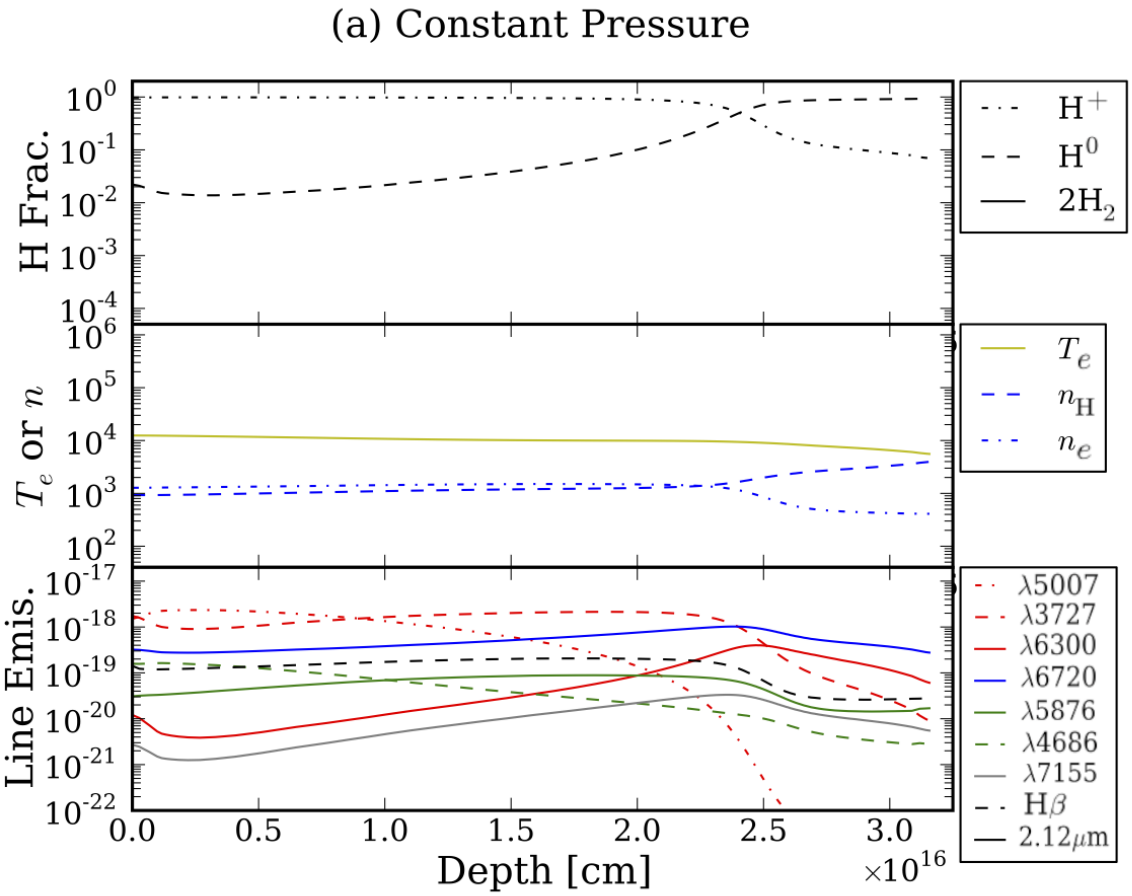

Figure 2.8 Each block of three panels shows the hydrogen ionization structure (top panel), T_e [K] and densities [cm^{-3}] (middle panel), and line emissivities [erg s^{-1} cm^{-3}] (bottom panel), as a function of depth. The different blocks show results for the constant pressure model (a), the dense core model (b), the temperature floor case (c), and the ionizing particles case (d). Comparison of the top panels in each block shows that of the three models which produce H_2 emission, the dense core model has a substantial molecular fraction in its center, while in the temperature floor and ionizing particles cases the H_2 is only a small trace constituent in an extended H^0 zone which emits H_2 as well as low-ionization and neutral forbidden lines.

Figure 2.8 (cont'd)

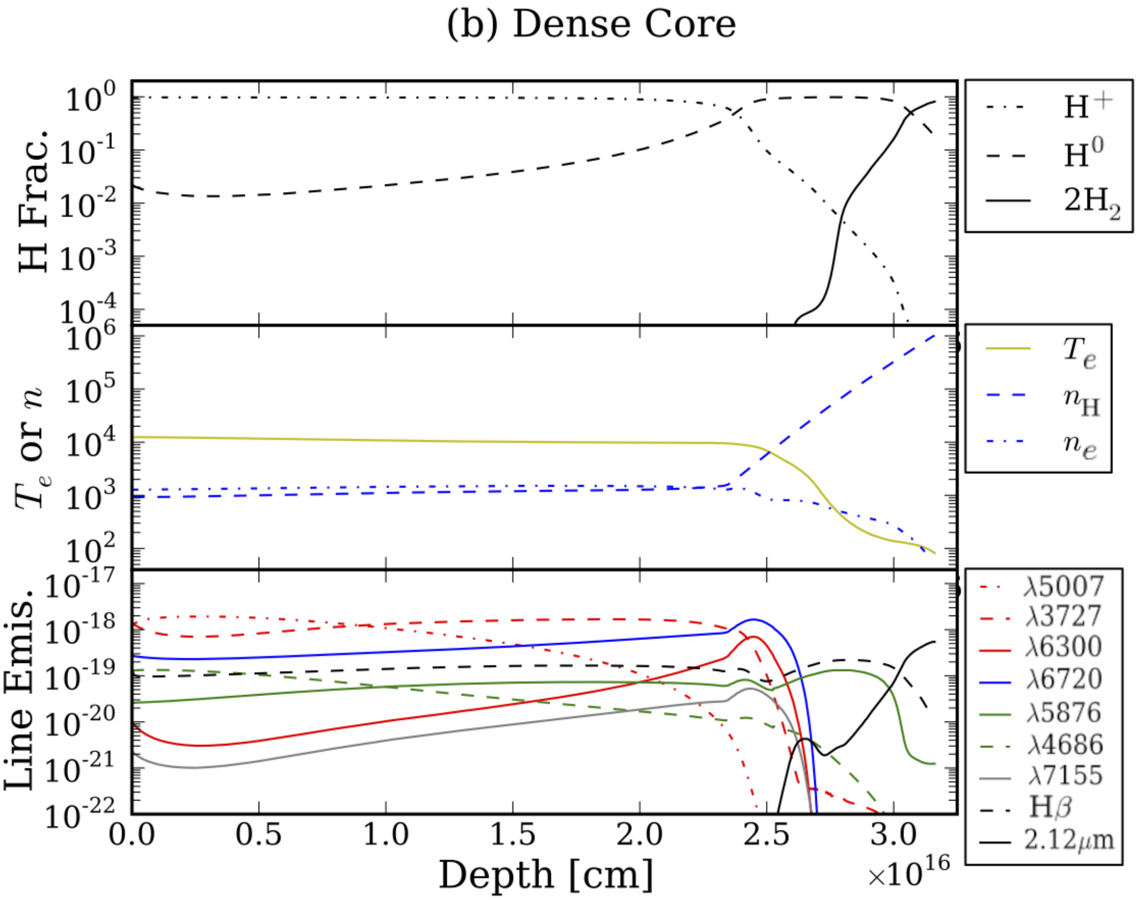

Figure 2.8 (cont'd)

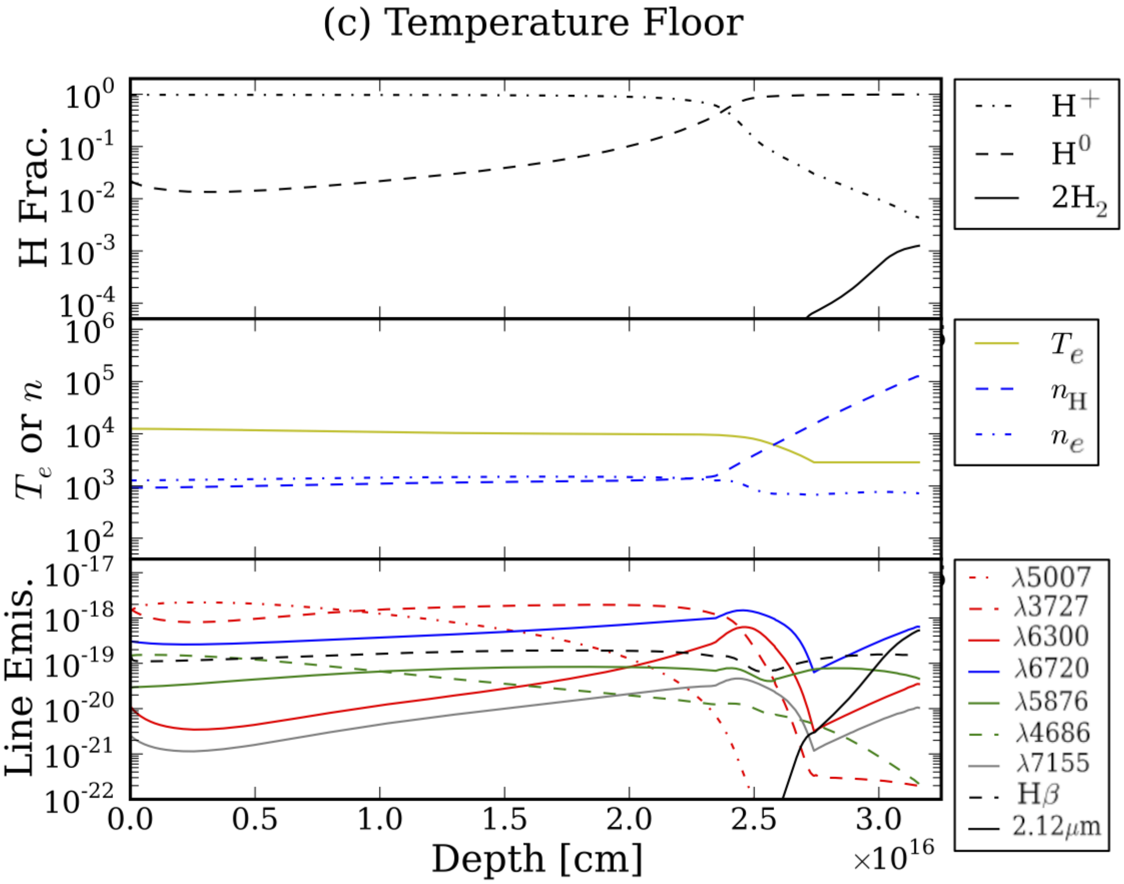

Figure 2.8 (cont'd)

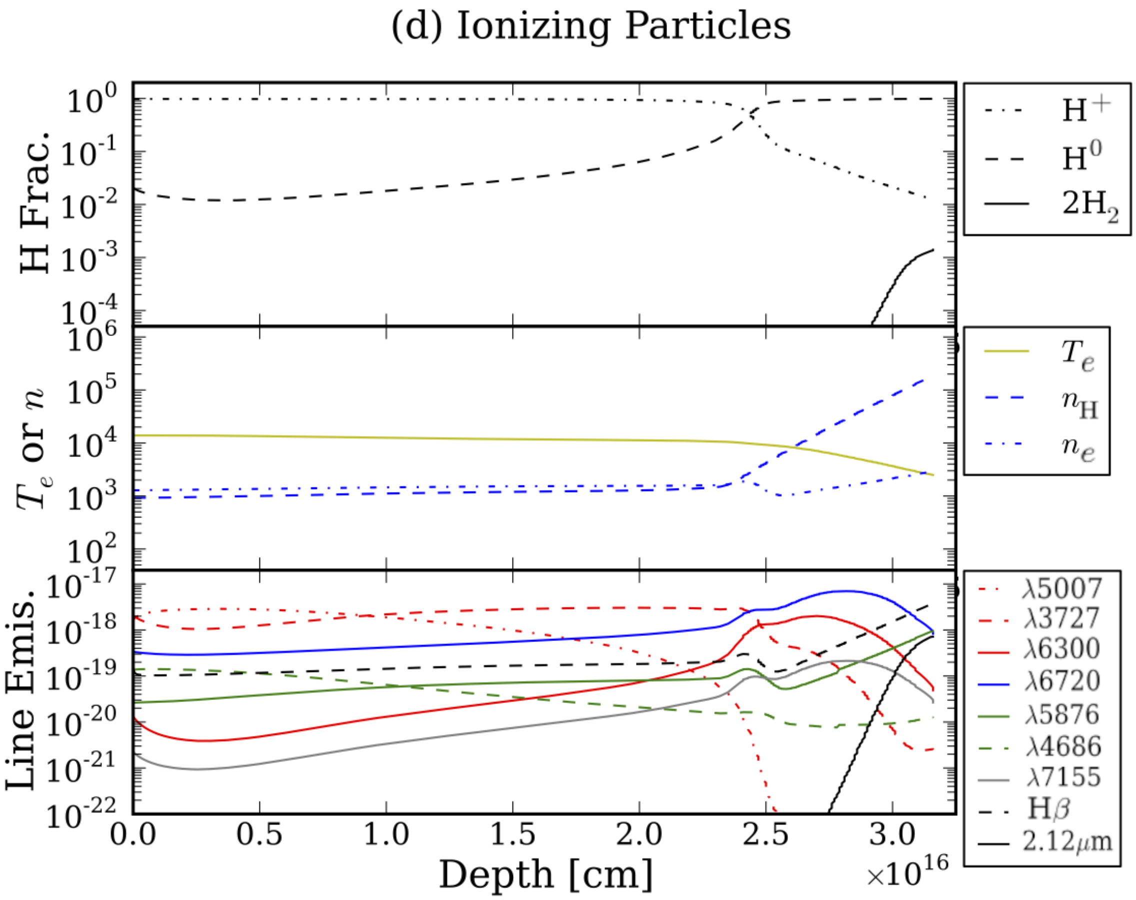

Table 2.4: Model Parameters and Predicted/Observed Surface Brightness Ratios

Parameter	Constant Pressure	Dense Core $\log(n_{\rm core}) = 6.0$	Temperature Floor	Ionizing Particles	5× Dust
$\log\phi$(H) (cm^{-2} s^{-1})	10.06	10.06	10.06	10.06	10.06
log Thickness (cm)	16.5	16.5	16.5	16.5	16.5
Additional Heating	None	None	Temp. floor	$\xi_{\rm H}/\xi_0 = 10^{5.3}$	$\xi_{\rm H}/\xi_0 = 10^{5.3}$
log $n_{\rm core}$ (cm^{-3})	3.6	6.0	5.1	5.25	5.25
$T_{\rm core}$ (T in last zone)	6890	108	2837	2890	2880
Predicted A_{V-pnt}	0.1	1.7	0.3	0.4	2.0
log $N_{\rm H2}$ (cm^{-2})	10.6	20.5	16.9	17.0	17.2
$< n({\rm H}^+)/n({\rm H_{tot}}) >$	5.8×10^{-1}	1.9×10^{-2}	1.0×10^{-1}	1.0×10^{-1}	1.0×10^{-1}
$< n({\rm H}^0)/n({\rm H_{tot}}) >$	4.2×10^{-1}	5.6×10^{-1}	9.0×10^{-1}	9.0×10^{-1}	9.0×10^{-1}
$< n({\rm H}_2)/n({\rm H}_{tot}) >$	1.7×10^{-9}	4.2×10^{-1}	6.3×10^{-4}	5.5×10^{-4}	8.6×10^{-4}
$n_e/n_{\rm H}$ in core	1.0×10^{-1}	7.8×10^{-5}	5.7×10^{-3}	$1.6\text{x}\times10^{-2}$	1.38×10^{-2}
Line	Predicted/Observed Surface Brightness				
H$_2$ λ2.12 μm	0.0	0.9	0.9	1.1	1.5
[O II] λ3727	0.7	0.6	0.7	1.0	0.8
[Ne III] λ3869	0.8	0.6	0.7	1.1	0.9

Table 2.4 (cont'd)

Parameter	Constant Pressure	Dense Core $\log(n_{\rm core}) = 6.0$	Temperature Floor	Ionizing Particles	5× Dust
H I λ4340	0.8	0.8	0.9	2.0	1.3
He I λ4471	0.7	0.7	0.8	1.2	0.9
He II λ4686	1.3	1.0	1.2	1.2	1.0
H I λ4861	1.0	1.0	1.1	2.3	1.6
[O III] λ5007	0.9	0.7	0.8	1.2	0.9
[N I] λ5198	0.4	0.2	0.3	1.6	1.3
He I λ5876	0.9	0.9	1.0	1.6	1.2
[O I] λ6300	0.2	0.1	0.2	0.7	0.5
H I λ6563	1.0	1.0	1.1	2.5	1.8
[N II] λ6584	0.4	0.3	0.3	0.5	0.4
[S II] λ6716	0.3	0.2	0.3	0.8	0.7
[S II] λ6731	0.3	0.2	0.3	0.9	0.7
He I λ7065	0.8	0.8	0.8	1.3	1.0
[Ar III] λ7136	0.8	0.7	0.8	1.0	0.8
[Fe II] λ7155	0.6	0.5	0.6	2.0	1.5

Table 2.4 (cont'd)

Parameter	Constant Pressure	Dense Core $\log(n_{\rm core}) = 6.0$	Temperature Floor	Ionizing Particles	5× Dust
[O II] λ7320	1.2	1.2	1.2	2.3	2.2
H I Brγ λ2.17 μm	0.9	1.1	1.1	2.1	1.7

There has to be more heating per unit volume that is provided by the observed SED, ϕ(H), and $n_{\rm H}$. Previous modeling of the filaments was not so observationally constrained and thus did not encounter this problem. Throughout the process of fitting these models we have accepted cases in which the low-ionization forbidden lines ([O I], [O II], [N II], [S II]) are underpredicted if H_2 is also underpredicted, because these forbidden lines are observed to be H_2 tracers (Paper II). Our aim is to use the constant pressure model as a baseline to which we will then add an H_2 production mechanism which we hope will also contribute lines such as [S II] and [O I]. Indeed, this best-fitting constant pressure model makes a negligible amount of H_2 2.12 μm emission (Table 2.4), ruling it out as a complete model.

2.3.4 Models with Dense Cores

The results from the constant-pressure model suggested that a denser core is needed to have enough column to produce the observed H_2 emission from within the size of K51 while still matching the lines from the H^+ zone. We provided this dense core by introducing a density profile that followed the constant pressure law through the ionized zone, but then quickly ramped up to a higher, constant central core density n_{core} H atoms cm^{-3}. The ramp-up started at a depth of $10^{16.37}$ cm which is the point at which most of the [S II] emission has occurred (so that the density determined from the [S II] doublet ratio would not exceed the measured value), and reached the constant value at n_{core} at a depth of $10^{16.50}$ cm.

We experimented with a range of ncore values. The results are given in Figure 2.9, where the solid line shows the predicted/observed H_2 intensity ratio. We found that $\log(n_{core}) = 6.0$ reproduces the observed H_2 2.12 μm line. This is our best-fitting model of a dense knot that is powered only by the incident synchrotron continuum from the Crab. The physical conditions, line emissivities, and hydrogen structure for this model are shown in Figure 2.8b, and predicted/observed line intensities are

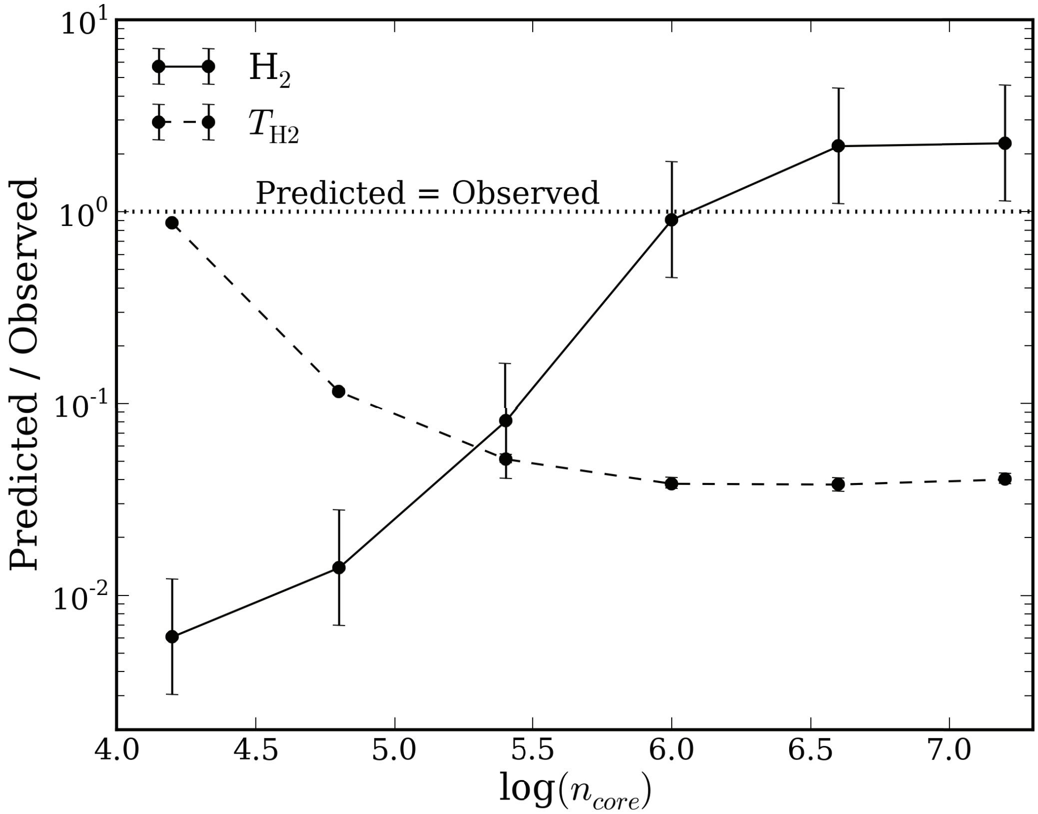

Figure 2.9 The predicted/observed ratio of the surface brightness of the 1-0 S(1) line of H_2 (solid line) and the predicted/observed temperature (dashed line), as a function of core density $n_{\rm core}$, for the dense-core models. The factor-of-two error bars shown for the H_2 surface brightness reflect the uncertainty in the geometry of the knot. $T_{\rm H2}$ is the H_2-weighted kinetic temperature. The model with the best-fitting H_2 surface brightness is for $\log(n_{\rm core}) = 6.0$

given in column 3 of Table 4. Note that the line emissivities of Hβ and He I, shown in the bottom panel of Figure 2.8b, actually increase in the core, where the electron temperature $T_e \sim 500$ K. The predicted line strengths only vary 20% from Case B showing that these lines are mainly due to recombinations.

This best-fitting dense-core model reproduces the observed H I, He I, He II and higher ionization forbidden lines as well as, and in some cases better, than our best constant pressure model, but now also reproduces the observed H_2 2.12 μm emission. However, like the low ϕ(H) constant-pressure case discussed above, it conspicuously fails to reproduce the relative strengths of other H_2 lines for which measurements or observational upper limits are given in Paper III. This is shown in Figure 2.10, which displays the predicted/observed ratios for the other H_2 lines relative to the 2.12 μm line, as a function of n_{core}. The 1-0 S(0) line is predicted to be excited by non-thermal mechanisms and to be several times stronger relative to the 1-0 S(1) 2.12 μm line than is actually observed. This is further illustrated in Figure 2.7c, which compares the observed H_2 level population diagram to the predicted diagram for the $\log(n_{core}) = 6.0$ dense core model. The left most set of points on Figure 2.10 show that the dense-core case which comes the closest to fitting the observed H_2 relative intensities has a lower core density, $\log(n_{core}) = 4.2$. However, Figure 2.9 shows that this model underpredicts the 2.12 μm line by more than two orders of magnitude so it is not viable.

2.3.5 Models with Additional H_2 Mechanisms

None of the above models get the H_2-emitting core hot enough to produce the observed bright, thermal H_2 spectrum. Additional heating is needed in the core. As was suggested by G90, the relativistic particles that fill the Crab's synchrotron-emitting plasma are a likely source. We proceeded as in Ferland et al. (2009) and considered two possibilities. The first is a generic heating source corresponding to mechanical energy input, possibly due to shocks or the presence of non-dissipative MHD waves. We will refer to it as the “temperature floor” case. In this model any collisional ionization would be produced by thermal particles so warm temperatures are needed to produce, for instance, H^+. The second possibility that we considered is heating by relativistic particles, which we will refer to as the “ionizing particle” case. Ionizing particles, as suggested by their name, can produce ions in gas that has a low kinetic temperature. For more details see the study by Ferland et al. (2009) of the filaments seen in the intergalactic medium (IGM) of cool-core galaxy clusters.

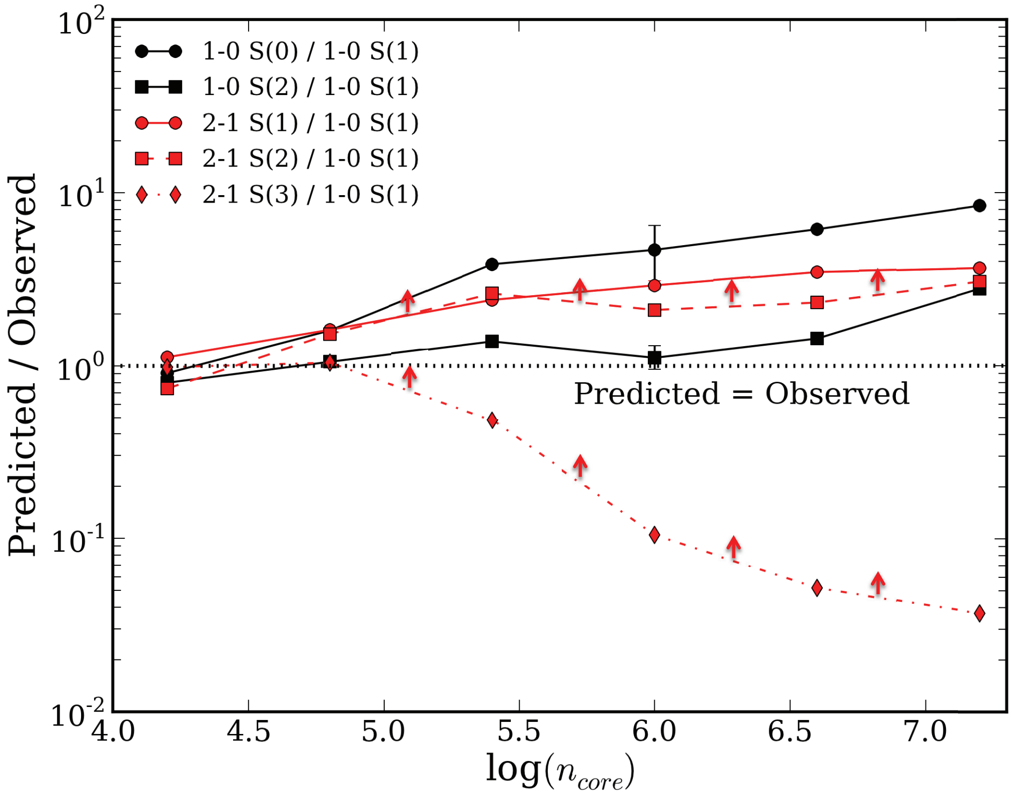

Figure 2.10 The predicted H_2 line ratios divided by the observed H_2 line ratios from Paper III, for the series of dense core models. In a perfect fit, all predicted/observed ratios would be 1. The two curves with upward arrows are cases where the observed value for the line in the numerator is only an upper limit, so that any predicted/observed ratio smaller than 10^0 represents an acceptable fit. For each of the other curves, the error bars shown at a single point are the same size for all points. The model at $\log(n_{\rm core}) = 4.2$, fits the observations the best but it is clearly not ideal, and Figure 2.9 shows that the 2.12 μm emission is too weak.

Temperature Floor Case

In the temperature-floor case, the electron temperature is artificially fixed at the observed H_2 temperature, $T_{\rm H2} = 2800$ K, corresponding to a heating rate of 2.5×10^{-16} ergs s^{-1} cm^{-3}. The only source of ionization in the deeper zones of the knot is through thermal collisions, and the dissociation of H_2 occurs only when the temperature is quite high. We included ionization by cosmic rays at the Galactic background rate of 2×10^{-16} s^{-1} (Indriolo et al. 2007), but not the effects of the additional high-energy particles localized in the Crab Nebula. We iterated over a range of core densities until we reproduced the observed H_2 2.12 μm surface brightness. From this procedure, we found the optimal core density to be $n_{core} = 10^{5.1}$ cm^{-3}.

Ionizing Particle Energy Density

In the ionizing particles case, we included the effects of the high-energy particles that must pervade the Crab's synchrotron plasma. We assumed that these particles penetrate into the dense knots, heating, ionizing and exciting the gas. In regions with high electron fractions, energetic particles predominately heat the gas, while in regions with low electron fractions, they predominately ionize and excite the gas (AGN3; Ferland et al. 2009). We add ionizing particles as in Ferland et al. (2009). Cloudy uses the results of Dalgarno, Yan & Liu (1999) to include the effects of cosmic rays. The key input parameter for Cloudy in this process is the ionization rate per H_2. We parameterize this rate as a ratio relative to the ionization rate in the ISM, $\xi_0 = 2 \times 10^{-16}$ s^{-1}.

We ran Cloudy models for a large grid of ionization rates per particle $\xi_{\rm H}$ and core densities n_{core} to find the models which reproduce the observed H_2 2.12 μm surface brightness and the observed H_2 temperature. Figure 2.11 compares the constraints placed by the observed H_2 temperature and by the Hβ and H_2 surface brightnesses in the $\xi_{\rm H}/\xi_0 - n_{core}$ parameter space. The slanting dashed line marks models which reproduce the observed temperature $T_{\rm H2}$ =2800 K, with the gray shaded area indicating the range due to the observational uncertainty in the temperature (as given in Paper III). The solid contours show the logarithm of the predicted/observed H_2 surface brightness, while the dotted contours show the logarithm of the predicted/observed Hβ surface brightness. A perfect model would have the dashed line simultaneously intersecting with the 0.0 contours for both H_2 and Hβ, but in fact all models overpredict Hβ. We adopted a scale factor of $\xi_{\rm H}/\xi_0 = 10^{5.3}$ and a core density of $n_{core} = 10^{5.25}$

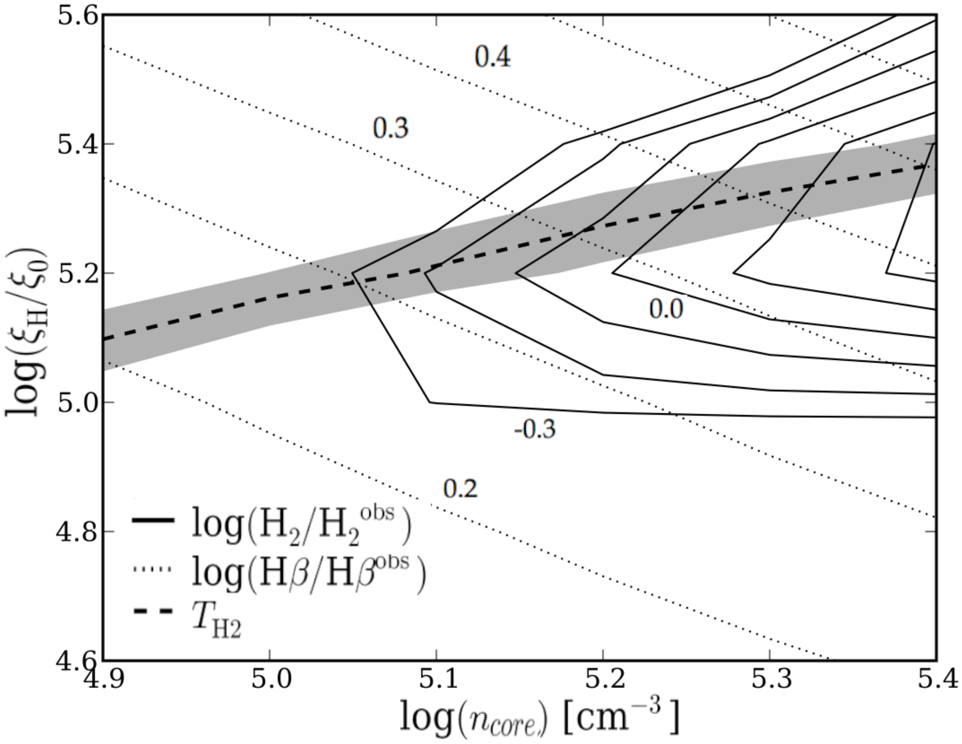

Figure 2.11 The optimization of core density and ionization rate scale factor for the ionizing particle case. Models reproducing the measured H_2 kinetic temperature fall along the dashed line while the gray band indicates the range due to the error bars of the measurement. The log contours show the ratio of the predicted to observed surface brightness of H_2 (solid line) and Hβ (dotted line). We adopt $\xi_H/\xi_0 = 10^{5.3}$ and $n_{\rm core} = 10^{5.25}$ cm^{-3} as the optimal parameters despite the overestimated Hβ emission.

cm^{-3} to be the best parameters for the ionizing particles case. This model overpredicts the Hβ surface brightness by approximately a factor of 2.

We next check to see if the deduced value $\xi_H/\xi_0 = 10^{5.3}$ is reasonable. Positively charged nuclei may be an important component of the ionizing particles (e.g. Hoshino et al. 1992; Gallant & Arons 1994), but there is no way to directly measure their presence. For the electrons and positrons, on the other hand, the energy distribution can be determined from the observed synchrotron radiation, so in the following discussion we will consider just the contribution of these particles. In the case of the ISM this underestimates the cosmic ray energy density by about 1 dex (Webber 1998).

The number of ionizations that the electrons and positrons will cause within the knot depends on the degree to which they are trapped by tangled magnetic fields. One limit is to assume that the magnetic field threads though the knot simply so that particles make only one pass through the knot. Then the flux of particles inside the knot is the same as the flux on the outside where it can be deduced from the synchrotron radiation. Using the number distribution of electrons as a function of energy found by Atoyan & Aharonian (1996) and the ionization cross section of atomic H (Indriolo, Fields & McCall 2009) scaled up by a factor 2.3 to account for ionization by secondary electrons and the difference between H and H_2 (Glassgold & Langer 1974), and integrating over all energies above 50 keV, the minimum energy for which a particle reaches the center of the knot, we found $\xi_{\mathrm{H}}/\xi_0 \geq 10^{3.2}$. This is 100 times smaller than is inferred from the Cloudy models.

An upper limit from the electron/positron contribution is to assume complete trapping so that all of the energy carried by ionizing particles entering the face of the knot is used up in heating or ionizing the large column density of neutral gas. Assuming energy equipartition with a 300 μG magnetic field (Marsden et al 1984)[2] the ionizing particle energy density in the synchrotron plasma is $U_{\mathrm{IP}} = 2000$ eV cm^{-3}. The energy flux into the knot is cU_{IP}, and assuming that there is about one ionization per 40 eV deposited, the total ionization rate for a knot of half-thickness $l_{\mathrm{knot}} = 10^{16.5}$ cm will be $\xi_{\mathrm{H}}\ (cU_{\mathrm{IP}})/(40 l_{\mathrm{knot}} n_{\mathrm{core}}) \sim 1 \times 10^{-9}$ s^{-1}. This corresponds to $\xi_{\mathrm{H}}/\xi_0 \leq 10^{6.8}$, about 30 times larger than the model requirements. The value $\xi_{\mathrm{H}}/\xi_0 = 10^{5.3}$ found for our ionizing particle model lies within the range set by these two limiting cases.

For energy equipartition with the magnetic field, the energetic electron energy density corresponds to a pressure of 8×10^6 K cm^{-3}. This is almost two orders of

---

[2] Recent estimates for the magnetic field at the radial distance of Knot 51 range from 240 μG to produce the synchrotron emission (Atoyan & Aharonian 1996) to 540 μG in the MHD simulations by Hester et al. (1996).

magnitude less than the gas pressure in the core, so even for the case of maximum trapping the ionizing particles are not dynamically important and hence do not affect the geometry of the gas.

Extended H^0 Zones

A crucial result for both cases is that hydrogen in the core of K51 is almost entirely atomic; only a trace amount of H_2 is required to reproduce the observed 2.12 μm line. The lower panels of Figures 2.8a-2.8d show the emissivity as a function of depth for several key lines. In the temperature floor and ionizing particle cases, the Hβ and [S II] line emissivities increase in the H_0/H_2 zone. The middle panels in Figure 2.8a-2.8d displays the temperature and density as a function of depth.

We also found that less than half of the H_2 formation proceeds on grains. H_2 is mainly formed through associative detachment: $H^- + H_0 \rightarrow H_2 + e^-$ (see Ferland, Fabian & Johnstone 1994). The main H_2 destruction paths include UV fluorescence and reverse molecular reactions involved in the formation of H_2. The dependence of these formation and destruction mechanisms on depth is shown in the middle panels and bottom panels, respectively, of Figure 2.12.

Heating and Cooling

Figure 2.13 identifies contributors to the total heating and cooling for both cases. Photoionization of H or He is the dominant heating process in the knot until a depth of 2.7×10^{16} cm where the temperature floor is imposed in the temperature floor case, and to a depth of 6.3×10^{15} cm in the ionizing particles case. The heating sources in the core for the temperature floor model are not meaningful, because the temperature has been artificially set to a fixed value. In the ionizing particles case, the H_0/H_2 zone is heated primarily by the ionizing particles, followed by a 10% contribution by ionization of Fe^0. Cooling proceeds mainly though electron collisional excitation of

(a) Temperature Floor

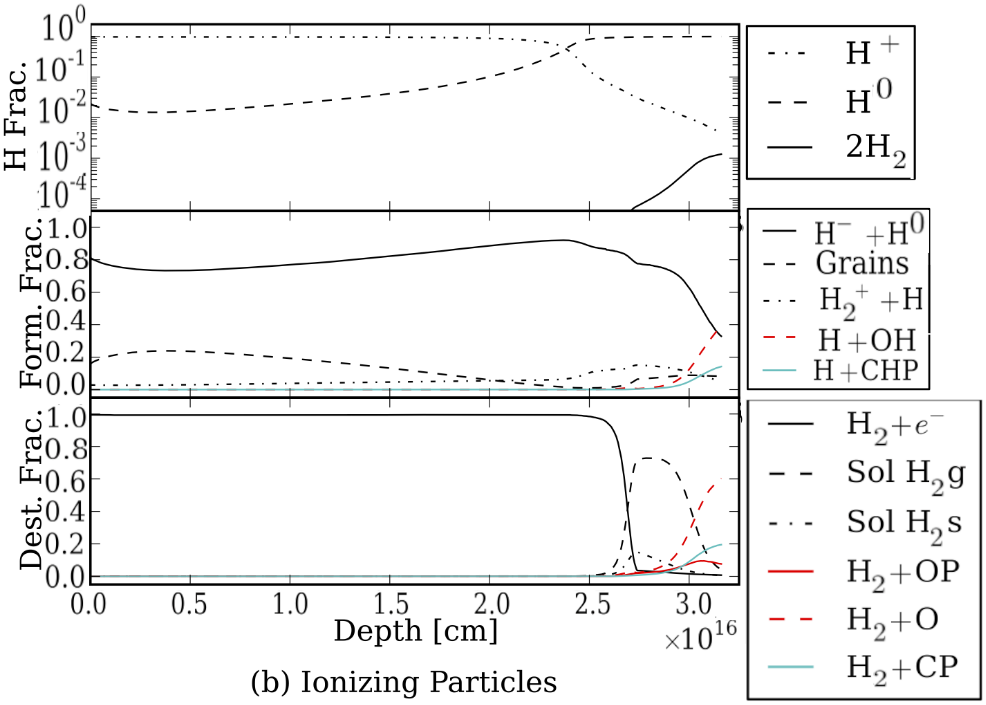

(b) Ionizing Particles

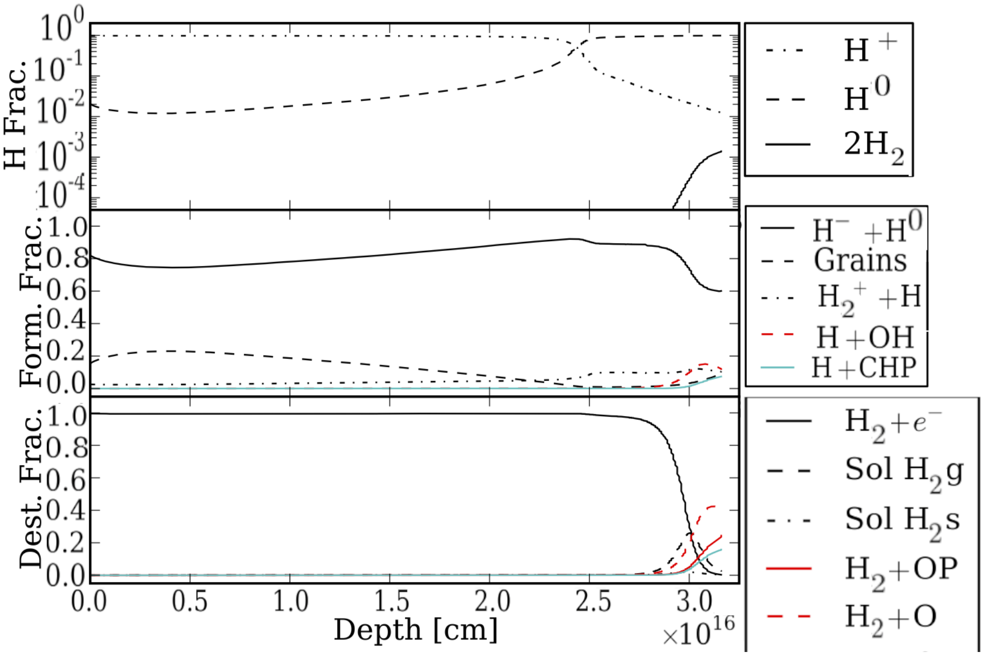

Figure 2.12 The H_2 formation mechanisms (middle panels) and H_2 destruction mechanisms (bottom panels), as a function of depth for the temperature floor case (a) and the ionizing particles case (b). A large fraction of H_2 forms through $H^- + H^0$ associative detachment (solid line in middle panels) rather than grain catalysis ("grains"). This is due to the relatively large $n_e/n_{\rm H}$ ratio in the core (see middle panels, Figure 2.8). The hydrogen ionization structure is shown in the top panels for reference.

[O III] lines in the H^+ zone and of [Fe II] lines in the H_0/H_2 zone for the ionizing particles case.

Effect of the Ionizing Flux in Extra Heating Models

As explained in §3.3.3, the ionizing photon flux, ϕ(H), most greatly affects higher ionization lines, in particular, [O III] λ5007 and He II λ4686. Larger values of ϕ(H) allow regions that form these lines to extend deeper into the knot. Figure 2.6 shows the dependence of various lines and physically relevant parameters on ϕ(H) for the temperature floor and ionizing particle cases. We used $\log\phi((\mathrm{H})) = 10.06$ in the models presented in Table 2.4. We note that Hβ and He I are not strongly correlated with ϕ(H) in the ionizing particles case since cosmic-ray heating accounts for over 50% of the surface brightness. Similarly, the gas kinetic temperature weighted by the H_2 abundance at each point, T_{H2}, is almost entirely set by ionizing particle heating with the ionizing photon flux having only a small effect.

Results for Models with Additional H_2 Excitation

Table 2.4 shows that the core temperatures, H_2 column densities and A_{V-pnt} for the temperature floor and ionizing particle models are very similar. Both models produce a satisfactory H_2 emission spectrum (as shown in panels (d) and (e) of Figure 2.7). The models are largely equivalent: the ionizing particles have provided a physical reason for the temperature floor.

The differences in the results from these two models come from their ability to reproduce the observed neutral and recombination line emission. In the ionizing particle case, the [O I] emission is correct to within 30% and [N I] is overpredicted by 60%. Ionizing particles ionize and heat the gas, producing stronger lines in the neutral zone. In this regard, the ionizing particles case is more successful than the temperature floor case which produces only about 20% of the [O I] and [N I] emission. The reason for

(a) Temperature Floor

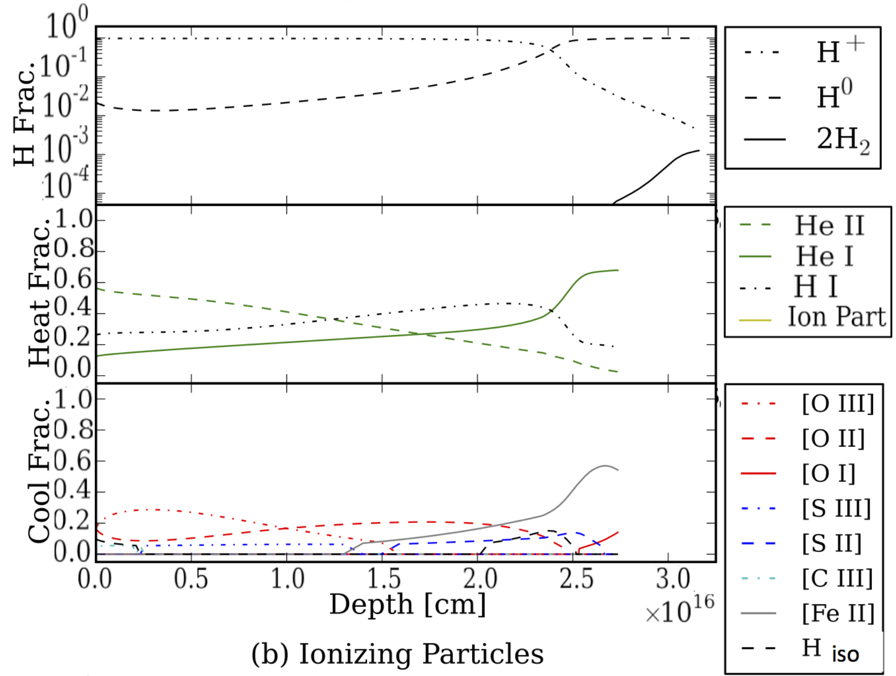

(b) Ionizing Particles

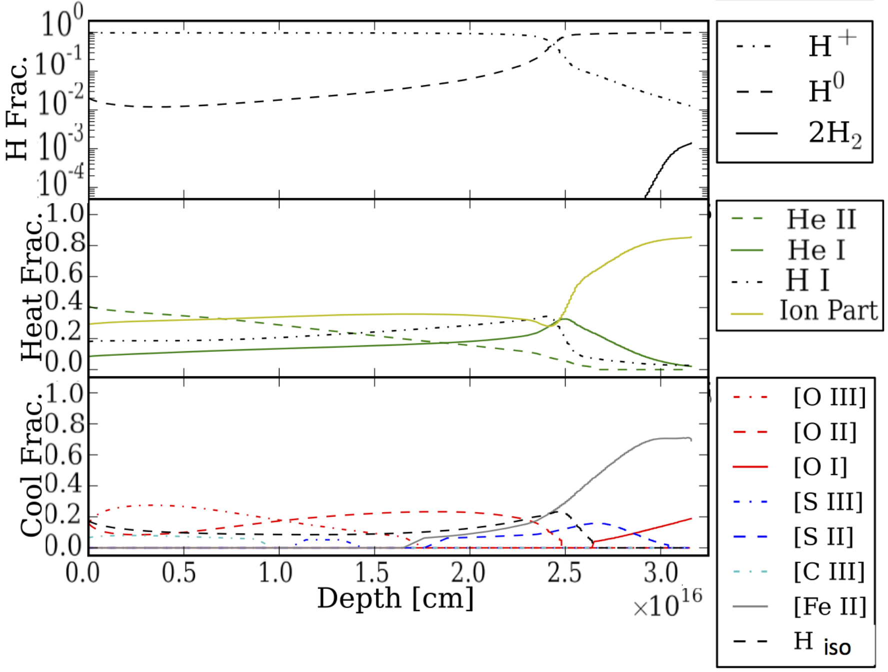

Figure 2.13 The heating fractions and cooling fractions as a function of depth, for the temperature floor case (a) and the ionizing particles case (b). The knot is heated by photoionizations followed by recombinations of the different ions indicated in the legend in the H^+ zone. But, heating by ionizing particles dominates in the H_0/H_2 zone for the ionizing particles case.

this stems from the temperature at which the H_2 is observed. Neutral oxygen requires temperatures of about 7000-8000 K to thermally excite substantial emission, while the measured H_2 temperature is only about 2800 K. In the temperature floor case, the [S II] doublet is underpredicted by a factor of 3, however in the ionizing particles it is correct to within $\sim$15%. The extra [S II] emission in the ionizing particles case comes from the core, which we explain in detail below. Finally, the temperature floor case correctly reproduces the [O II] λ7320 line but the ionizing particles case overpredicts it by a factor of two. However, there is considerable uncertainty in this particular measurement.

Conversely, the H^0 and He^0 recombination lines are overpredicted by approximately a factor of two in the ionizing particles case. This is a failure of the ionizing particles case, but the temperature floor case correctly predicts all recombination lines to within 20%. The discrepancy here arises from the physics in the core. Figure 2.8 displays the emissivity of Hβ for both cases (shown as the dashed black line in the bottom panels). The ionizing particles case features an increase in Hβ emission in the core due to ionization of H^0, the majority of the hydrogen, followed by recombinations. The temperature-floor case does not display this feature since the gas is too cool to collisionally ionize H. In this aspect, the temperature floor case is more successful than the ionizing particles case. The existing HST Hβ images have too low signal/noise ratio to be able to tell whether or not there is emission from the core. Future high-resolution Hβ imaging with better signal/noise ratio will help to decide whether the ionizing particle case is a viable model.

A successful feature of both the temperature-floor case and the ionizing-particles case is that part of the [S II] $\lambda\lambda$6720 doublet is emitted from the same region as molecular hydrogen (bottom panel of Figure 2.8c and 2.8d). This is observed to be the case in Knot 51 (Fig 2), and in Paper II we showed that many other, fainter regions of the Crab's system of filaments produce H_2 emission that correlates with [S

II]. Our two viable models are consistent with this observation. Conversely, Figure 2.8a shows that the constant pressure model does not emit any $H_2$and Figure 2.8b shows that the dense core model emits H_2 only from a region largely separate from that which emits [S II].

Both the temperature floor and ionizing particle cases are able to reproduce the major observational signatures of the H_2 knots. However, each of these models has failures as well as successes, making it unclear which model is to be preferred. In both cases, we are able to successfully reproduce the forbidden lines from the ionized gas to within a factor of two, the H_2 2.12 μm line to within 10%, and the correct relative strengths of the observed H_2 lines.

A variation on the ionizing particles model is to accept a worse fit to the H_2 2.12 μm surface brightness, but one that is still within the uncertainty of the measurement, in order to lower the recombination line strengths enough so that they fit the observations to within a factor of two. A model with $\log(\xi_{\rm H}/\xi_0) = 5.2$ and $\log(n_{\rm core}) = 5.1$ produces only 70% of the observed H_2 emission, but fits all the optical lines to within a factor two except for [O II] λ7320. However, the purpose of this paper is to explore models that match the H_2 emission. Therefore, this model which purposefully did not attempt to fit the H_2 emission will not be considered any further.

2.3.6 Models with Increased Dust Abundance

The models with extra H_2 excitation mechanisms reproduce the observed H_2 spectrum along with the surface brightness of many optical lines. However, these models underpredict the observed A_{V-pnt} ~3 mag. Recent estimates of the Crab's total dust content range from 0.002 $M_\odot$ (Temim et al. 2012) to 0.25 $M_\odot$ Gomez et al. 2012), and the dust/gas ratio is known to vary from place to place within the filamentary structure (Sankrit et al. 1998). Sankrit et al. (1998) estimate the mass ratio M_{dust}/M_{gas} to be as large as ten times the ISM value for one filament. We do not have additional information that allows us to constrain the dust abundance in the Crab. However, we tested the robustness of our results by varying the dust abundance, ranging from dust-free to an order of magnitude above the ISM value. For simplicity, in the ionizing particles case, we did not reoptimize the heating rate and core density as this is a computationally expensive task. Instead, we simply explore the parameter space here to present the sensitivity of various relevant values.

The top panel of Figure 2.14 shows the fraction of H_2 formation due to grain catalysis ("grains") and associative detachment ("$H^- + H_0$") at the center of the knot and the predicted/observed A_{V-pnt} ratio measured clear through the knot, plotted as a function of dust abundance for the temperature floor and ionizing particle cases. In both cases, the H_2 formation rate by grain catalysis eventually becomes faster than associative detachment. The observed A_{V-pnt} is found at approximately 10 times the ISM dust abundance. The bottom panel of Figure 2.14 shows a slow decrease in the optical line strengths as function of dust abundance due to increased extinction. In contrast, H_2 emission increases with dust

abundance due to an increase in the H_2 abundance due to grain catalysis and shielding.

An ionizing particles model with a dust abundance a factor of 5 above the ISM value gives a reasonable fit to observed surface brightnesses as well as matching the observed A_{V-pnt} to within about a factor of three (Table 2.4). Internal extinction removes many of the Hβ photons generated in the central core and brings this line into better agreement with the observations. This model matches all the higher ionization forbidden lines to within 20%, all recombination lines to within at least a factor of 2, and the thermal H_2 spectrum (Figure 7f). However, it does fail to produce enough [N II] λ6584 and [O II] λ7320.

Table 2.4 does not include the Spitzer or Herschel broad-band measurements because these are extremely crude measurements which combine continuum emission

(a) Temperature Floor

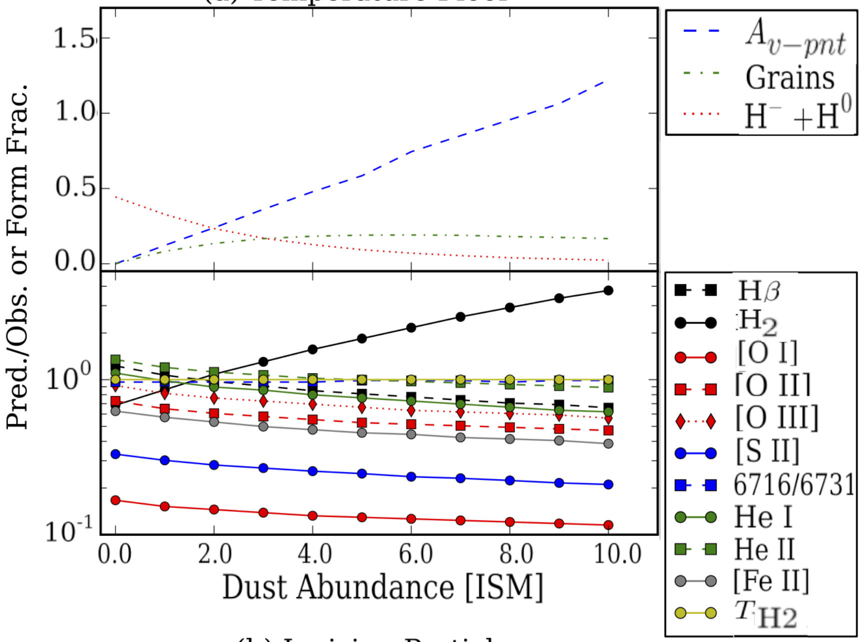

(b) Ionizing Particles

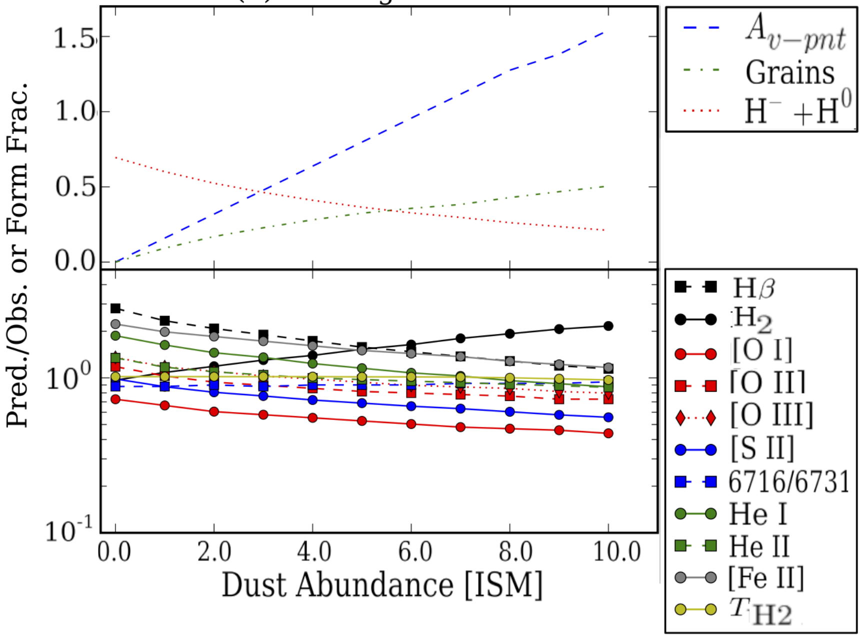

Figure 2.14 The sensitivity of several key parameters as a function of the grain abundance relative to the ISM grain abundance. The top panels show the formation fraction at the center of the knot due to the grain catalysis ("grains") and the $H^- + H_0$ formation routes and twice the predicted visual extinction A_{V-pnt} relative to the observed values. At a grain abundance of ∼3.0 times the ISM value, grain catalysis overtakes associative detachment in the temperature floor case. The bottom panels show the predicted over observed values for various quantities as a function of grain abundance.

with a variety of emission lines, and therefore do not deserve the same weight as the individual lines listed in the table. However, the predictions from the extra heating models are 25 times too low for the temperature floor model, within a factor of two for the ionizing particles model, and 14 times too high for the 5× dust model. We regard all of these as being satisfactory matches.

We briefly explored a model with no dust at all, to determine whether sufficient H_2 would be formed by routes not involving dust. Although it is clear that K51 must contain some amount of dust because we see dust absorption in the HST continuum image (§2.3), there are other H_2 knots in the Crab that do not have detectable dust absorption and which therefore might be described by such a model. As Figure 14 (bottom panels) shows, models without dust can still produce strong H_2 emission. For example, a dust-free model with density $n_{\rm core} = 10^{5.2}$ cm^{-3} at the center of the knot and a temperature floor is able to correctly reproduce the observed H_2 2.12 μm surface brightness and thermal H_2 spectrum. It underpredicts [N I] λ5198, [N II] λ6584, [O I] λ6300, and [S II] λ6720 by about the same amount as in the temperature floor model described above (in which dust is present at the ISM abundance). This dust-free model is not intended to describe K51, but it does show that in principle dust-free knots could form H_2 and produce strong H_2 emission.

2.4 Discussion

2.4.1 Understanding the H_2 Formation Environment

For both the temperature floor and the ionizing particle models, we find the surprising result that the strong H_2 emission comes from a region where hydrogen is predominantly atomic. The overwhelming reason is that the core is insufficiently shielded from the Balmer continuum to allow H_2 to fully form. The energetic photons penetrate into the core and produce a region where hydrogen is mainly atomic but there is a significant electron density.

The H_2 formation mechanism in this environment is primarily associative detachment ($H^- + H \rightarrow H_2 +^- e$). This is because the product of the electron density n_e and the hydrogen density n_H is large enough to allow H_2 formation to proceed faster by associative detachment rather than by the usual grain catalysis method ($2H + \text{grain} \rightarrow H_2 + \text{grain}$). For typical conditions present in the ISM at the H_0/H_2 interface,

$$\frac{r_H}{r_{\text{grain}}} = \frac{n_e \alpha_H}{n_H \alpha_{\text{grain}}} \approx 250 \frac{n_e}{n_H} \tag{2.1}$$

(Ferland et al. 1994 equation A10), where r_{grain} and r_H are the rates, and α_{grain} and $alpha_H$ are the rate coefficients for grain catalysis and associative detachment, respectively. For $n_e \ / \ n_H > 4 \times 10^{-3}$ associative detachment is faster than grain catalysis at forming H_2. In the cases we have considered in this paper, $n_e/n_H \sim 10^{-2}$ in the core of the knot, showing that associative detachment is dominant. This result will hold regardless of any changes to the abundances or $\phi(H)$. If we are overpredicting the H_2 emission due to uncertainties in the geometry, then the core density ncore would need to be lowered to compensate, producing a larger n_e/n_H and still favoring associative detachment.

2.4.2 Timescale Considerations

We have assumed that the age of the SNR is long enough for physical processes occurring in K51 to be in steady state. Here we discuss processes for which this is not true: (1) the known variability in the incident continuum spectrum due to high-energy gamma ray bursts; (2) the H_2 formation timescale; (3) the dynamical timescale; (4) the evaporation timescale.

The gamma-ray activity of the Crab is the quintessential example for high-energy plasma physics, and as such, has been the subject of several recent investigations (e.g. Abdo et al. 2011; Tavani et al 2011). In order to consider the most extreme case in which a gamma ray flare would alter the physical conditions in which H_2 forms, we have chosen an exceptionally energetic flare to compare with the total luminosity produced by the pulsar. Buehler et al. (2012) detected a gamma-ray burst that corresponds to a peak luminosity of $\sim 4 \times 10^{36}$ erg s^{-1}. However, that gamma-ray peak only corresponds to ∼5% of the total luminosity currently being injected into the nebula, after the luminosity responsible for acceleration of the filaments is removed. Such slight variations are negligible when considering the effects on the molecular knots.

Of greater concern is the H_2 formation timescale. In K51, this is set by the associative detachment reaction. The rate for this reaction is limited by the rate for radiative attachment, $H_0 + e^- \rightarrow H^- + \gamma$. Therefore, from Equation 1 the rate is given by $r_H = n_e \alpha_H$ where $\alpha_H = 8.861 \times 10^{-18} T_e^{0.663}$ is the rate coefficient for radiative attachment at the temperature in core of the Crab (Ferland et al. 1994). The electron (or kinetic) temperature in the core is very close to the H_2 temperature of 2800 K. The smallest electron density in the core is $\sim 7 \times 10^2$ cm^{-3} in the temperature floor case, and this will set the most extreme timescale. In this situation, $\tau_H = 1/r_H \sim 2.5 \times 10^4$ yr, which is much longer than the age of the Crab Nebula. This indicates that future calculations must include time dependent chemistry. We hope to explore the effects of a time-dependent calculation in a future paper.

Our extra-heating models are highly over-pressured in the core relative to the envelope of ionized gas, raising the question of how long such knots could survive. The sound crossing time is set by the sound speed in the core, $c_s = (kT/P_0 m_H)^{1/2} \sim 7.0 \times 10^5$ cm s^{-1}, and is $t_s \sim 1400$ yr, roughly the age of the Crab. However, the evaporation (or mass-loss) timescale is more physically relevant. Assuming that the heated gas in the ionized layer flows outward at the speed of sound in the ionized gas,

$c_{s-ion} \sim 1.4 \times 10^6$ cm s^{-1}, the mass loss rate is $dm/dt \sim 4\pi l_{knot}^2 c_{s-ion}\rho_{ion}$ where ρ_{ion} is the total mass density in the ionized skin. Using a total K51 mass of 2×10^{-3} $M_\odot$ (as found below in §4.6) gives $t_{pe} \sim m/(dm/dt) \sim 1800$ yr. Therefore, even if K51 formed instantaneously after the supernova explosion, it is reasonable that it has marginally survived.

A related possibility is a dynamical environment where dense seeds are ablated to produce the emission in a non-equilibrium flow. This is highly similar to the knots in the Helix planetary nebula (Henney et al. 2007).

2.4.3 Effects of Geometrical Uncertainty

We assumed a plane-parallel geometry for our modeling of K51, and compared our results to emergent line intensities deduced as if we were in fact measuring a plane parallel slab face-on. In reality, although K51 is the simplest case available, it has a complicated and poorly defined morphology. Our modeling does not intend to accurately describe all of the features present in K51. Instead, we offer a proof of concept model in which our main results hold regardless of the actual geometry. As an example of the uncertainties due to the poorly-known geometry, we consider the effects if the actual geometry were spherical as opposed to the assumed plane-parallel situation.

As described in §2.2, we determined an observed surface brightness for each emission line by taking the total flux measured from the knot and dividing by the knot's projected surface area on the sky. But a sphere of a given radius has two times more surface area than the front and back surfaces of a thin disk of the same radius, so the emergent energy per unit area would be two times smaller.

In our plane-parallel models, a simulation stopping halfway through the knot has an H_0/H_2 core that extends over a range of depth that is one-third the depth of the ionized zone, producing a core:ionized volume ratio of 1:3. But if this same dependence on depth into the cloud were true for a spherical cloud, the core:ionized volume ratio would become about 0.02. Thus, if our Cloudy results were adjusted to account for a spherical geometry, the predicted ratio of H_2:ionized surface brightness should be decreased by approximately a factor of 16.

An additional uncertainty comes from the ∼1 mag of internal extinction at visible wavelengths. If the knot is opaque to optical lines then emission lines coming from the rear half of the knot (which we assume to be illuminated from the rear side) would need a greater reddening correction. However, the knot is transparent to IR lines, thus, only half of the volume emitting optical lines from the ionized outer skin would be observed, while all of the H_2-emitting volume would be seen at NIR wavelengths. This would improve the fit for the ionizing particles case, since the overpredicted H^0 and He^0 visible wavelength lines originate mostly from the core, and on average would experience greater extinction than has been accounted for and hence would become weaker. Although in that case the $Br\gamma/H\beta$ ratio would no longer fit the Case B values, the measurement of the $Br\gamma$ line strength has considerable uncertainty and is not a tight constraint on our models.

These factors may or may not partially cancel each other out, but taking them into account would change our optimization of the abundances, of $\phi(H)$, and of the density law. However, we stress that such a reoptimization is unlikely to change our basic results about H_2 formation and the state of hydrogen in the core.

2.4.4 Are Models with Fully Molecular Cores Ruled Out?

In Papers I and III we presented estimates of the H_2 emissivity per H baryon based on the assumption that the emitting cores are fully molecular and are excited solely by collisions. We suggested that our H_2 survey selectively found molecular regions in which the temperature and density are in the range where H_2 has its highest emissivity. To create a fully molecular core, the internal extinction must be large to shield UV radiation from inducing dissociation (Tielens & Hollenbach 1985). As is discussed in Paper III, given the observed 2800 K H_2 temperature, the measured H_2 emission would need to come from a much smaller volume than is contained within the ∼1" diameter structures seen in our H_2 images, suggesting that the emission might come from either a thin shell around a completely obscured inner core or from dense sub-condensations with a very small volume filling factor.

Here, we have arrived at a very different picture. At least in the case of K51, the Crab SED is insufficiently shielded to neglect photodissociation. The two models which include additional excitation mechanisms produce an extended H^0 zone in which hydrogen is almost entirely atomic, not molecular, but has a sufficiently large column density so that the observed H_2 emission still can be produced within the observed volume of the knot. The measured H_2 emission comes from an atomic region that fills the volume of the knot, rather than from the fully molecular zone posited in Paper III.

However, the statistics suggest that other H_2 knots may well have fully molecular regions. In Paper II we found that the H_2 knots are predominately redshifted (34 have $v > 100$ km s^{-1} while only 7 have $v < -100$ km s^{-1}). This means that the knots we have detected in the H_2 line are on the back side of the expanding nebula, which has a systemic velocity near 0 km s^{-1}. Our translucent model does not account for this observation. A possible explanation is that in most H_2 knots the excitation is stronger on the side facing the pulsar and that a fully molecular zone with significant 2.12 μm extinction has formed on the side away from the pulsar, which for the missing blueshifted knots would be the side nearer to us.

In addition, some of the other knots found in our H_2 survey could turn out to be fully molecular gas that is optimally emitting in H_2 as suggested in Paper III. The extended very faint H_2 emission that seems to follow many of the large-scale filament structures (Paper II) could represent fully molecular regions with less than the maximum H_2 emissivity. There could also be additional discrete condensations of cooler molecular gas that do not produce detectable H_2 emission.

An important check on the possible existence of fully molecular gas will come from future mm-wavelength observations. Figure 15 compares the very different appearance of the mid-IR spectra expected from an extended H^0 zone of the type we propose for K51, and from a fully molecular core. For both cases we show the predicted spectrum from an H_2 knot, including the line emission, bound-free emission, free-free emission and dust continuum emission produced within the knot, together with the transmitted part of the incident synchrotron continuum. The mm-wavelength range in the fully molecular model (lower panel) has a spectrum rich with lines from CO, CS, HCN, and a host of other molecules, which are mostly absent in the temperature floor model (upper panel). As an example of the difference between the models, for the temperature floor and ionizing particle models the predicted strength of the CO $j = 1-0$ line at 2.6 mm is $\sim 10^7$ times fainter than H_2 2.12 μm. This corresponds to a flux of about 0.6 mJy km s^{-1}. For a line width of 20 km s^{-1} the peak brightness would be 0.05-0.24 mJy, which is very faint but probably just detectable with Atacama Large Millimeter Array (ALMA) if the line is narrow and all of the flux falls in one beam. In the fully molecular core case, the CO emission would instead come from a region where H_2 is not emissive because it is much cooler than the 2800 K that we found for K51, so for the same amount of H_2 emission the CO lines would be extremely bright.

In Paper III we suggested a model in which the H_2 emission comes from a thin, heated outer layer on a cool core of molecular gas. In that sort of picture, the column density through K51 of warmer (emitting) H_2 is 2×10^{18} cm^{-2}, and (based on the ratio of the knot diameter to the thickness of the H_2-emitting layer) the total column density including the cold (non-emitting) H_2 is roughly 2×10^{21} cm^{-2}. Using a conversion factor $X = 3 \times 10^{20}$ H_2 cm-2 (K km $s^{-1})^{-1}$ (Young & Scoville 1991), the surface brightness in the CO line should be about 7 K km s^{-1}. This is 104 times brighter than the previous case, so CO would be relatively easy to detect with current interferometers. However, this latter result assumes that the CO-emitting gas fills the entire volume corresponding to the observed 2" diameter of K51; a smaller filling factor (as is likely to be the case) would make the line much harder to detect. Also, the X-factor value is based on measurements of optically thick gas with typical ISM metallicities, so it is unclear how accurate it is for the case of the Crab. In spite of these two caveats, a deep CO measurement is likely to provide a critical test of our model.

2.4.5 The Role of Dust

Thermal emission from dust is clearly seen in the integrated continuum spectrum from the full Crab Nebula (Marsden et al. 1984). Temim et al. (2006, 2012) estimated the total dust mass associated with the filament system to be $10^{-3} - 10^{-2}$ $M_{\odot}$ while Gomez et al. (2012) estimated the range to be 0.26-0.68 $M_{\odot}$. Well-resolved dust absorption features are known to be present at a number of points across the Crab (Fesen & Blair 1990, Hester et al. 1990). Previous photoionization models of the filaments have yielded a dust to gas ratio estimate an order of magnitude above the ISM (Sankrit et al. 1998).

Our extra heating models correctly predict the shape of the observed thermal emission bump from dust in the Crab. The filled circles in the upper panel of Figure 2.15 (plotted on top of the temperature floor model) show observed points derived from Herschel, Spitzer, Wise and Planck images, taken from Table A1 of Gomez et al. (2012). The Gomez et al. (2012) results are integrated over an aperture that covers most of the Crab. They are corrected for the average line emission, but include a st--rong contribution from the unfiltered synchrotron emission. We adjusted their observed flux values by subtracting off the synchrotron component, scaling the remaining

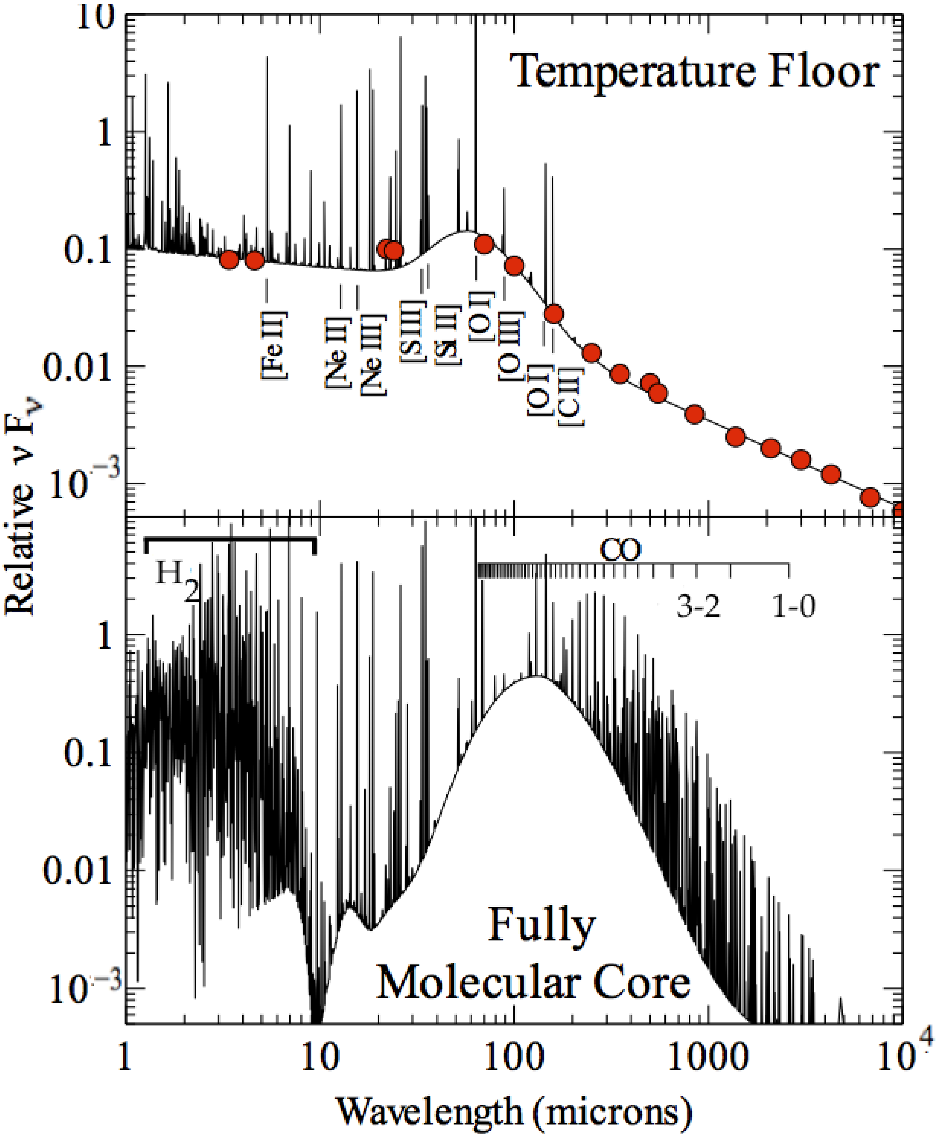

Figure 2.15 Predicted IR-mm wavelength spectra for the Temperature Floor model and for a typical fully molecular core, computed with Cloudy. Examples of the stronger atomic lines are marked in the upper panel, while the CO $\nu = 0$ lines and the region dominated by H_2 emission lines are marked in the lower panel. The region longward of 100 μm in the molecular core model includes strong lines of CO, CS, HCN, SiO, NH_3, H_2O, SO and NO. The red dots show the continuum emission summed over a wide area on the Crab as measured by Gomez et al. (2012), after adjusting their observations to match the underlying continuum shape not due to dust emission and also the height of the dust emission feature predicted for a single H_2 knot. This shows that our model correctly predicts the peak wavelength and width of the dust emission feature.

dust emission to match the height of our predicted dust emission, and finally adding back on the underlying continuum component predicted by our models. This means that the observed points at $\lambda < 10$ μm and $\lambda > 500$ μm have been forced to match our simulated spectrum, but that the points between those two wavelength limits show that the shape and peak wavelength of our predicted dust emission closely match the observations. This tests the dust temperature that is predicted by our models, but not the dust abundance. Our models predict that as a result of the assumed grain-size distribution and compositions, the dust will have a range of temperatures lying between 38 and 54 K. This is in reasonable agreement with the cold and hot components found by Gomez et al (2012), which had T_{dust} ~28 and 63 K, respectively.

While we do not have observations that allow us to directly constrain the dust abundance in K51, we explored the effects of varying this quantity in §3.6. The best model from this analysis arises from adopting a dust abundance five times greater than the ISM. This creates an environment in which H_2 forms at equal rates via grain catalysis and associative detachment, emphasizing the importance of less common H_2 formation routes even in dustier environments.

As was noted in §2.3, we assumed dust with optical properties that produce a rather low albedo. If we were to repeat the entire analysis using dust properties at the other end of the albedo range, we would correct the observed absorption dip to a significantly larger A_{V-pnt} value but then the models would also predict a larger A_{V-pnt}. The two A_{V-pnt} values should match about as well as they do for the dust properties assumed here, but there would be changes in the dusts effect on the internal structure of the knot and the emission line spectrum which we would expect to be fairly modest.

Are there dust-free knots in the Crab? Although K51 clearly contains dust, archival HST continuum images show that there are other H_2 knots that do not appear to be associated with specific dust absorption features. Therefore, it is possible that the observed dust emission originates only in some parts of the filamentary system, while other parts have no dust. The dust-free model briefly described in §3.6 represents a first pass at describing dense condensations in such regions. It is able to produce the observed 2.12 μm line in a unique environment in which grain catalysis, typically a primary mechanism for H_2 formation in the ISM, is absent and associative detachment is the only major H_2 formation mechanism. Our dust-free model is roughly as successful as the temperature floor model in describing the observed emission line intensities from K51.

2.4.6 Mass Estimate

Previous sections have developed a type of model that largely reproduces the observed emission from the ionized and molecular regions of K51. Here we use this model to estimate the total mass in the knot. Previous studies have used hydrogen recombination lines to estimate the mass of ionized gas, and H_2 lines to measure the mass in molecular regions. The latter is especially uncertain because we do not have any direct measurement of the density of the molecular core, and the derived mass depends on the density when the density is low.

We use our model to convert line intensities into a mass. In this approach, the model self consistently accounts for regions where hydrogen is ionized, molecular, and atomic. The latter can only be estimated with a model because there are no existing 21 cm detections of the knots[3]. The model reports the total column density required to produce the surface brightness in H I or H_2 lines, which we then rescale to subtract off the H+ zone. A surface brightness can then be converted directly into a column density and, if the size of the knot is known, into the total mass, for the atomic and molecular regions.

---

[3] The predicted 21 cm emission from Knot 51 would only be $\sim 10^{17}$ cm^{-2} K^{-1}, which is much too faint to be detectable with an instrument like the Expanded Very Large Array (EVLA).

We can use the temperature floor and/or ionizing particle model to estimate the total mass that is needed to produce the observed H_2 emission. To within 5%, the two models give the same result. Only a modest amount of H_2 is required, because the density and kinetic temperature in the extended H^0/ H_2 core are in the range over which H_2 will emit with nearly maximum efficiency (see Figure 5 of Paper III). However, both models predict that there will be a factor of 2000 times more H atoms present in the form of H^0 than in the form of H_2, which is a significant amount of mass that would not otherwise be detectable.

For K51 alone, using the ionizing particle model, the mass of H_2 is $m_{\mathrm{H2}} = 8 \times 10^{-7}$ $M_\odot$ while the total mass in the core including H^0 and the He and heavy elements in the H^0/ H_2 zone is $m_{core} = 2 \times 10^{-3}$ $M_\odot$. For the sum of all 55 H_2 knots reported in Paper II, scaling by the observed H_2 flux gives $m_{\mathrm{H2},total} = 4 \times 10^{-5}$ $M_\odot$ and $m_{core,total} = 0.1$ $M_\odot$. This assumes that the surface brightness to mass conversion factor derived for K51 applies to all knots. The latter value is an order of magnitude smaller than the estimate made by Fesen, Shull & Hurford (1997) based on the assumption that fully molecular cores were needed to explain the dust absorption features and H_2 emission known at that time. Combining our results with Fesen et al.(1997)'s estimate of 3.4 $M_\odot$ in the form of ionized and previously-known neutral gas, the H_0/ H_2 cores contribute about 5% of the total mass in the system of filaments.

In Paper II we noted very weak H_2 emission coming from many parts of the filaments outside of the catalogued H_2 knots, which could trace additional similar cores that do not efficiently emit H_2 because they do not have the optimum temperature and density for H_2 emission. These would not be counted in the above mass estimate. Figure 8 suggests that such cores would emit low surface-brightness [O I] and [S II] lines, but we have not run specific models of them.

There could also be additional cores that in fact *are* fully molecular. We ruled out such a possibility for the particular case of K51 because the H_2 spectrum predicted by our dense core model does not match the observations. But there could be other knots for which we do not have a NIR spectrum that in fact would be described by our dense core model, or there could be cores that are too cold to strongly emit H2 but which could be detected through CO observations.

2.4.7 Crucial Observational Questions

Further progress on understanding the H_2-emitting knots rests in part on filling in some missing key pieces of information. Here we describe four open questions that can be addressed in a practical way by new observations.

Where is the dust and what is the dust-to-gas ratio? As is discussed above, many H_2-emitting knots do not show accompanying dust absorption. Are they dust free? Dust absorption is seen in many locations where we have not been able to detect strong H_2 emission. What are the detailed correlations between the absorbing dust features and the H_2 emitting cores? We are currently using archival HST images to investigate this question, but the available continuum images do not fully sample HST's point spread function and have useful signal:noise ratio over only about 2/3 of the Crab. A survey to uniform depth over the full Crab at the higher spatial resolution offered by WFC3 would be very helpful.

What is the geometry? The existing H_2 images have only about 0.7" FWHM spatial resolution, which is insufficient to discern the exact relationship between the ionized and molecular regions. Observing the 2.12 μm line in K51 and a few other knots with an adaptive optics system on an 8 m-class telescope could produce images with spatial resolution similar to or better than the HST visible-wavelength narrow-band images, which would be a major improvement.

Does significant Hβ emission come from the same zone that emits H_2? Both of our models with extra heating say that it does. The available HST Hβ image (Fig. 2) is not nearly good enough to answer this question. A new HST Hβ image with high signal:noise ratio would directly test these models, which predict that the Hβ emission should largely trace the H_2 morphology, rather than coming from a surrounding sheath. It is important that K51 has a radial velocity that is measured to be close to zero, because this means that its emission lines fall within the velocity range covered by the HST narrow-band filters.

Finally, are there any fully molecular cores? CO observations are needed to search for these. Conversely, detection of strong CO emission from K51 would rule out our extra heating models (§4.4). We are currently carrying out a program using the Institut de Radioastronomie Millimetrique (IRAM) 30 m and Plateau de Bure telescopes for a preliminary search for CO emission from the Crab, but ALMA will be able to carry out a much deeper survey.

2.5 Conclusions

We have explored four different types of models of the regions in small knots within the Crab Nebula. Our goal is to simultaneously reproduce the classical optical emission lines and the exceptionally strong emission from H_2 that has a thermal distribution of populations. The first two of these models are powered only by the synchrotron radiation field and can be ruled out. This includes the pressure-balance model, which does not produce sufficiently strong H_2 emission from within the size scale of Knot 51, and the dense-core model, which can produce the necessary H_2 2.12 μm emission by secondary electron excitation but predicts a highly non-thermal H_2 spectrum. From those results we deduced that extra heating is needed in the core of the knot in order to excite the observed H_2 emission.

We considered two cases for this additional heating: generic heating by any mechanism (such as shocks or dissipative MHD waves) that is able to supply a heating rate of 2.5×10^{-16} ergs s^{-1} $cm{-}3$ (the temperature floor case), and as a specific heating mechanism, ionizing particles. As was discussed above, both of these models successfully reproduce the observed H_2 emission including both the surface brightness and the H_2 line strengths relative to each other. Both also successfully reproduce the forbidden lines from the more highly ionized ionized gas. The temperature floor case underpredicts the strengths of forbidden lines from neutral and low-ionization species while getting the recombination lines approximately right, while the ionizing particle case comes closer to correctly predicting the neutral and low-ionization forbidden lines but overpredicts the H I and He I recombination lines. The 5× dust model is able to also fit the observed A_{V-pnt} to within a factor of two while still tting the emission line surface brightnesses to the same accuracy that is achieved by the other two models, but at the price of adding the dust abundance as an additional free parameter. We conclude that all three of these models t the observations to within the error bars that are set by the uncertainties in the geometry

We have found that the dust content in our simulations can be varied appreciably, from dust free to a factor of 5 above ISM abundances, while still maintaining overall reasonable fits to the ionized, neutral and molecular line strengths. Thus, we can conclude that dust might play an important role in understanding certain knots but it is not necessary for all knots.

The goal of this paper has been a general exploration of the types of models that might be able to explain the strong, thermal H_2 emission seen coming from the molecular knots. This paper presents a progress report, not a fully accurate model. In that spirit, we conclude that the models with extra heating do in fact represent progress and are likely to be a guide to what is really happening in the H_2-emitting zone. We have ruled out one of the two cases (dense cores) proposed by G90, while the second, ionizing particles, remains a possibility.

We have found an unusual astrophysical environment, independent of the exact H_2 excitation mechanism, in which the relatively large n_e/n_{H} ratio allows H_2 to form most quickly through associative detachment rather than through grain catalysis.

There are only a few published descriptions of such environments (e.g. Ferland et al. 1994), and this paper presents a different look at the possible conditions in supernova remnants.

We have assumed that steady state holds in all of our models. In §4.6 we showed that in order to accurately understand the expected emission, future simulations including time dependent chemistry must be performed. Time dependent plasma / chemistry simulations in an environment like the Crab filaments have never been performed and this paper provides the basis for such an investigation. The existence of H_2 requires a dense core to provide shielding. The observed H_2 temperature shows that this would be highly overpressured relative to the envelope of ionized gas.

The mass contained in these extended H^0/H_2 zones is significant, amounting to about 0.1 $M_\odot$ for the sum of the 55 H_2-emitting knots reported in Paper II. This is about 5% of the total mass estimated to be in the form of ionized gas or in more conventional H^0 zones. The observed H_2 is producing the 2.12 μm line at essentially its peak emissivity per unit mass, so the Crab could easily include many additional extended H^0/ H_2 zones or fully molecular zones that are too cool to produce detectable H_2 lines; CO observations are needed to look for such gas.

Improved high-angular resolution, high signal-to-noise images are needed, especially in the visible continuum, in Hβ and in the H_2 2.12 μm line. These would better trace the morphological connections between the dust, the ionized gas, and the H_2. This would greatly improve our ability to discriminate between possible heating and H_2 excitation mechanisms. Finally, a survey of CO would provide the means to distinguish between models with dense molecular cores and our favored models, which include extra heating.

3 Interpreting the Ionization Sequence in Active Galactic Nuclei Emission Line Spectra

We investigate the physical cause of the great range in the ionization level seen in the spectra of narrow lined active galactic nuclei (AGN). We have used a recently developed technique called mean field independent component analysis (MFICA) to identify examples of individual SDSS galaxies whose spectra are not dominated by emission due to star formation. From these objects, we assembled high S/N ratio composite spectra into large subsets of similar objects, defining an ionization sequence that includes exceptionally low-ionization cases. This is our AGN sequence. We then used a local optimally emitting (LOC) cloud model to fit emission-line ratios in this sequence, including the weak lines that can be measured only in the co-added spectra. These weak line ratios provide consistency checks on the density, temperature, and ionizing continuum of Seyfert galaxies determined from strong-line ratios. After integrating over a wide range of clouds at different radii and densities, we find in our models that the radial extent of the NLR is the major parameter in determining the position of higher to moderate ionization AGN along our sequence, providing a physical interpretation for their systematic variation. Higher ionization AGN contain optimally emitting clouds that are more concentrated towards the central continuum source than in lower ionization AGN. We also find that the ionizing luminosity is probably anti-correlated with the NLR ionization level, and hence anticorrelated with the radial concentration of the NLR. This suggests that the ionization sequence might be an age sequence, where the low-ionization objects are older and have systematically cleared out their central regions by radiation pressure. The success with which we have fitted classical excitation mechanism diagnostics demonstrates the effectiveness of the MFICA technique in isolating AGN contributions to emission lines, which future studies can utilize to further investigate the structure of the NLR and the origin of emission.[1]

3.1 Introduction

The narrow line region (NLR) of active galactic nuclei (AGN) is a region of ionized and neutral gas generally classified by strong [N II] λ6584 and [O III] λ5007 emission. In contrast to the very small broad line region (BLR), the NLR is on the order of 10^2 pc in size and contains relatively low-density gas, with electron densities $n_e \sim 10^4 cm^{-3}$. However, the physical picture of the NLR is unclear as there are few resolved NLRs. An important route for advancing our understanding of this region is to compare observed emission-line strengths to the ones predicted by models simulating an entire NLR.

Diagrams constructed from emission-line intensity ratios are widely used for this sort of comparison. Early empirical work by Baldwin, Phillips and Terlevich (1981) pointed out the importance of the [O III] λ5007/ Hβ vs. [N II] λ6584/ Hα diagram (hereafter the BPT diagram) for classifying emission-line galaxies as either active galactic nuclei (AGN) or star forming (SF). The optical diagnostic diagrams presented in Veilleux and Osterbrock (1987; hereafter VO87) added further diagnostic intensity ratios that are minimally affected by reddening. More recent work has extended this method into the ultraviolet (UV) and infrared (IR) (Spinoglio & Malkan 1992; Allen, Dopita & Tsvetanov 1998; Sturm et al. 2002; Groves, Dopita & Sutherland 2004a,

---

[1] This chapter is almost entirely taken word for word from Richardson et al. (2013b)

2004b (hereafter G04a, G04b)). The class of low-ionization galaxies called LINERs (Heckmann 1980), which has also been studied in many papers, is characterized by very strong emission lines from neutral species and includes many objects which are well separated from both AGN and SF galaxies in the BPT and similar diagrams. However, there are other low-ionization galaxies called "transition" objects which merge down into the SF galaxies on such diagrams (Ho, Filippenko & Sargent 1993; Kauffmann et al 2003; Kewley et al 2006). Here, we study the relationship between this latter class of low-ionization AGN and typical higher-ionization Type II AGN.

There have been many studies using the observed intensity ratios to identify the ionization source in narrow line Seyferts and SF galaxies. Photoionization models have been remarkably successful in reproducing the observed emission-line ratios in high-ionization AGN (Ferguson et al. 1997 (hereafter F97); Komossa & Schulz 1997; G04b). The excitation mechanism for low-ionization narrow line regions in the region overlapping with SF galaxies remains uncertain and it is not even clear whether all such objects contain AGN. Photoionization models of AGN have focused on matching the emission from either high-excitation and low-excitation galaxies but none have attempted to simultaneously match both. Models that incorporate shock excitation (Dopita & Sutherland 1995, 1996) can account for LINERS but fail to fit high ionization AGN.

The structure of the NLR is another open question. Three different models that can reproduce the observed emission from the NLR of Seyferts are: (1) a combination of matter and ionization bounded clouds (Binette et al. 1996); (2) radiation pressure dominated dusty clouds (G04a); and (3) locally optimally-emitting clouds (F97; see also Komossa & Schulz 1997).

The model that combines matter- and ionization-bounded clouds is specified by the ratio of the solid angles subtended by matter-bounded and ionization-bounded clouds. The matter-bounded component is responsible for high ionization lines, namely He II $\lambda4686$, and the ionization-bounded component is responsible for low to intermediate ionization lines. The dusty, radiation-pressure-dominated model is based on the principle that radiation pressure incident on grains is sufficient to moderate the density, excitation and surface brightness of high ionization regions. Finally, the locally optimally emitting cloud (LOC) model assumes that the emission lines come from a vast sea of clouds distributed over a wide range of densities and radial distances from a central source of ionizing radiation and that the observed emission-line intensity ratios are the result of a powerful selection effect: emission lines are produced in clouds that optimally emit them.

Each of these models can successfully represent the NLR in at least some galaxies, but it is not clear whether any of them can explain all NLRs. The low-ionization AGN, which we include in this present study, fall in a region of the BPT diagram that is also occupied by low ionization SF galaxies (cf. Tanaka 2012a, 2012b). This overlap with SF cases greatly confuses the issue of whether or not one general type of model can explain the full sequence from low-ionization non-SF objects to the much more luminous high-ionization objects such as classical Seyfert galaxies. The low-ionization AGN may or may not include cases where the ionization is due to a composite non-thermal and SF spectrum. What is needed is an unbiased set of AGN that span the full ionization range.

In Allen et al. (2013; hereafter Paper I) we developed a new technique that is able to separate AGN from SF galaxies with much greater purity than is usually achieved with older methods such as those based on BPT diagrams or principal component analysis. This mean field independent component analysis (MFICA) technique allowed us to separate galaxies along a star-forming (SF) locus from those along an active galaxy (AGN) locus extending down to even quite low ionization levels. We used a sample of about 10^4 low redshift ($0.1 < z < 0.12$) SDSS emission-line galaxies to isolate sequences, or “loci,” of pure SF and of AGN cases.

First, the MFICA technique was used on small subsets of the full sample to generate five "continuum" and five "emission-line" components. We found that three of the emission-line components could be combined with various weightings to reproduce the spectra of any SF galaxy, while all five emission-line components were also needed in order to reproduce the AGN spectra. The relative strengths of the different emission-line components therefore specified the relative SF and AGN contributions to each galaxy's spectrum.

Next, the components were fitted to each member of the full sample of $\sim 10^4$ emission-line galaxies in a two-step process, first fitting and subtracting the continuum and then fitting the emission-line components. This produced a set of five emission-line component strengths for each galaxy in the full sample, which defined a five-dimensional parameter space. We then used an existing technique (Newberg & Yanni 1997) to identify two loci of galaxy points running through this parameter space, one corresponding to pure SF galaxies and the other to AGN.

Figure 3.1a shows the BPT diagram for the full sample of galaxies used in Paper I. The dashed curve is the boundary between SF and AGN defined by Kauffmann et al. (2003), while the solid line is the theoretical upper limit on SF line ratios found by Kewley et al. (2001). The diagonal line is the boundary between Seyferts and LINERs suggested by Kauffmann et al. (2003), although this definition was later refined (Kewley et al. 2006). Objects between the dashed and dotted lines may be a mix of SF, AGN and composite cases, introducing considerable confusion about the ionization mechanism over an extensive part of the full diagram. In contrast, Figure 3.1b displays a diagram that can be interpreted as a more abstract version of the BPT diagram. The three axes represent the contribution of the first three MFICA emission-line components (not including the AGN-only components) to each individual galaxy's spectrum, and shows how the SF and AGN loci from Paper I project into this particular parameter space. There is considerable separation between them except at the very lowest-ionization end of the AGN locus. This degree of separation shows that AGN galaxies fall along a single locus implying that their variation can be represented by a single free parameter.

The triangles on Fig 3.1a (discussed in more detail below) represent the spectra that we will analyze below, and show how the AGN sequence from Paper I maps back onto the BPT diagram. On this and other line-ratio diagrams, the AGN locus does not pass through the regions on line-ratio diagrams usually considered to be the realm of LINERs. Rather it starts out below the LINER region in the area occupied by transition objects, and then angles up into the AGN region.

The MFICA technique has picked out a sequence of AGN and has followed this sequence down into the transition object region, but in a way that rejects SF galaxies with similar emission-line spectra. Our hope is that we have separated out the "wheat from the chaff" in the transition zone. We can use this fact to gain a better understanding of how NLR properties change in response to changes in more basic AGN properties, over a wider range of parameter space than has previously been studied. Since the AGN sequence is mainly a monotonic progression along the AGN locus, a tantalizing possibility is that we may be able to find a single physical parameter that can be varied to determine the position of an individual object along sequence. As a check on this, we will also study objects that represent the observed scatter orthogonal to the AGN sequence. In §2 we describe composite observed spectra formed at five roughly equally spaced points along the MFICA AGN locus, and at two additional points to either side of the AGN sequence at each of those positions on the sequence. These composites range from very low ionization objects up through very highly ionized Type II AGN, and have sufficiently high signal:noise (S/N) ratios that many additional observed line ratios involving weak lines can be measured as consistency checks in addition to using the usual strong line ratios which have been used to constrain previous models. None of these composite spectra show any evidence of a non-thermal continuum, except for their emission lines. Then in §3, following F97 we adopt an LOC model and use it to reproduce the observational line-ratio diagrams. We investigate the sensitivity of the line ratios to various physical parameters. The physical interpretation of our results is discussed in §4, while §5 summarizes our conclusions. We will address the SF locus in a future paper.

3.2 A Comparison Sample at Representative Points Along the Locus

The clean separation of AGN from SF galaxies enabled by the technique developed in Paper I enables a deeper exploration of the NLR than has been possible in previous work. Our approach here is to use the MFICA technique to identify subsets of galaxies which are essentially AGN cases at five different, equally spaced points along central spine of the AGN locus, plus additional point to either side of the AGN locus. The continuum was fitted to and subtracted from each individual galaxy spectrum using the MFICA components, and then the continuum-subtracted AGN spectra within each subset were co-added in their rest frames. The subsets for these AGN are named aij, where the first index indicates the position along the AGN locus ranging from $i = 0$ at the low-ionization end to $i = 4$ at the high-ionization end. The second index is the position in a direction orthogonal to the AGN locus, with $j = 0$ corresponding to the "wing" closest to the SF sequence and $j = 2$ corresponding to "wing" further from the SF sequence. Figure 3.1 shows where these points (shown as triangles) fall on the conventional BPT diagram and also along the particular 3D projection of the AGN locus used in Figure 3.1b. Note that on the BPT diagram the lowest ionization subsets (a0j) fall very close to the line representing the Kauffmann et al. (2003) lower boundary for finding AGN and are well below the line representing the Kewley et al.

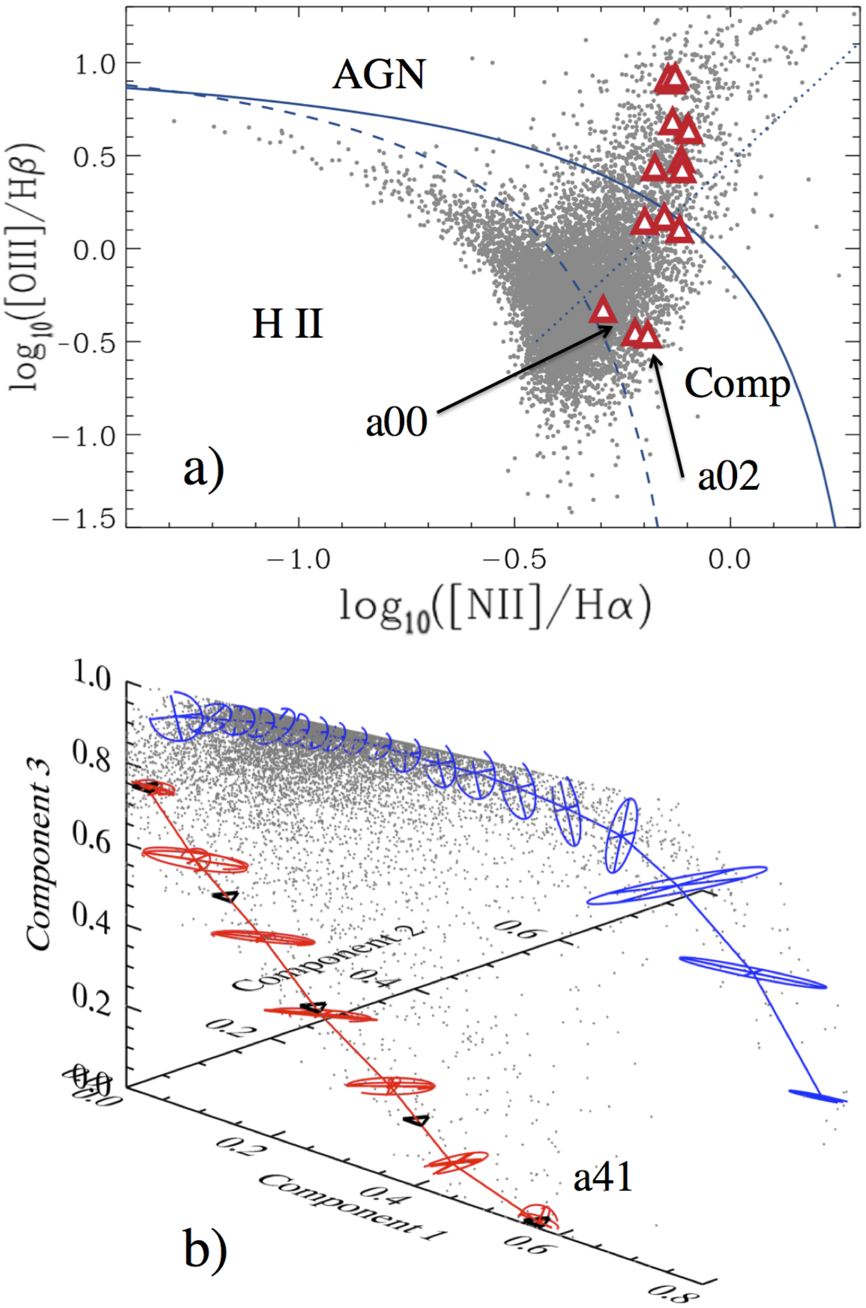

Figure 3.1 (Upper panel) The BPT diagram for our sample of galaxies from Paper I with classification curves Kauffmann et al. (2002; solid line), Kewley et al. (2001; dashed line) and Kauffmann et al. (2003; dotted line). The red triangles show our sequences of AGN picked out by MFICA with a4j representing the highest ionization observations. (Lower panel) The 3-D MFICA classification diagram with axes representing the strengths of the first three MFICA components. The ovals along each locus represent the range in galaxies still identified as AGN or pure SF, and the sequences described in the text as “wings” (ai1 and ai2) would follow the outer boundaries of these ovals for the AGN locus.

Table 3.1: Properties of aij subsets

Subset	a00	a01	a02	a10	a11	a12	a20	a21	a22	a30	a31	a32	a40	a41	a42
$E(B-V)$	0.80	0.83	0.68	0.43	0.49	0.56	0.40	0.43	0.45	0.30	0.33	0.39	0.20	0.20	0.21
Observed $L(\mathrm{H}\beta)^1$	1.8	2.1	2.4	2.0	2.2	2.6	3.1	2.9	3.2	3.1	2.4	2.8	2.9	2.9	2.8
Observed $L(5007)^1$	0.95	0.85	0.92	3.1	3.6	3.7	9.2	9.6	9.1	16.	12.	13.	24.	25.	24.
Dereddened $L(\mathrm{H}\beta)^1$	29.	38.	25.	9.0	12.	18.	12.	13.	15.	8.8	7.7	11.	5.9	5.9	5.7
Dereddened $L(5007)^1$	14.	14.	8.8	13.	18.	24.	35.	40.	41.	43.	35.	47	47.	49.	48.
Component weights															
Component 1	0.03	0.02	0.01	0.14	0.13	0.11	0.25	0.25	0.25	0.40	0.40	0.40	0.54	0.57	0.59
Component 2	0.02	0.01	0.01	0.01	0.01	0.02	0.02	0.01	0.01	0.00	0.01	0.01	0.01	0.00	0.00
Component 3	0.73	0.74	0.75	0.52	0.54	0.55	0.34	0.34	0.34	0.13	0.16	0.18	0.01	0.01	0.01
Component 4	0.09	0.17	0.24	0.16	0.34	0.32	0.17	0.26	0.35	0.22	0.30	0.38	0.22	0.26	0.29
Component 5	0.13	0.07	0.00	0.17	0.09	0.00	0.22	0.14	0.05	0.24	0.14	0.04	0.23	0.16	0.11

[1] Luminosities are in units 10^{40} erg s^{-1}.

(2001) upper limit for SF galaxies. Table 3.1 lists some general properties of these 15 aij subsets, each of which contains a sample of the 50 galaxies whose MFICA weights most closely matched the selected points along the AGN locus. The $E(B-V)$ values were determined from the Hα/Hβ intensity ratio as described below. We then list both the observed and dereddened luminosities of Hβ and [O III] λ5007. Finally, the table lists the relative weightings of each of the MFICA emission-line components when fitted to the coadded spectrum representing each individual subset along the AGN locus. Selected regions of the co-added spectra of the 5 central ($j = 1$) subsets are shown in Figure 3.2. The additional subsets ($j = 0, 2$) are not shown in Figure 3.2 due to their close similarity to the central subset.

We then measured emission-line strengths from the co-added spectrum for each subset. For most lines, we just integrated the flux within the line profile above a locally fitted continuum. The accuracy was about +/-5 per cent for the stronger lines ranging to +/-20 per cent for the weakest lines based on the S/N ratio in the adjacent continuum. We separated the [S II] doublet by simply dividing the blended profile at the lowest point between the two lines. He I λ5876 is on the wing of Na D, which is the one absorption feature in the underlying galaxy spectrum that obviously did not subtract off properly along with the rest of the continuum. Our He I λ5876 measurements are based on fitting the He I line with the profile of the Hβ emission line, with a typical uncertainty of about 10 per cent. Table 2a lists the observed (reddened) value, while Table 2b lists the dereddened values assuming a standard Galactic reddening curve with $E(B-V)$ chosen to produce dereddened $I(\mathrm{H}\alpha)/I(\mathrm{H}\beta) = 2.86$, appropriate for Case B recombination at $n_e = 10^2$ cm^{-3} and $T_e = 10^4$ K (Osterbrock & Ferland 2006; hereafter AGN3). The dereddened values are the ones used in the following analysis. The S/N obtained from co-adding spectra allows weak lines such as [S II] λ4070 (the sum of the [S II] $\lambda\lambda$4068,4076 doublet), [Ar IV] λ4711, [N I] λ5200, [N II] λ5755, He I λ6678 and [O II] λ7325 to be measured

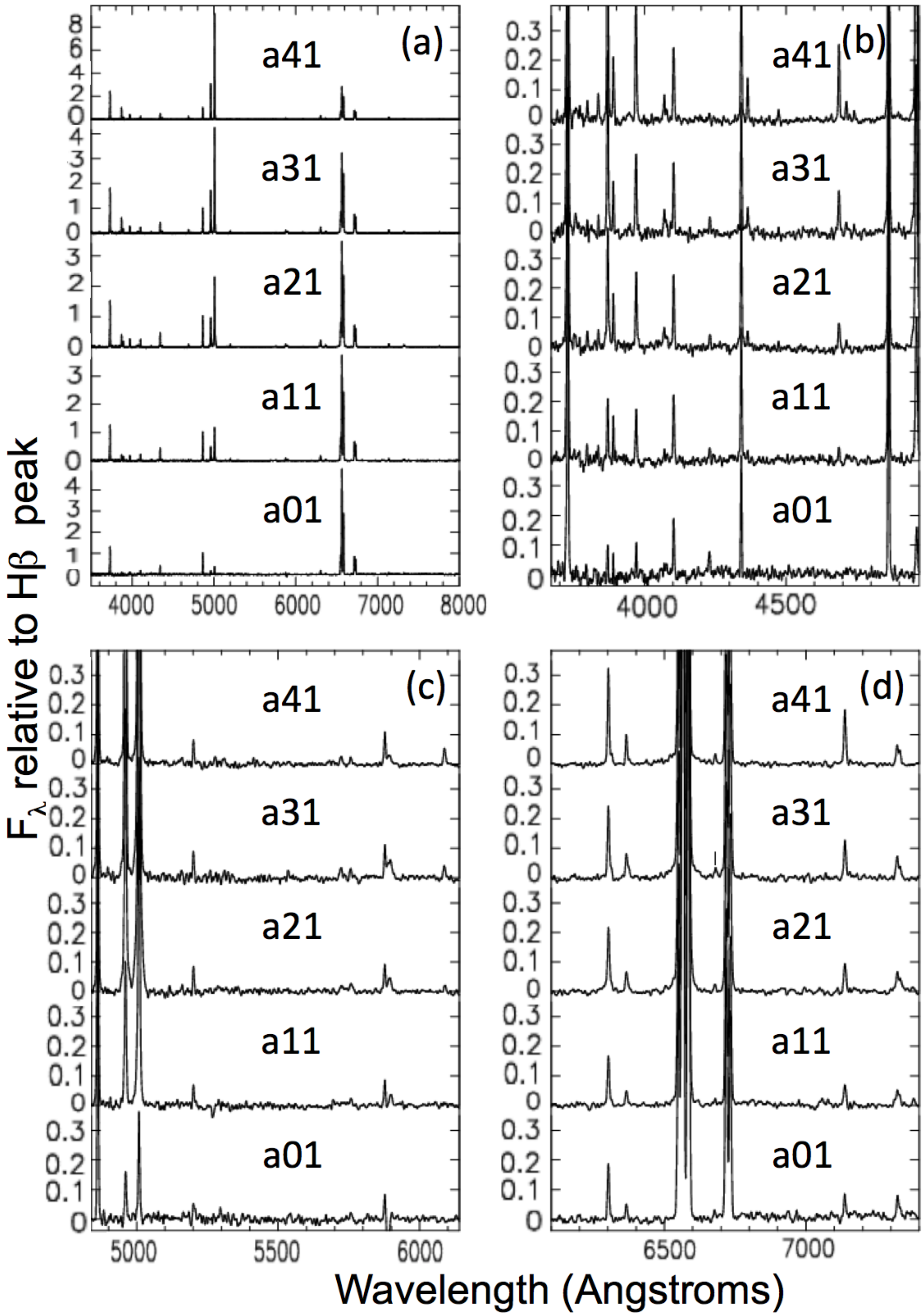

Figure 3.2 Observed, coadded spectra for the five subsets that fall directly along central the AGN locus. Panel (a) shows the full spectra. The other panels show enlargements that slightly overlap in wavelength. All flux values are shown in units of the peak Hβ intensity in the particular spectrum.

Table 3.2a: The measured emission line strengths for the AGN Locus. Measurements are relative to Hβ.

Ion	$\lambda_{\rm air}$	a00	a01	a02	a10	a11	a12	a20	a21	a22	a30	a31	a32	a40	a41	a42
[O II]	3727	1.47	1.43	1.18	1.48	1.30	1.31	1.78	1.58	1.48	2.05	1.82	1.71	2.48	2.37	2.35
H I	3798	<0.03	<0.04	<0.04	0.01	0.03	0.04	0.01	0.03	0.05	0.03	0.01	0.01	0.05	0.04	0.04
H I	3835	<0.01	<0.02	<0.05	0.02	0.02	0.03	0.01	0.03	0.04	0.03	0.01	0.02	0.08	0.07	0.08
[Ne III]	3869	0.10	0.02	0.08	0.16	0.17	0.18	0.41	0.42	0.38	0.57	0.54	0.56	0.78	0.79	0.81
H I	3889	0.04	0.03	0.08	0.11	0.09	0.11	0.14	0.14	0.14	0.13	0.13	0.14	0.16	0.16	0.16
[S II]	4070	0.12	0.06	0.04	0.07	0.03	0.01	0.10	0.13	0.11	0.11	0.10	0.08	0.12	0.11	0.11
H I	4102	0.17	0.14	0.18	0.18	0.17	0.20	0.21	0.20	0.20	0.19	0.20	0.19	0.22	0.21	0.21
[Fe V]?	4229	0.04	0.10	0.09	0.05	0.02	0.04	0.04	0.04	0.04	0.04	0.05	0.06	0.03	0.01	0.01
H I	4340	0.33	0.32	0.35	0.42	0.40	0.44	0.42	0.44	0.44	0.38	0.39	0.41	0.42	0.42	0.43
[O III]	4363	<0.07	<0.04	<0.04	0.05	0.04	0.08	0.07	0.07	0.07	0.10	0.11	0.13	0.11	0.12	0.12
He II	4686	<0.05	<0.01	<0.03	0.05	0.04	0.03	0.09	0.09	0.09	0.14	0.15	0.14	0.23	0.23	0.24
[Ar IV]	4711	<0.02	<0.02	<0.04	0.03	<0.02	<0.03	0.02	0.02	0.01	0.04	0.04	0.05	0.06	0.06	0.06
H I	4861	1.00	1.00	1.00	1.00	1.00	1.00	1.00	1.00	1.00	1.00	1.00	1.00	1.00	1.00	1.00
[O III]	4959	0.17	0.18	0.14	0.60	0.60	0.50	1.31	1.23	1.11	1.85	1.81	1.71	2.76	2.86	2.92
[O III]	5007	0.53	0.40	0.39	1.52	1.60	1.39	2.94	3.25	2.88	5.11	4.76	4.62	8.34	8.64	8.76

Figure 3.2a (cont'd)

Ion	$\lambda_{\rm air}$	a00	a01	a02	a10	a11	a12	a20	a21	a22	a30	a31	a32	a40	a41	a42
[N I]	5200	0.05	0.07	0.08	0.04	0.08	0.08	0.06	0.08	0.07	0.06	0.07	0.07	0.07	0.07	0.07
[N II]	5755	<0.07	<0.07	<0.04	<0.06	<0.07	<0.06	0.03	0.05	0.04	0.03	0.03	0.04	0.02	0.02	0.02
He I	5876	0.14	0.08	0.07	0.11	0.09	0.09	0.12	0.11	0.11	0.13	0.12	0.11	0.12	0.12	0.12
Fe VII	6087	<0.00	<0.01	<0.00	<0.01	<0.01	<0.01	0.02	0.03	0.03	0.04	0.05	0.07	0.08	0.08	0.08
[O I]	6300	0.24	0.25	0.16	0.23	0.23	0.22	0.33	0.35	0.31	0.35	0.31	0.33	0.40	0.40	0.40
[O I]	6363	0.10	0.06	0.04	0.07	0.06	0.06	0.10	0.10	0.10	0.11	0.13	0.14	0.11	0.11	0.11
[N II]	6548	1.05	1.35	1.30	0.91	1.15	1.40	0.97	1.20	1.35	1.03	1.19	1.34	0.94	0.95	0.98
H I	6563	6.58	6.79	5.82	4.49	4.73	5.11	4.35	4.45	4.58	3.92	4.03	4.29	3.51	3.52	3.54
[N II]	6584	3.36	4.13	3.78	2.85	3.34	3.92	2.92	3.44	3.55	2.88	3.22	3.45	2.58	2.54	2.64
He I	6678	0.04	0.03	0.02	0.02	0.02	0.04	0.04	0.03	0.03	0.04	0.04	0.03	0.04	0.04	0.04
[S II]	6716	1.25	1.21	0.89	0.90	0.86	0.86	0.93	0.93	0.88	0.97	0.94	0.92	1.01	0.96	0.96
[S II]	6731	0.98	1.01	0.76	0.76	0.76	0.75	0.80	0.83	0.78	0.85	0.84	0.82	0.85	0.81	0.81
[Ar III]	7135	0.08	0.10	0.06	0.09	0.09	0.09	0.14	0.14	0.14	0.19	0.18	0.18	0.25	0.25	0.25
[O II]	7325	0.13	0.12	0.07	0.08	0.13	0.17	0.16	0.19	0.13	0.16	0.15	0.16	0.15	0.16	0.16

Table 3.2b: The dereddened emission line strengths for the AGN locus. Measurements are relative to Hβ.

Ion	λ_{air}	a00	a01	a02	a10	a11	a12	a20	a21	a22	a30	a31	a32	a40	a41	a42
[O II]	3727	3.60	3.62	2.54	2.40	2.24	2.45	2.79	2.54	2.46	2.88	2.63	2.64	3.10	2.97	2.96
H I	3798	<0.07	<0.09	<0.07	0.01	0.05	0.07	0.02	0.05	0.08	0.05	0.02	0.02	0.06	0.06	0.06
H I	3835	<0.03	<0.04	<0.10	0.03	0.04	0.06	0.01	0.05	0.06	0.05	0.02	0.04	0.09	0.09	0.10
[Ne III]	3869	0.22	0.04	0.17	0.25	0.28	0.31	0.62	0.64	0.60	0.77	0.76	0.83	0.96	0.97	1.00
H I	3889	0.08	0.07	0.15	0.17	0.15	0.19	0.22	0.22	0.22	0.17	0.18	0.21	0.20	0.19	0.20
[S II]	4070	0.23	0.12	0.07	0.10	0.05	0.02	0.14	0.18	0.16	0.14	0.13	0.11	0.14	0.13	0.13
H I	4102	0.32	0.27	0.31	0.25	0.25	0.31	0.29	0.28	0.29	0.24	0.25	0.26	0.25	0.25	0.25
[Fe V]?	4229	0.06	0.18	0.15	0.06	0.03	0.06	0.05	0.05	0.06	0.04	0.07	0.07	0.03	0.02	0.01
H I	4340	0.50	0.51	0.51	0.53	0.52	0.59	0.53	0.56	0.56	0.45	0.46	0.51	0.47	0.47	0.48
[O III]	4363	<0.10	<0.06	<0.06	0.06	0.05	0.10	0.09	0.09	0.09	0.12	0.13	0.16	0.12	0.13	0.13
He II	4686	<0.06	<0.01	<0.03	0.05	0.04	0.03	0.10	0.10	0.10	0.15	0.16	0.15	0.24	0.24	0.24
[Ar IV]	4711	<0.02	<0.02	<0.05	0.04	<0.03	<0.04	0.03	0.02	0.01	0.04	0.04	0.05	0.06	0.06	0.06
H I	4861	1.00	1.00	1.00	1.00	1.00	1.00	1.00	1.00	1.00	1.00	1.00	1.00	1.00	1.00	1.00
[O III]	4959	0.16	0.16	0.13	0.58	0.57	0.47	1.26	1.18	1.07	1.80	1.76	1.65	2.71	2.81	2.87
[O III]	5007	0.48	0.36	0.35	1.43	1.50	1.29	2.78	3.07	2.71	4.91	4.56	4.39	8.12	8.41	8.53

Figure 3.2b (cont'd)

Ion	λ_{air}	a00	a01	a02	a10	a11	a12	a20	a21	a22	a30	a31	a32	a40	a41	a42
[N I]	5200	0.04	0.05	0.06	0.04	0.07	0.07	0.06	0.07	0.06	0.05	0.07	0.06	0.06	0.06	0.07
[N II]	5755	<0.04	<0.04	<0.02	<0.04	<0.05	0.04	0.03	0.04	0.03	0.03	0.03	0.03	0.02	0.02	0.02
He I	5876	0.08	0.04	0.04	0.08	0.06	0.06	0.09	0.08	0.08	0.10	0.10	0.09	0.11	0.10	0.10
Fe VII	6087	<0.01	0.01	<0.01	0.01	<0.01	<0.01	0.02	0.02	0.02	0.03	0.05	0.07	0.07	0.07	0.08
[O I]	6300	0.11	0.12	0.09	0.15	0.15	0.13	0.23	0.23	0.21	0.26	0.23	0.23	0.33	0.34	0.33
[O I]	6363	0.05	0.03	0.02	0.05	0.04	0.03	0.07	0.07	0.07	0.08	0.09	0.10	0.09	0.09	0.09
[N II]	6548	0.46	0.57	0.64	0.58	0.70	0.79	0.64	0.77	0.85	0.75	0.85	0.90	0.77	0.77	0.79
H I	6563	2.86	2.86	2.86	2.86	2.86	2.86	2.86	2.86	2.86	2.86	2.86	2.86	2.86	2.86	2.86
[N II]	6584	1.45	1.72	1.84	1.81	2.01	2.18	1.91	2.20	2.21	2.10	2.28	2.29	2.09	2.05	2.13
He I	6678	0.02	0.01	0.01	0.01	0.01	0.02	0.02	0.02	0.02	0.03	0.03	0.02	0.03	0.03	0.03
[S II]	6716	0.51	0.48	0.41	0.56	0.50	0.46	0.60	0.58	0.53	0.69	0.65	0.59	0.81	0.76	0.77
[S II]	6731	0.40	0.40	0.35	0.46	0.44	0.40	0.51	0.52	0.47	0.60	0.58	0.53	0.68	0.64	0.65
[Ar III]	7135	0.03	0.03	0.02	0.05	0.05	0.05	0.08	0.08	0.08	0.13	0.12	0.11	0.19	0.19	0.19
[O II]	7325	0.04	0.04	0.03	0.05	0.06	0.08	0.09	0.10	0.07	0.10	0.10	0.09	0.11	0.11	0.11

in most cases, providing important consistency checks on our models.

3.3 Modeling the Narrow Line Region

3.3.1 Method

We used the LOC model, which treats the NLR as the sum of a large number of separate gas clouds spread out around a central ionizing source (Baldwin et al 1995). Once the incident spectral energy distribution (SED) and the chemical abundances are set, the major free parameters in the LOC model are the distributions of the individual clouds in their radial distances r from the source of ionizing radiation, and in their gas densities n_{H}.

The individual clouds were modeled using version 10.0 of the plasma simulation code Cloudy (Ferland et al. 1998). For simplicity, we assumed that there is no ISM attenuation of the AGN continuum radiation incident on the clouds. The consequences of this are described in F97. We used constant density models; the results of Pellegrini et al. (2007) show that constant-density and constant-pressure models give very nearly the same result for optical lines, which form in the warm gas within the H^{+} zone. The distinction is mainly important for infrared lines which form in cool atomic gas and which are not considered here. We used the solar abundances summarized in G04a, taken from a series of papers by Asplund and his collaborators (Asplund et al. 2000; Asplund 2000, 2003; Allende Prieto et al. 2001, 2002). Abundances for additional elements not given by G04a are taken from F97. Following F97, we used an ionizing luminosity $L_{\mathrm{ion}} = 10^{43.5}$ erg s^{-1}, typical of Seyfert galaxies. Our simulations proceeded until the electron temperature fell below 4000 K or above 10^5 K. Gas below 4000 K does not significantly contribute to optical emission lines, although it does produce infrared lines, and gas above 10^5 K contributes principally to X-Rays. These models did not include any cosmic rays. The Cloudy models all terminate before reaching molecular regions where cosmic ray ionization from the Galactic background becomes important. Komossa & Schulz (1997) studied the effect of adding the standard Galactic cosmic ray background to similar models, and found that the emission line ratios changed by only 1 per cent.

A series of grids of individual clouds were computed over a range of densities and radii that represent plausible values for gas in the NLR. Each grid consisted of 7171 cloud models. The radial distance from the ionizing source to the individual cloud, r, was varied in 0.1 dex steps from 10^{16} to 10^{23} cm and the hydrogen density, $n_{\rm H}$, was varied in 0.1 dex steps from 10^{0} to 10^{10} cm^{-3}. We assumed that the ionizing flux was isotropic so that a difference in radii reflects a difference in flux proportional to r^{-2}. Differences in Lion would appear as a rescaling of the radial distances by $(L_{\rm ion}/10^{43.5})^{1/2}$. The total hydrogen density was kept constant for each individual cloud but the molecular and electron densities were determined self-consistently and so vary with depth. The results from these grids are shown below in terms of the equivalent width of various emission lines, relative to the continuum level at 4860Å, which indicates the efficiency of each cloud in reprocessing the continuum into a particular emission line.

We computed both dust-free and dusty grids of clouds. By "dusty", we mean LOC grids that include dust in the individual clouds in parts of the NLR where it is not expected to have been sublimated, while "dust free" refers to LOC grids with no dust anywhere. Dust is difficult to accurately model in a physically consistent way, since sublimation occurs at small distances from the central object, so following F97 we adopted a step function in our dusty grids to artificially account for this process. We used a mix of graphite and carbonaceous grains and a grain size distribution typical of an H II region (Baldwin et al. 1991). At $r \leq 10^{16.9}$ cm the grain temperature is high enough to sublimate both types of grains so our models were dust-free with solar abundances. For $10^{16.9} < r \leq 10^{17.6}$ cm, the silicates are too hot to exist, so we included only graphite grains and used a solar composition, except for carbon which was depleted by 15 per cent. Finally, for $r \geq 10^{17.6}$ cm, we include both graphite and carbonaceous grains and adopt Orion Nebula abundances (Baldwin et al. 1996) that are typical of an H II region. This is the procedure used by F97. In reality, different sized grains sublimate at different temperatures. However, we followed F97 and ignored this effect, assuming that there is threshold radius for each grain composition after which those particular grains are allowed to form.

The LOC model is based on the fact that different emission lines are optimally emitted in different individual clouds according to the correct density and incident flux for efficient production of each particular line, while we observe only the integrated spectrum of the ensemble of clouds. This gives rise to a powerful selection effect in which the overall radial and density distributions of the clouds largely determines the measured spectrum. As in F97 (see also Baldwin et al. 1995), we modeled the total emitted spectrum integrated over radial distance and density distributions defined as $f(r) \propto r^{\gamma}$ and $g(n) \propto n_{\mathrm{H}}^{\beta}$, respectively, where γ and β are free parameters. An average spectrum over many galaxies as we have produced here is more likely to be correctly described by a broad power-law distribution than might be the case for an individual galaxy. The total luminosity of the line is then,

$$L_{\mathrm{line}} \propto \int \int r^2 F(r, n_{\mathrm{H}}) r^{\gamma} n_{\mathrm{H}}^{\beta} dn_{\mathrm{H}} dr \tag{3.1}$$

where $F(r, n_{\mathrm{H}})$ is the flux of the line and $r^{\gamma} n_{\mathrm{H}}^{\beta}$ is the spatial distribution function (Bottorff et al. 2002). Throughout the remainder of the paper, when the log of densities and radii are given, the units are cm^{-3} and cm, respectively. We chose the integration limits to include the range of parameter space that is physically relevant for the NLR. Gas with densities $\log(n_{\mathrm{H}}) > 8$ is above the maximum critical density for optical forbidden lines. Gas at radii $\log(r) < 17.48$ would either be much too hot to produce strong optical emission lines, or would have high density which would suppress the forbidden lines. Gas with densities $\log(n_{\rm H}) < 2.0$ does not optimally emit many lines, the notable exception being [S II] λ6720. This is the justification for the integration limits used by F97.

We experimented with changing the integration limits to include a larger range, but this only produces small changes to the integrated spectrum. Changes in the abundances, the SED, γ or β all produced much more noticeable effects. For this reason, we will only present integrations within the limits $2< \log(n_{\rm H} < 8$ and $17.48 <\log(r) <23$.

We compared the observed integrated predictions to the predictions by using line-ratio diagrams as in Baldwin, Phillips & Terlevich (1981), Villeaux & Osterbrock (1987), and elsewhere. We discuss these diagrams below. We will exclusively describe dust-free LOC grids until §3.6 where we address the fact that our dusty models do not fit some of the AGN subsets as well as our dust free models.

3.3.2 Spectral Energy Distribution Optimization

The SED in AGN is uncertain. The various forms of the incident continuum assumed in previous work include simple power laws, $f_\nu \propto \nu^{\alpha}$,(Binette et al. 1996, G04a), a combination of power law and blackbody continua (Komossa & Schulz 1997) and multi-component distributions (F97). In addition, the SED viewed by the BLR (Korista et al. 1997) may be different than the SED viewed by the NLR, and parts of the SED, such as emission originating from a dusty torus are only visible for AGN at certain viewing angles. We adopted a multi-component approach as in F97 and used He I/H I line intensity ratios to infer the SED.

We considered the three different spectral energy distributions (SEDs) shown in Fig. 3. They all have the general form,

$$f_\nu \propto \nu^{\alpha_{\rm uv}} e^{-h\nu/kT_{\rm cut}-kT_{\rm IR}/h\nu} + C\nu^{\alpha x} \tag{3.2}$$

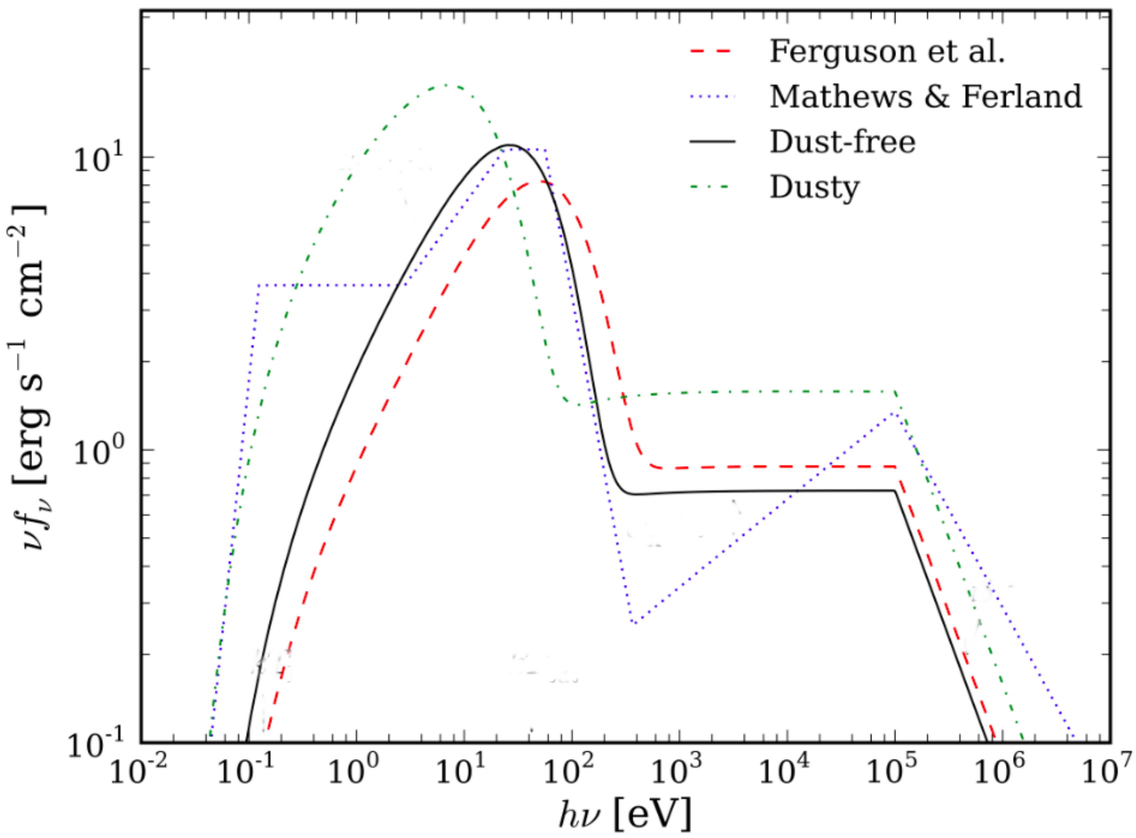

Figure 3.3 The SEDs for Ferguson et al. (1997), Mathews and Ferland (1987), our best model (dust-free) and our dusty model. Our optimized models result from an SED that has a shifted UV "Big Bump" in order to match He II λ4686, a well known indicator of the SED.

where $\alpha_{\rm uv}$ is the low-energy slope of the "big bump," $T_{\rm cut}$ is the UV temperature cutoff, $T_{\rm IR}$ is the IR temperature cutoff, C is a normalizing constant, and α_x is the slope of the X-ray component. The factor C sets the scaling between the big bump and the X-ray power law, and in Cloudy is determined by specifying α_{ox}, which is given by,

$$\frac{f_\nu(2\text{keV})}{f_\nu(2500\text{Å})} = 403.3^{\alpha_{ox}} \tag{3.3}$$

(Korista et al. 1997). The last term of Equation 3.2 was assumed to fall off as ν^{-2} above 100 keV.

A commonly used AGN SED is given by Mathews & Ferland (1987; hereafter MF87), and is shown as a dotted line in Figure 3.3. A combination of direct observations, with inferences based on the emission-line spectrum, determined the components of this SED. The X-ray slope of the SED, $\alpha_x \sim -0.7$, is typical for radio-loud AGN (Zamorani et al. 1981). As we describe below, this has a significant effect on the equivalent width contours but minimally affects the LOC integrations. F97 used a modified SED, shown on Figure 3.3 as the dashed line. This SED differs from that of MF87 in that it lacks infrared emission from a dusty torus, includes a soft X-ray component, and has a softer X-ray slope $\alpha_x \sim -1.0$ that is typical of radio quiet quasars and AGN (Elvis et al. 1994).

The He II λ4686/Hβ intensity ratio is an important test of these possible SEDs, because (1) He II and Hβ are recombination lines and therefore less sensitive to T_e than collisionally excited lines (AGN3); (2) the ratio is relatively insensitive to large changes in the ionization parameter (Binette, Courvoisier & Robinson 1988). Photoionization models of AGN often underpredict this ratio (Ferland & Osterbrock 1986).

Using the F97 and MF87 SEDs, we computed two separate grids of Cloudy models as outlined in §3.1, and then ran LOC integrations. The predicted [O III] λ5007/Hβ vs He II λ4686/Hβ line ratio diagrams for our dust-free LOC models using each of these SEDs are shown in the upper two panels of Figure 3.4 as colored lines connecting a series of circles. Each line represents the LOC results for a different density weighting in the range $-1.8 \leq \beta \leq -0.6$ with the different lines corresponding to increments in β of -0.4. Along each individual line the radial weighting is varied over the range $-2.0 \leq \gamma \leq 2.0$, and the circles along the line represent different LOC models run at increments in γ of 0.25. The circles with white centers represent the best-fitting LOC models described below in § 3.5. The black diamonds, triangles and squares represe-

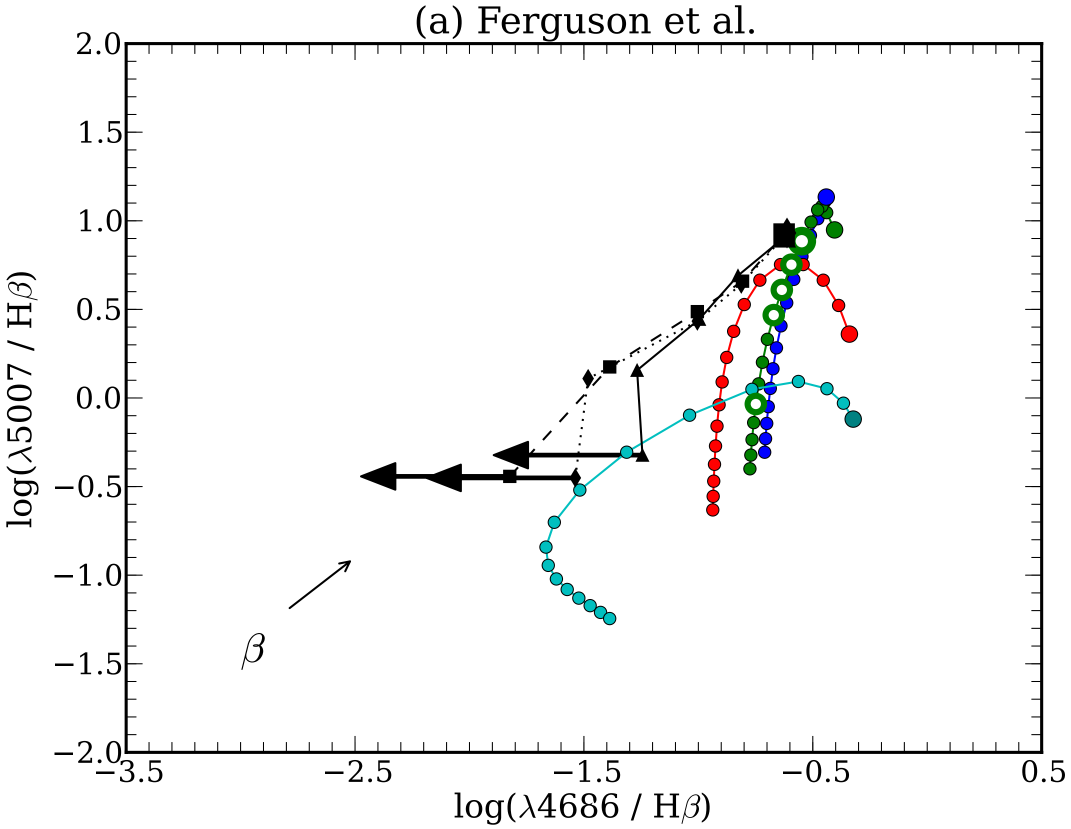

Figure 3.4 The He II $\lambda4686$ /Hβ line ratio for various SEDs: Ferguson et al. (top left panel), Mathews and Ferland (top right panel), and our optimized SED (lower panel). In each panel the triangles connected by the solid black line are the dereddened measurements from the co-added spectra that constitute the a40-a30-a20-a10-a00 sequence. Similarly, the squares connected by the dashed black line show the a41-a31-a21-a11-a01 sequence, and the diamonds connected by the dotted black line show the a42-a32-a22-a12-a02 sequence. The largest shape in each sequence indicates observations at the top of AGN locus (a40, a41, a42). The colored lines with circles represent LOC integrations. The density-weighting indices in the LOC integrations, β, have more negative values along the direction of the arrow and are indicated by different colors. The radial weighting indices, β, become more negative as a function of increasing distance from the largest colored circle for each particular density weighting. The hollow circles indicate our best fitting set of free parameters, with the largest hollow circle indicating our best fit to the a41 subset (large black square). The cross in the corner of the plot located in the lower right corner of the bottom row indicates the range of acceptable error. The He II $\lambda4686$ /Hβ line ratio successfully matches the higher to moderate ionization AGN subsets within a factor of two for our optimized SED and the Mathews and Ferland SED.

Figure 3.4 (cont'd)

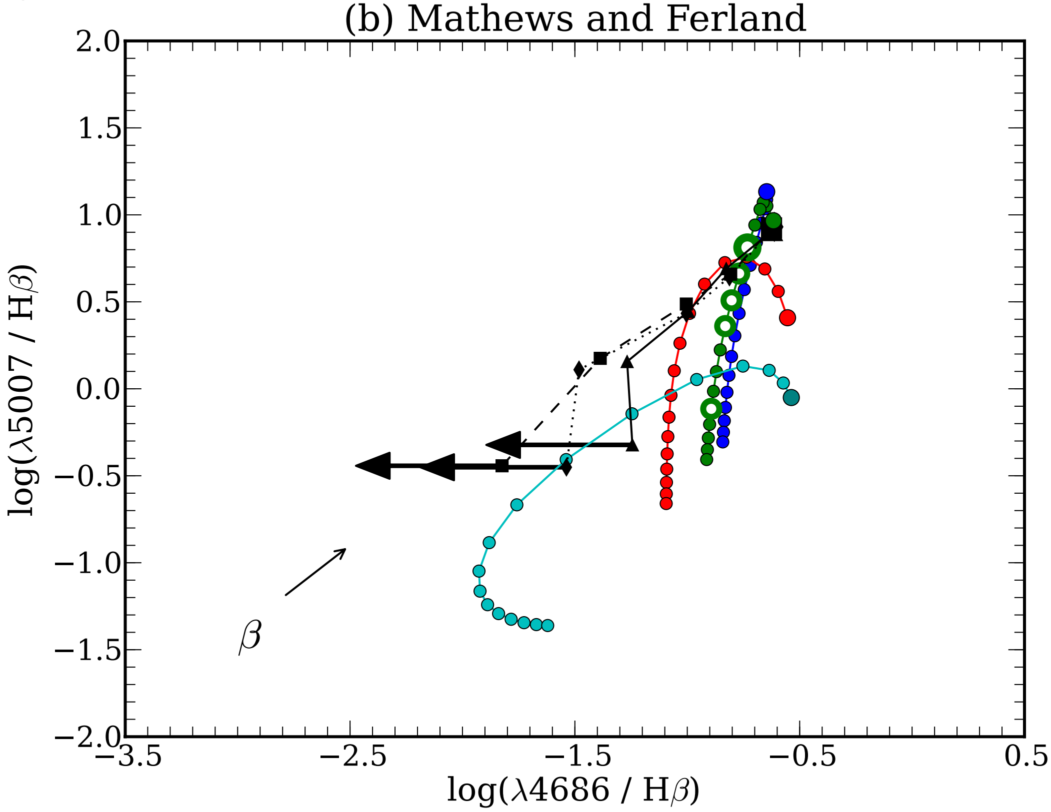

Figure 3.4 (cont'd)

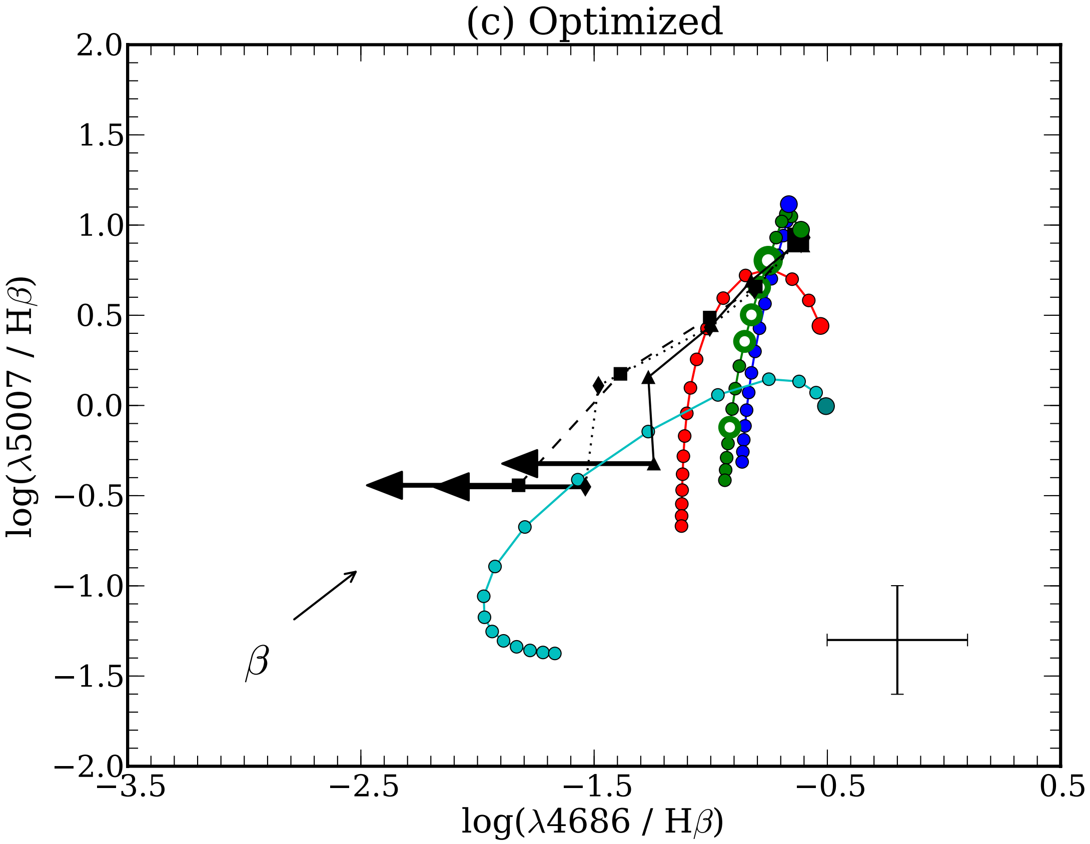

-nt the ratios measured from the AGN observations, with each sequence in the observations indicated by a different line style and symbol. The largest of these symbols represents the top of the AGN locus for that sequence. The largest symbol should be compared to the largest white-filled circle, which represents our best-matching LOC result for the high ionization end of the observed sequence.

While in Figure 3.4 and in other similar figures discussed below we have shown all three observed AGN sequences (the central ai1 locus and the two “wings” corresponding to ai0 and ai2), all of the sequences are very similar. In fact, even in the full set of line ratio diagrams described below the difference between each sequence is so slight that we cannot determine a physically meaningful interpretation for the wings; they appear to just represent object-to-object scatter about the central locus. For this reason, we compare our models only to the central locus.

It can be seen that the higher-ionization observed points in the upper two panels of Fig. 4 are in good agreement with the calculated curves. However for the F97 SED, the models producing integrated spectra with moderate [O III] $\lambda5007/\mathrm{H}\beta$ ratios (moderate ionization) overpredict the He II/Hβ ratios by almost a factor of three. In contrast, the MF87 SED produces a He II/Hβ ratio within a factor of 2. This is closely related to the "Stoy method" of determining the SED (AGN3) and we adjust its hardness to reproduce the ratio. Here and throughout the paper, we adopt a factor of 2 as our criterion for an acceptable fit between the predicted and observed line ratios, taking into account the uncertainty in the measurements of the weaker lines, the uncertainties (and object to object scatter) in the SED and abundances, and the fact that the LOC models just use simplified power laws to describe the distributions of r and n_{H}.

We optimized a third SED, shown on Figure 3.3 as the solid line, to try to produce a better fit to the measurements from our galaxy sample. In addition to a SED similar to radio-loud quasars (MF87), we wanted one that was typical of AGN (F97) but that still matched the moderate ionization He II/Hβ ratio. To achieve this, we modified the F97 SED by shifting the "big bump" until the He II/Hβ ratio matched the moderate to high ionization subsets. This modified "bump" turned out to match the one in the MF97 SED. We also adjusted α_{ox} to give closer agreement with the mean value of -1.4 found in AGN (Zamorani et al. 1981; Steffen et al. 2006).

Our optimized SED is characterized by $T_{\mathrm{cut}} \sim 4.2 \times 10^5$ K, $\alpha_{\mathrm{UV}} = -0.3$, $\alpha_{ox} = -1.35$, $\alpha_x = -1.0$, and $kT_{\mathrm{IR}} = 0.14$ eV. The bottom panel of Figure 3.4 verifies the fit to the moderate and high-ionization He II/Hβ ratio. Further adjustments were made to match the lower ionization He II/Hβ ratios but we were unable to simultaneously account for both the lower and upper end of the locus. By matching the higher and moderate ionization He II $\lambda4686/\mathrm{H}\beta$ ratios to within a factor of two, we were able to vast majority of our SED-indicating line-ratios ([O II] $\lambda3727$/ [O III] $\lambda5007$, He II

λ4686/Hβ, [O I] λ6300 /[O III] λ5007, He II λ4686/ He I λ5876 and [N I] λ5200/ [N II] λ6584) to within a factor of two without further tweaking, including many ratios at lower ionization. The MF87 and our optimized SED give essentially identical fits to the observed points on Figure 3.4, which are slightly better than the fit for the F97 SED. We chose to use the optimized SED for the remainder of our analysis.

3.3.3 X-ray Effects

Figure 3.5 shows that the peak emissivity of some strong lines occurs at two locations on the LOC plane for the Mathews & Ferland (1987) AGN continuum, but the Ferguson et al. (1997) continuum only creates a single maximum. We found that this is caused by the different assumptions in the form of the X-ray continuum. The emission-line equivalent widths indicate the efficiency with which individual clouds convert continuum radiation into emission lines, and, as Figure 3.5 shows, are generally similar for each of the SEDs shown in Figure 3.3. In high density, high incident-flux (low-r) environments, the equivalent width contours of these lines become smeared out over a larger range of parameter space. In the case of the Mathews and Ferland SED, these regions become isolated and form a second optimally emitting region.

By introducing gradual changes to the MF87 SED until it resembled the F97 SED, we were able to determine that the shape of the continuum at energies greater than 1 keV is responsible for creating the second optimally emitting region. The infrared-wavelength "shelf" in the MF87 SED represents emission from the torus and does not affect the equivalent widths. The densities at which the second optimally emitting regions occur are most likely larger than those physically relevant to the NLR, however X-ray effects are important in other contexts of AGN (e.g. in the BLR). It is important to note that the thicknesses through some of the clouds in these optimally emitting regions became comparable to their distance from the source. While F97 did not

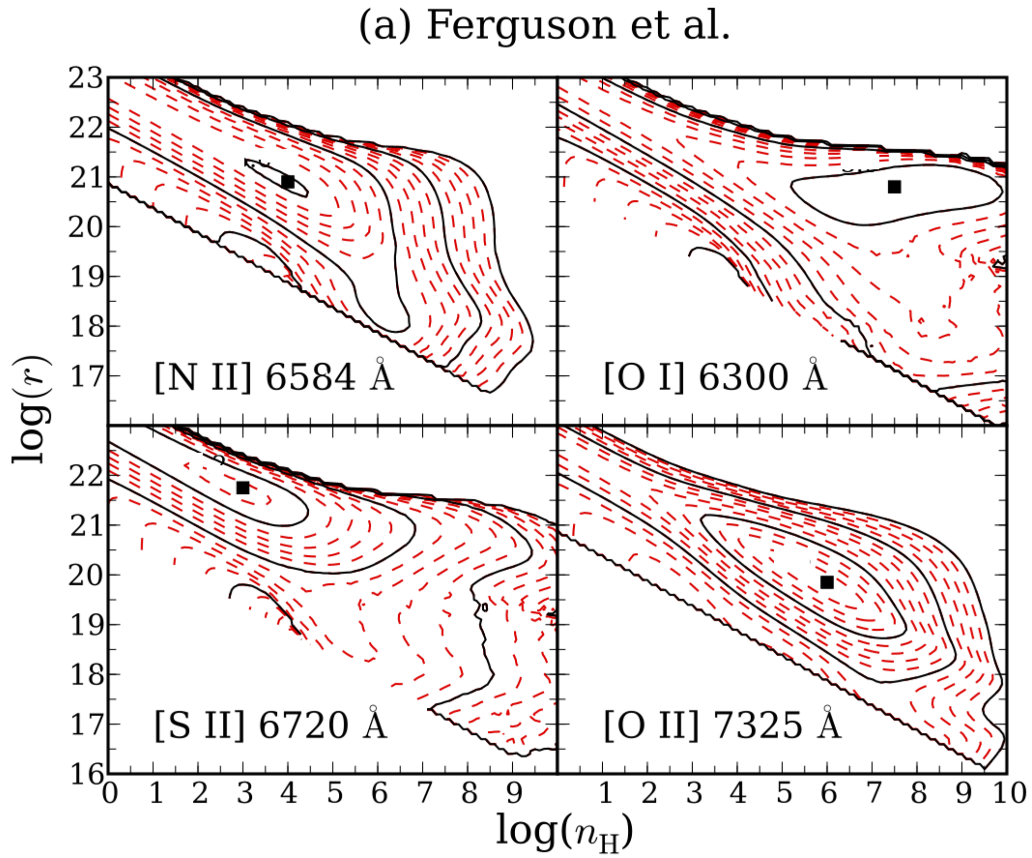
(a) Ferguson et al.

Figure 3.5 Contours for log equivalent widths as a function of radius, r, and hydrogen density, n_{H}. All equivalent widths are relative to the continuum at 4860 Å. The contour increments represent steps of 0.2 dex with a lower cutoff at 1 Å. The squares are labeled with log equivalent width and indicate the local maxima for each grid. We show equivalent width diagrams for three different SEDs: (a) Ferguson et al. (1997), (b) Mathews and Ferland (1987), (c) our optimized SED. Panel (b) clearly shows a second region in which the gas is optimally reprocessed into emission lines. This can be seen to a lesser degree in panels (a) and (c) where a "shelf" starts to form in high density, high flux regions.

Figure 3.5 (cont'd)

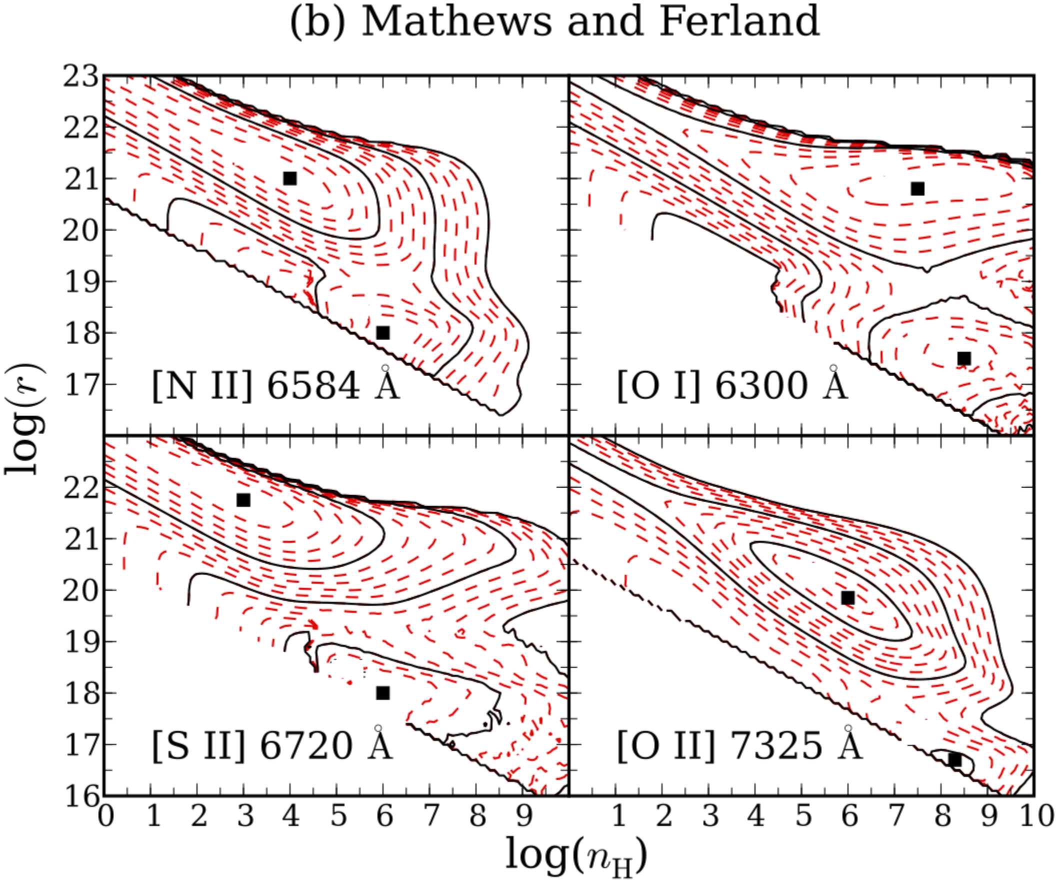

Figure 3.5 (cont'd)

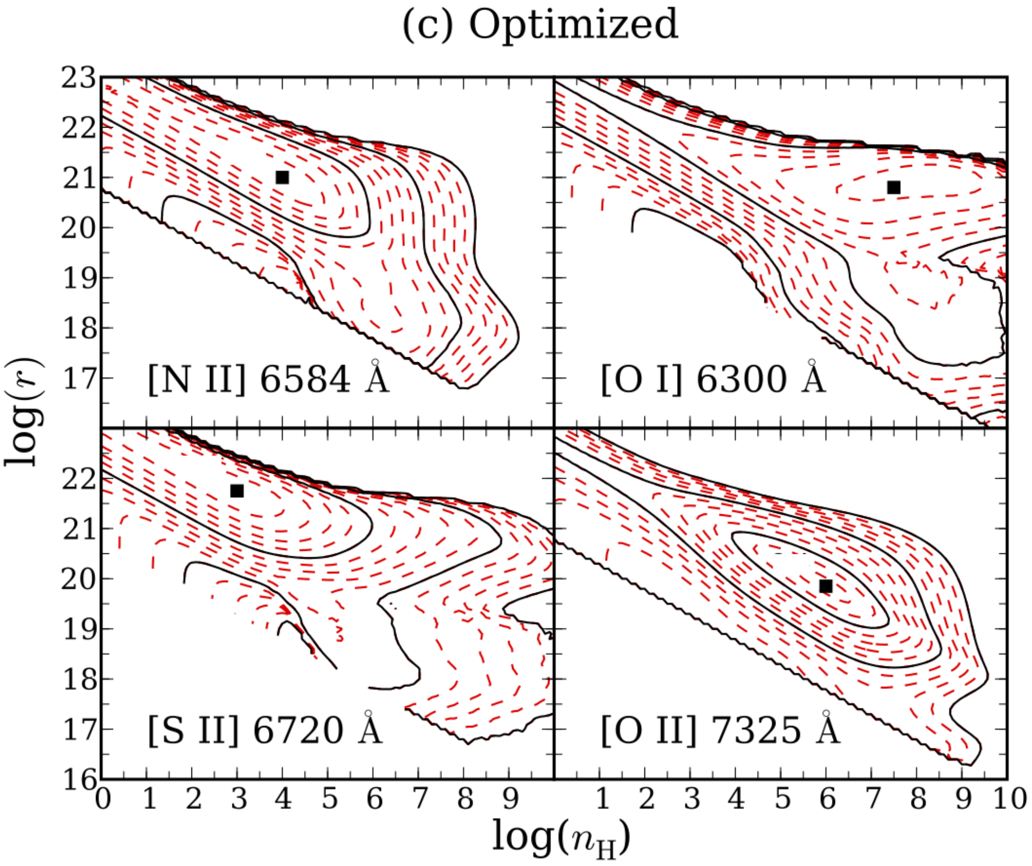

(c) Optimized

allow clouds to have thickness greater than 10 per cent of their distance to the source, they note that this criterion did not have a real impact on the resulting contours.

3.3.4 Metallicity Effects

We found that [N II] λ6584 was underpredicted with our solar abundance set, so we adjusted the nitrogen abundance. Nitrogen abundances have long been known to deviate from solar abundances in AGN (e.g. Storchi-Bergmann & Pastoriza 1990; Dopita & Sutherland 1995; Hamann & Ferland 1999). Baldwin et al. (2003) found that nitrogen abundances a factor of 15 above solar are needed to accurately represent the QSO Q0353-383, and Bradley, Kaiser & Baan (2004) found a factor of 34 enhancement in the weak NLR in M51. Nitrogen enhancement in AGN is thought to stem from secondary CNO nucleosynthesis, where carbon and oxygen are pre-existing, and then distributed by stellar winds from massive stars. This creates a unique scaling relationship with metallicity, [N/H] $\propto Z^2$ while other elements scale linearly with metallicity (Hamann & Ferland 1999).

We used that scaling relation to tune the abundances to fit [N II] λ6584/ [O II] λ3727, a metallicity indicator (Groves, Heckman & Kauffmann 2006) and [N II] λ6584/Hα. After iterating over a range of metallicities[2], we found that a metallicity of 1.4 $Z_\odot$ provides the best agreement with these two line ratios. Enhancing only nitrogen by a factor of 1.5 above solar would give an equally good fit to the observations, but we used the 1.4 $Z_\odot$ value appropriate for secondary enrichment.

Our final abundance set for the dust-free models, by number relative to hydrogen, is given in the log as follows: He: -0.987; Li: -8.54; Be: -10.4; B: -8.97; C: -3.46; N: -3.90; O: -3.16; F: -7.37; Ne: -3.77; Na: -5.53; Mg: -4.27; Al: -5.36; Si: -4.34; P: -6.28; S: -4.65; Cl: -6.57; Ar: -5.45; K: -6.72; Ca: -5.50; Sc: -8.65; Ti: -6.81; V: -7.83; Cr: -6.16; Mn: -6.32; Fe: -4.39; Co: -6.93; Ni: -5.60; Cu: -7.58; Zn: -7.19.

3.3.5 Final Dust-Free Model

Our goal in this paper is find a single tunable LOC parameter responsible for the variation in AGN ranging from Seyferts all the way down to the lowest-ionization objects as evident in Figure 3.1. The best case for achieving that goal is to use our final dust-free models for the individual clouds.

In order to get a fuller picture of the physical conditions in the individual clouds as a function of their position on the $\log(n_{\rm H})\log(r)$ plane, Figure 3.6 shows the ionization parameter, U (dotted lines), and the gas temperature in the [O III]-emitting zone T_e (dashed and solid lines) at the illuminated face of the cloud. The cutoff for detectable

---

[2] Here we adopted the common usage of the term metallicity as the metals abundance relative to hydrogen, by number, normalized to solar values. However, we note that metallicity is more properly defined as a mass fraction.

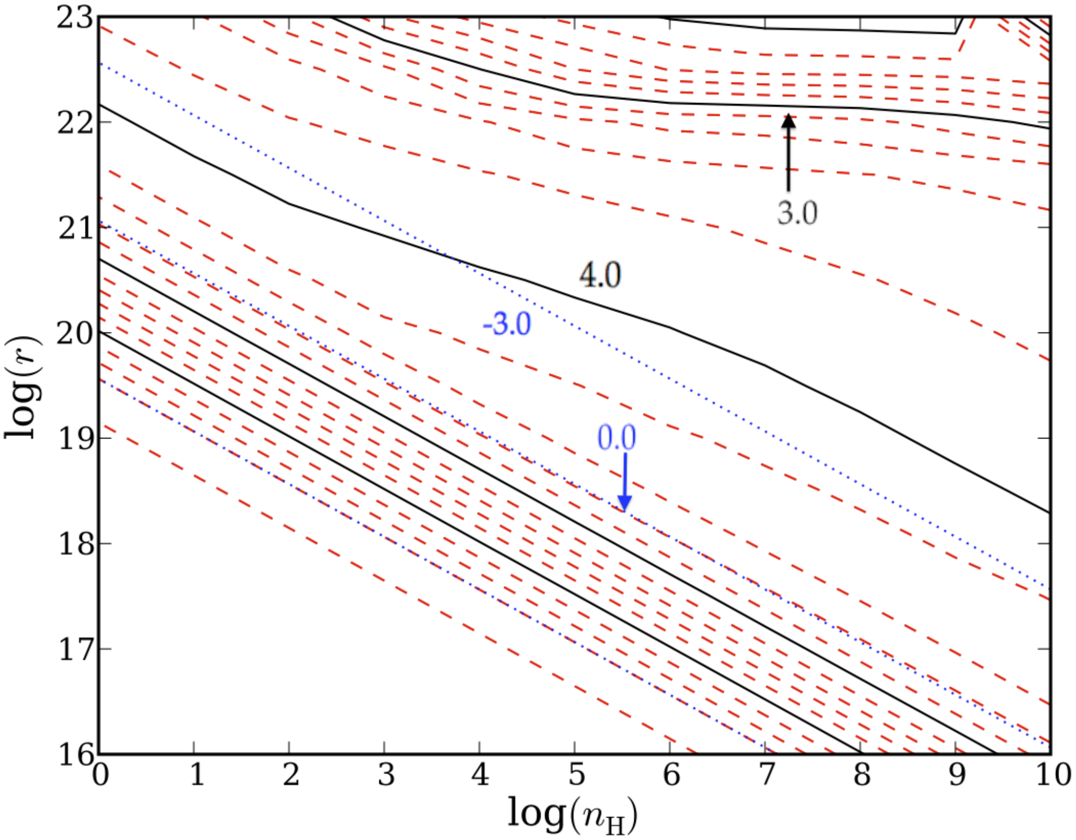

Figure 3.6 The ionization parameter and temperature at the illuminated face of each cloud. The ionization parameter is shown by a representative sample of evenly spaced blue, dotted contours across the LOC plane. The temperature is given in 1.0 dex (black lines) and 0.2 dex (red lines) increments.

lines is taken to be EW = 1 Å, which roughly corresponds to $\log(U) = 3.0$. Each U contour has a slope of $(n_H dr)/(r dn_H) = -0.5$. Figure 3.7 displays the equivalent width contours for 20 important emission lines, as a function of $\log(n_H)$ and $\log(r)$.

Next, Figs. 3.8-3.12 show 24 different diagnostic diagrams predicted for the LOC integrations using the dust-free model, and compare them to the observations in the same way as was done in Figure 3.4. The lines and symbols in Figs. 3.8-3.12 are keyed the same as in Figure 3.4, with black lines and symbols showing the observed line ratios, and the colored lines and symbols showing predicted line ratios, with a separate predicted line for each sequence of LOC models in which β is held constant but γ is varied. Each panel is on the same scale to emphasize at a glance which line ratios are better indicators. The error bars in the bottom right corner of the last panel in each figure represent a factor of two error.

We discuss the individual diagrams from Figure 3.8-3.12 below, but a first glance over the full set of diagrams shows that our LOC models can fit almost all line ratios for the upper half of the observed AGN locus (the black points starting from the larger black symbols and working back down the observed sequence). The larger black square represents the observed extreme AGN case, a41. The LOC model which provides the overall best fit to those observations has $\beta = -1.4$, $\gamma = -0.75$ and is in--dicated by the larger open (filled in white) green circle. The observed a41-a01 sequence is matched using a density weighting of $\beta = -1.4$ (the green line on Figure 3.8-3.12) while changing the radial weighting as parameterized by γ in Equation 3.1. The a41-a31-a21-a11-a01 observations are fitted to reasonable accuracy in most panels on Fig. 3.8-3.12 by the LOC models with values $\gamma = -0.75$, $\gamma = -0.5$, $\gamma = -0.25$, $\gamma = 0.0$, $\gamma = 1.0$ respectively, each of which is shown as an open circle. A perfect fit would have the larger black square fall exactly on top of the larger open circle, and then to have each successive black square fall on top of each successive open circle.

At high - moderate ionization, the fits are usually within a factor of two, which demonstrates the effectiveness of the MFICA method at picking out an AGN ionization sequence that is largely described by the variation of a single physically meaningful parameter the radial distribution of clouds. Table 3.3a shows the line ratio predictions for our model at each of these locations as well as comparison to the observed value. Next, we discuss the details of these comparisons between the models and the observations.

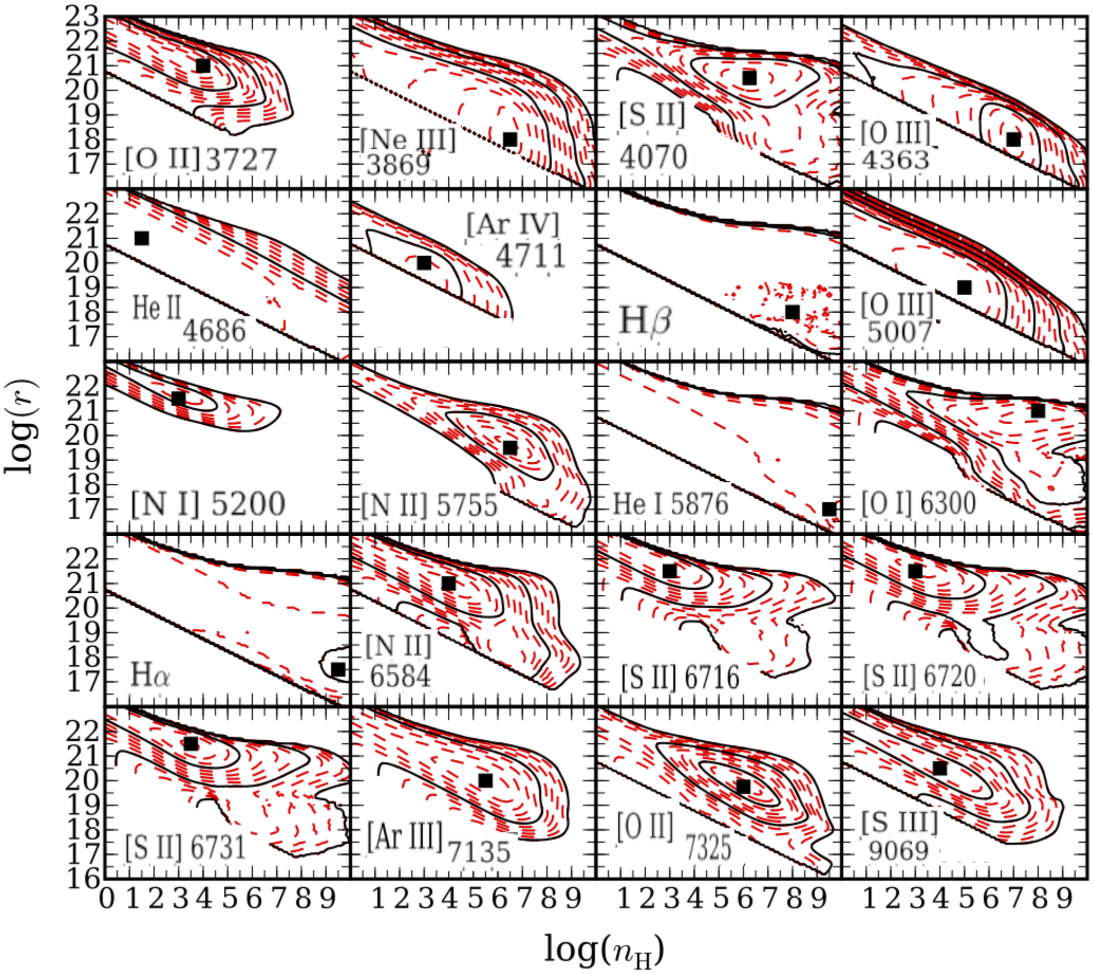

Figure 3.7 Contours of log equivalent width as a function of radius, r, and hydrogen density, n_{H}, in the same manner as Figure 3.5 but for our best fitting model.

Excitation Mechanism

Panels (a)-(d) of Figure 3.8 show classic diagnostic diagrams from BPT and VO87, which are particularly sensitive to whether the excitation source is a power law (AGN) or starburst. The degree to which our model fits the AGN observations emphasizes its consistency with line ratios widely used to identify the excitation source and

Table 3.3a: AGN Emission line ratio predictions - Dust Free Model

	Model Predictions (log of line ratio)					Log(Predicted / Observed)				
Line Ratio	a01	a11	a21	a31	a41	a01	a11	a21	a31	a41
[O II] 3727 / [O III] 5007	0.45	-0.05	-0.22	-0.41	-0.63	-0.55	-0.23	-0.14	-0.17	-0.18
[O II] 3727 / [O I] 6300	0.70	0.73	0.74	0.75	0.74	-0.80	-0.46	-0.29	-0.31	-0.20
[O II] 3727 / [O II] 7325	2.10	1.90	1.81	1.69	1.53	0.10	0.36	0.41	0.27	0.13
[Ne III] 3869 / He II 4686	0.24	0.37	0.43	0.50	0.57	<-0.20	-0.47	-0.38	-0.19	-0.04
[S II] 4070 / [S II] 6720	-1.38	-1.27	-1.21	-1.13	-1.02	-0.53	-0.002	-0.42	-0.16	0.02
[O III] 4363 / [O III] 5007	-2.52	-2.38	-2.34	-2.29	-2.22	>-1.74	-0.87	-0.78	-0.74	-0.41
He II 4686 / Hβ	-0.90	-0.84	-0.81	-0.77	-0.74	>0.92	0.55	0.20	0.03	-0.11
He II 4686 / He I 5876	-0.18	-0.10	-0.05	-0.002	0.06	>0.28	0.10	-0.14	-0.21	-0.30
[Ar IV] 4711 / [Ar III] 7135	-2.15	-1.41	-1.20	-0.98	-0.76	>-2.00	-1.11	-0.59	-0.49	-0.25
[O III] 5007 / Hβ	-0.24	0.28	0.43	0.60	0.75	0.20	0.10	-0.05	-0.06	-0.17
[O III] 5007 / [Ar III] 7135	0.69	1.16	1.30	1.46	1.64	-0.33	-0.32	-0.27	-0.12	0.00
[N I] 5200 / Hα	-1.68	-1.75	-1.80	-1.87	-2.00	0.04	-0.12	-0.19	-0.24	-0.33
[N I] 5200 / [N II] 6584	-1.43	-1.48	-1.51	-1.54	-1.59	0.07	-0.01	-0.02	-0.01	-0.07
[N I] 5200 / [O II] 7325	0.69	0.40	0.27	0.10	-0.11	0.51	0.39	0.43	0.29	0.16
[N II] 5755 / [N II] 6584	-2.38	-2.28	-2.23	-2.16	-2.05	>-0.75	>-0.68	-0.50	-0.20	-0.02

Table 3.3a (cont'd)

	Model Predictions (log of line ratio)					Log(Predicted / Observed)				
He I 5876 / Hβ	-0.72	-0.74	-0.75	-0.77	-0.79	0.64	0.45	0.33	0.25	0.19
[O I] 6300 / [O III] 5007	-0.25	-0.79	-0.96	-1.16	-1.37	0.25	0.23	0.16	0.14	0.02
[O I] 6300 / Hα	-0.97	-0.99	-1.00	-1.03	-1.09	0.42	0.31	0.08	0.06	-0.16
[O I] 6300 / [N II] 6584	-0.72	-0.72	-0.71	-0.70	-0.68	0.45	0.42	0.26	0.29	0.10
Hα / Hβ	0.48	0.48	0.48	0.48	0.47	0.03	0.02	0.02	0.02	0.02
[N II] 6584 / [O II] 3727	0.02	-0.01	-0.03	-0.04	-0.06	0.35	0.03	0.04	0.02	0.01
[N II] 6584 / Hα	-0.25	-0.27	-0.29	-0.33	-0.41	-0.03	-0.12	-0.18	-0.23	-0.26
[S II] 6716 / [S II] 6731	0.08	0.06	0.05	0.04	0.03	-0.01	0.00	0.00	-0.01	-0.05
[S II] 6720 / Hα	-0.09	-0.15	-0.19	-0.25	-0.36	0.42	0.33	0.23	0.11	-0.05
[O II] 7325 / [O I] 6300	-1.40	-1.17	-1.07	-0.94	-0.79	-0.89	-0.82	-0.71	-0.58	-0.33
[O II] 7325 / Hα	-2.37	-2.16	-2.07	-1.98	-1.88	-0.47	-0.51	-0.62	-0.52	-0.49
Fraction of Ratios Fitted	-	-	-	-	-	0.50	0.46	0.62	0.81	0.85
	Free Parameters					Free Parameters				
Density Weighting - β	-1.4	-1.4	-1.4	-1.4	-1.4	-1.4	-1.4	-1.4	-1.4	-1.4
Radial Weighting - γ	1.0	0.0	-0.25	-0.5	-0.75	1.0	0.0	-0.25	-0.5	-0.75

Table 3.3b: AGN Emission line ratio predictions - Dusty Model

	Model Predictions (log of line ratio)					Log(Predicted / Observed)				
Line Ratio	a01	a11	a21	a31	a41	a01	a11	a21	a31	a41
[O II] 3727 / [O III] 5007	0.79	-0.08	-0.26	-0.45	-0.65	-0.21	-0.26	-0.18	-0.22	-0.20
[O II] 3727 / [O I] 6300	0.77	0.78	0.76	0.72	0.64	-0.49	-0.41	-0.27	-0.34	-0.30
[O II] 3727 / [O II] 7325	1.94	1.76	1.68	1.57	1.41	-0.06	0.23	0.28	0.15	-0.002
[Ne III] 3869 / He II 4686	0.63	0.57	0.54	0.51	0.48	<0.18	-0.27	-0.27	-0.18	-0.14
[S II] 4070 / [S II] 6720	-1.24	-1.18	-1.15	-1.12	-1.06	-0.38	0.09	-0.36	-0.15	0.02
[O III] 4363 / [O III] 5007	-2.32	-1.73	-1.60	-1.46	-1.31	>-1.54	-0.22	-0.05	0.08	0.50
He II 4686 / Hβ	-1.37	-1.07	-0.98	-0.87	-0.77	>0.45	0.32	0.03	-0.07	-0.14
He II 4686 / He I 5876	-0.53	-0.21	-0.12	0.01	0.11	>-0.07	0.02	-0.20	-0.22	-0.25
[Ar IV] 4711 / [Ar III] 7135	-2.35	-1.25	-1.09	-0.95	-0.84	>-2.11	-0.95	-0.49	-0.47	-0.33
[O III] 5007 / Hβ	-0.18	0.57	0.69	0.81	0.90	0.26	0.39	0.21	0.15	-0.02
[O III] 5007 / [Ar III] 7135	0.47	1.19	1.32	1.43	1.55	-0.54	-0.28	-0.26	-0.14	-0.10
[N I] 5200 / Hα	-1.13	-1.30	-1.36	-1.43	-1.51	0.59	0.33	0.24	0.21	0.15
[N I] 5200 / [N II] 6584	-1.21	-1.24	-1.24	-1.23	-1.22	0.29	0.24	0.25	0.31	0.30
[N I] 5200 / [O II] 7325	0.68	0.46	0.38	0.28	0.15	0.50	0.45	0.54	0.47	0.43
[N II] 5755 / [N II] 6584	-2.11	-1.97	-1.89	-1.75	-1.55	>-0.49	>-0.37	-0.16	0.21	0.49

Table 3.3b (cont'd)

	Model Predictions (log of line ratio)					Log(Predicted / Observed)				
He I 5876 / Hβ	-0.84	-0.85	-0.86	-0.87	-0.88	0.52	0.34	0.23	0.15	0.10
[O I] 6300 / [O III] 5007	0.02	-0.86	-1.03	-1.17	-1.30	0.52	0.15	0.09	0.12	0.10
[O I] 6300 / Hα	-0.64	-0.78	-0.83	-0.87	-0.90	0.75	0.51	0.26	0.22	0.03
[O I] 6300 / [N II] 6584	-0.73	-0.72	-0.70	-0.67	-0.62	0.45	0.42	0.27	0.32	0.17
Hα / Hβ	0.48	0.49	0.49	0.50	0.51	0.02	0.03	0.04	0.04	0.05
[N II] 6584 / [O II] 3727	0.05	-0.06	-0.06	-0.05	-0.03	0.27	-0.02	0.003	0.01	0.13
[N II] 6584 / Hα	0.08	-0.06	-0.12	-0.20	-0.29	0.30	0.09	-0.01	-0.10	-0.14
[S II] 6716 / [S II] 6731	0.09	0.08	0.07	0.06	0.06	0.01	0.02	0.02	0.02	-0.02
[S II] 6720 / Hα	0.01	-0.20	-0.28	-0.38	-0.49	0.52	0.28	0.14	$<$0.001	-0.18
[O II] 7325 / [O I] 6300	-1.17	-0.98	-0.92	-0.85	-0.76	-0.66	-0.63	-0.56	-0.48	-0.30
[O II] 7325 / Hα	-1.81	-1.77	-1.74	-1.71	-1.67	0.09	-0.12	-0.30	-0.26	-0.27
Fraction of Ratios Fitted	-	-	-	-	-	0.54	0.62	0.85	0.77	0.85
	Free Parameters					Free Parameters				
Density Weighting - β	-1.8	-1.8	-1.8	-1.8	-1.8	-1.8	-1.8	-1.8	-1.8	-1.8
Radial Weighting - γ	0.5	-1.0	-1.25	-1.5	-1.75	0.5	-1.0	-1.25	-1.5	-1.75

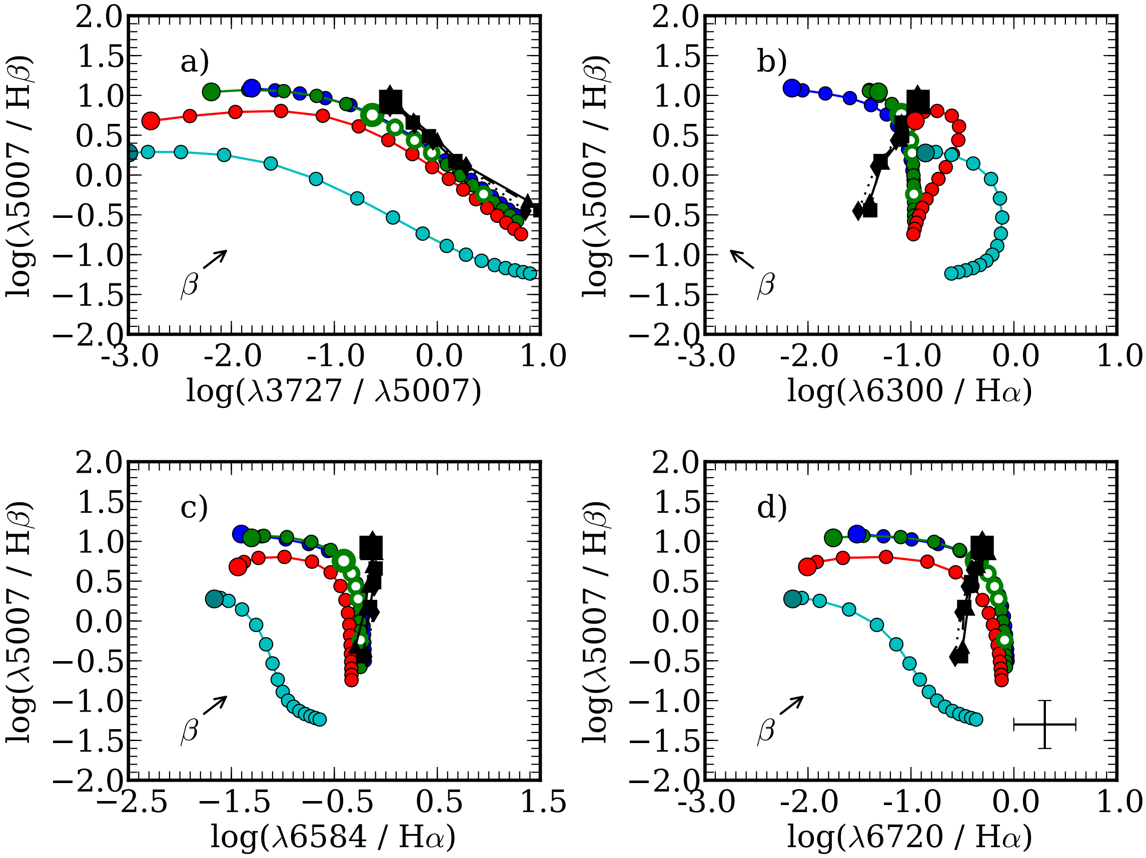

Figure 3.8 Line ratio diagrams constraining the excitation mechanism, displayed in the same manner as Figure 3.4. Our model successfully fits the high to moderation ionization AGN subsets. In the cases of [N II] λ6584/ Hα and [O III] λ5007/ Hβ we have successfully matched the entire AGN sequence to within a factor of two.

classification of emission line galaxies. Comparing simulations with power law spectra and starlight to observations resulted in the development of these diagrams.

We used these diagrams to make a baseline assessment of our model, since we must be able to reproduce typical emission line ratios before exploring other diagnostic diagrams. Using the criterion of a factor of two representing an adequate fit, we successfully matched [N II] λ6584/Hα over the entire AGN sequence, [O III] λ5007/Hβ, [O II] λ3727/ [O III] λ5007 and [O I] λ 6300/ Hα for the a41-a31-a21-a11 sequence (higher to low ionization subsets), and [S II] λ6720/Hα for the a41-a31-a21

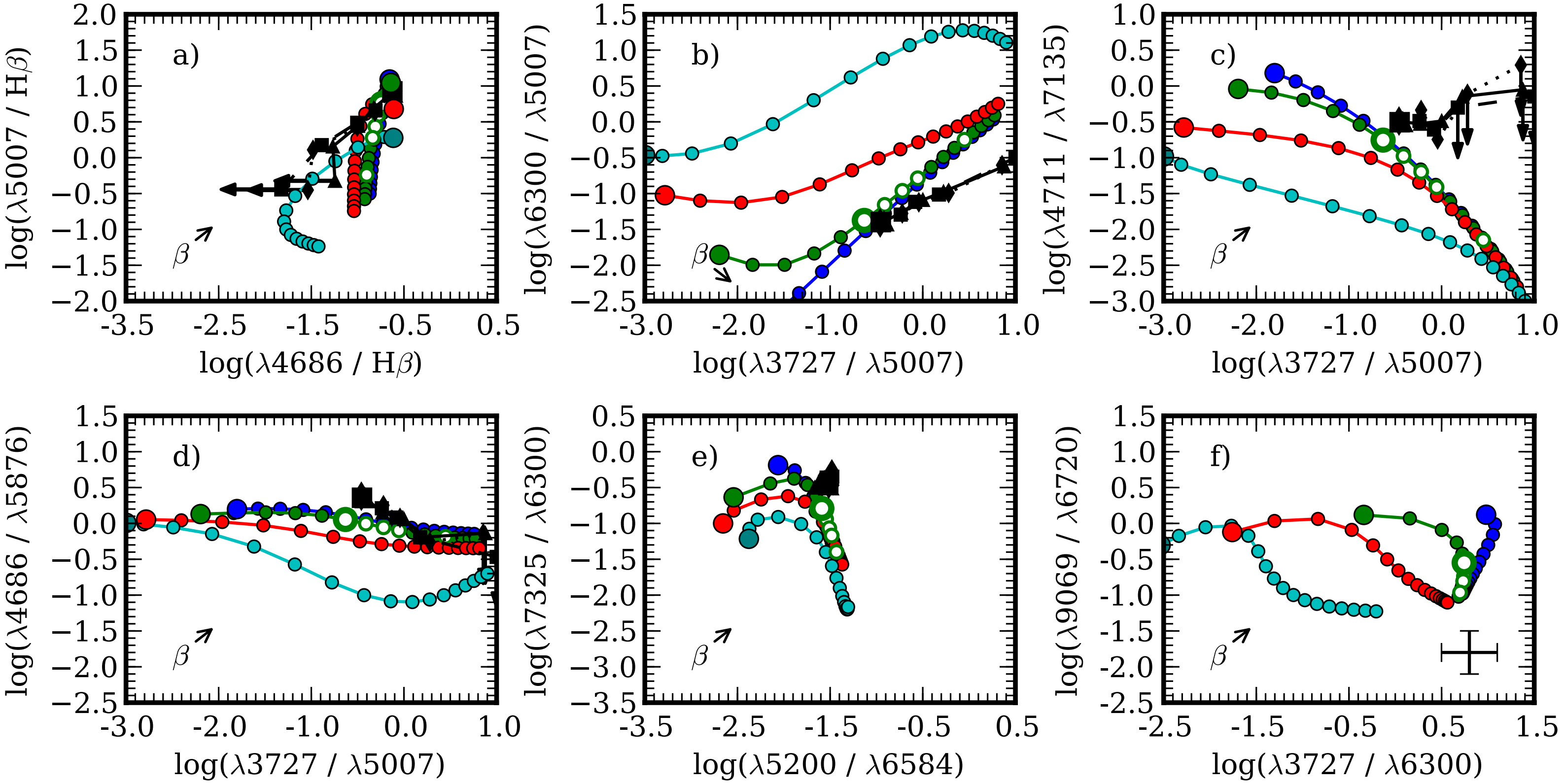

Figure 3.9 Line ratio diagrams that constrain the SED, displayed in the same manner as Figure 3.4. The extreme AGN subsets (large symbols) are successfully fitted in essentially every diagram. Our model reproduces the high to moderate ionization observations for all but [Ar IV] λ4711 / [Ar III] λ7135 and the entire sequence for all but He II λ4686/ Hβ and [O II] λ7325 / [O I] λ6300.

sequence (higher to moderate ionization subsets). These results show that we have sufficient agreement with established excitation diagnostics to proceed on to other line ratio diagrams.

Spectral Energy Distribution

In Panels (a)-(f) of Figure 3.9 we show less common line ratio diagrams, which draw upon weaker lines to constrain the SED. This adds important cross-checks to the results from the usual strong-line diagrams in previous investigations. In order to limit the effects of differing abundances, these diagrams mostly use ratios of lines from different ionization states of the same element. The S/N obtained from co-adding spectra instead of using emission lines from individual AGN makes these diagrams more trustworthy indicators. Panel (e) combines two SED indicators, [N I] λ5200/ [N II] λ6584 and [O II] λ7325 / [O I] λ6300, both of which are minimally affected by reddening. The results show that although the observations do not show the predicted modest changes of these line ratios as the radial weighting is changed in the LOC model, the entire [N I] λ5200/ [N II] λ6584 sequence and higher ionization observation of [O II] λ7325 / [O I] λ6300 still does agree with a change in radial weighting to within approximately a factor of two.

Panel (f) on Figure 3.9 combines two SED indicating ratios, [S III] λ9069/ [S II] λ6720 vs. [O II] λ3727/ [O I] λ6300. The observations used here do not extend out to the [S III] lines, but these lines are commonly measured in low-z galaxies and we include them here so that other investigations can take of advantage of these results. The ratio [O II] λ3727/ [O I] λ6300 is included in our observations, and ranges from 1.0 (in the log) at the high ionization end to 1.5 for the lowest ionization cases. The adopted LOC models all predict that this ratio should be about 0.7 in the log, which agrees with the observations to within a factor of two except for the lower ionization cases.

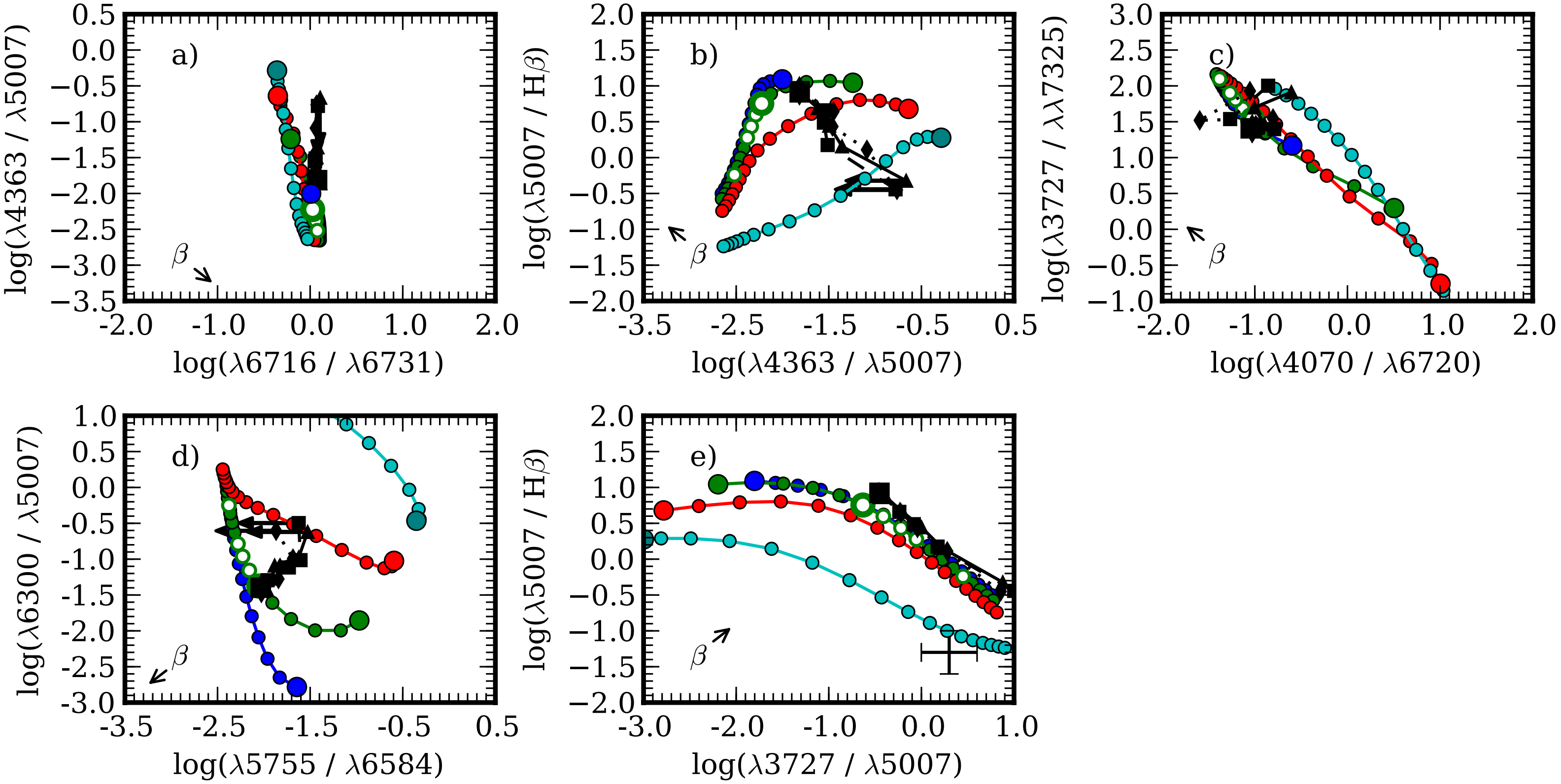

Figure 3.10 Line ratio diagrams that constrain the physical conditions, displayed in the same manner as Figure 3.4. The excellent agreement between our model and the [S II] λ6716 / [S II] λ6731 ratio over the entire range of ionization shows that low density regions are correctly predicted by our model. High density regions, probed by the [S II] λ4070 / [S II] λ6720 ratio, also agree with the high to moderate ionization observations. The [O II] λ3727 / [O III] λ5007 ratio, sensitive to ionization parameter, fits the observations at all but the lowest ionization points. The temperature, however, given by the [O III] λ4363 / [O III] λ5008 ratio and [N II] λ5755 / [N II] λ6584 ratio contradicts observations in all but the highest ionization cases.

Physical Conditions

Figure 3.10 probes the average temperature and density. Except as noted, these figures use standard temperature- and density-sensitive intensity ratios (see AGN3, chapter 5). In the case of the temperature sensitive [O III] λ4363/ [O III] λ5007 ratio (Panels (a)-(b)), the models come close to matching the higher ionization subsamples but the lower ionization subsamples give higher temperatures than those given by our models. Panel (d) confirms this finding using another temperature indicator, [N II] λ5755/ λ6584. The observations agree with our models at the higher ionization end of the sequence but at lower ionization the ratio disagrees with our models by indicating higher temperatures than predicted. This is an important discrepancy that we will explore further in §4.2.

Panel (a) shows a typical density sensitive ratio, [S II] λ6716/ λ6731, which is in excellent agreement with our models. This ratio is very insensitive to our free parameters, which is not surprising in these LOC models because the density indicated by the [S II] line ratio is close to the density for optimal emission of these lines. Panel (c) combines a low density indicator, [O II] λ3727/ λ7325, with a high density indicator, [S II] λ4070/ λ6720 (Holt et al. 2011). Our model agrees with the higher and lower ionization subsamples, but fails to match the moderate ionization AGN subsamples. Panel (e) shows a diagram originally proposed by BPT, and therefore also appears in Figure 3.8, but which is a good indicator of the ionization parameter (Komossa & Schulz 1997; G04b). The observed [O II] λ3727/ [O III] λ5007 agrees nicely with all but the lower end of the sequence and even in this region only disagrees by a factor of 3-4.

Grains

The diagnostics in Figure 3.11 are taken from G04b, who found these line ratios to be sensitive to the radiation pressure from dust grains and to emphasize the success

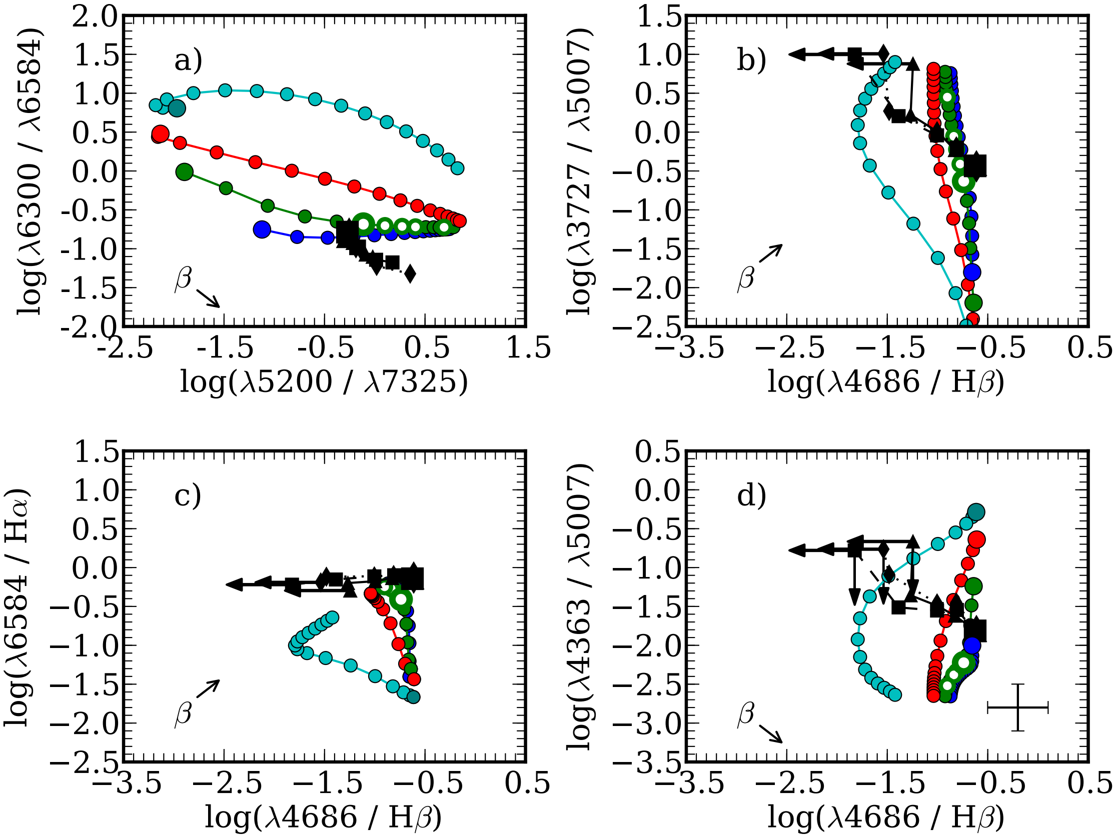

Figure 3.11 Line ratio diagrams sensitive to radiation pressure from grains taken from G04b, displayed in the same manner as Figure 3.4. These dust-free models successfully fit all of the high to moderate ionization observations except for [O III] λ4363 / [O III] λ 5007, which also failed in G04b.

of their dusty model. However, we find that our dust-free models match the observations just as well as the G04b dusty models. For example, Panel (a) shows [N I] λ5200 and [O II] λ7325, which are typically weak in Seyfert galaxies, and there is decent agreement between the AGN observations and our dust free model. G04b found dramatic differences between the observations and dust-free models on this diagram. G04a argued that the diagram in Panel (b) ([O II] λ3727/ [O III] λ5007 vs. He II λ4686/Hβ) points out the success of their dusty models over their dust-free models at high ionization parameters. In contrast, our dust-free models fit quite nicely over

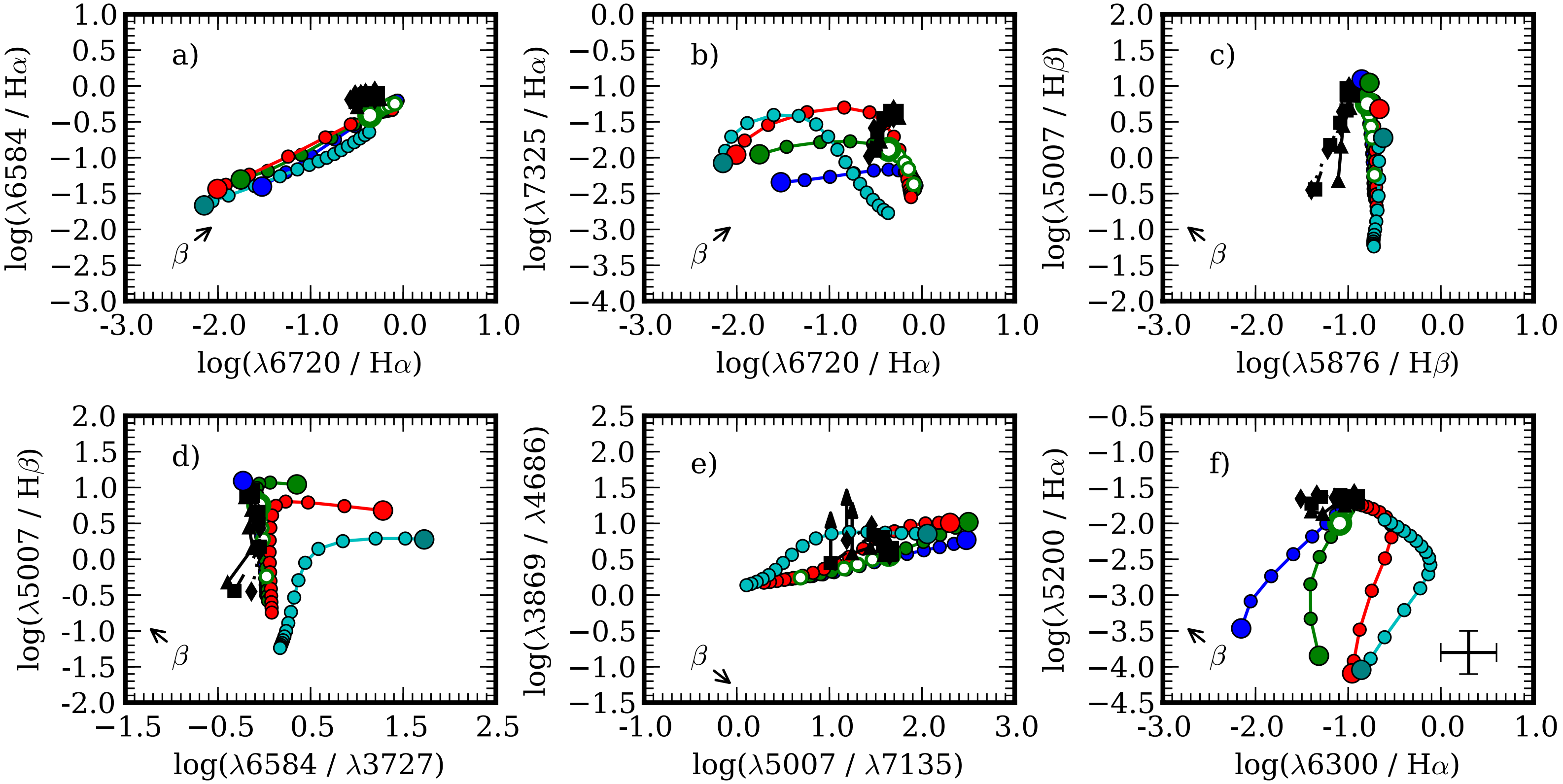

Figure 3.12 Line ratio diagrams that constrain abundances, displayed in the same manner as Figure 3.4. The best abundance sensitive ratio, [N II] λ6584 / [O II] λ3727, was used to optimize our abundance set and fits observations over the entire range of ionization except for the lowest subsample. The models and observations agree to within the factor two error bars except for the [O II] λ7325/ Hα ratio, which agrees with the highest ionization observation to within a factor of three.

a large range of ionization. The integrations in Panel (c) match our high to moderate ionization region of the sequence. Panel (d) was used by G04b to emphasize that their dusty model is not devoid of problems because of the inability to reproduce high temperatures at moderate ionization; our model shows that this problem is also present in our dust-free models. It should be noted that the classical Seyferts to which G04b compared their models almost all lie above the dotted and solid lines in Figure 3.1a, so that in terms of the BPT and VO87 diagrams their results should be compared only to our 3 highest-ionization levels. These are the cases for which our dust-free models give the best fits to the observations.

Abundances

Figure 3.12 shows ratios of lines from ions with similar ionization potentials, but from different elements, leading to abundance sensitivity. Panel (a) stems from a discussion in Storchi-Bergmann & Pastoriza (1990) where only nitrogen and sulfur abundances needed enhancements to account for emission in different AGN covering a wide range in ionization. However, our 1.4 $Z_\odot$ solar abundance set nicely fits this diagram for the high - moderate ionization subsamples. Panel (b) incorporates [O II] λ7325/Hα, a ratio involving a weak line only measurable because of our large sample, which fits our highest ionization subsamples within a factor of 3. He I λ5876 depends linearly on the helium abundance; therefore Panel (c) shows that our default solar helium abundance is correct for all but the lower ionization parts of the sequence.

Panel (d) displays the main determinant in our metallicity optimization, [N II] λ6584/ [O II] λ3727, and our model fits the entire sequence to within 10 per cent except for the lowest ionization observation. The diagram in Panel (e), [Ne III] λ3869/ He II λ4686 vs. [O III] λ5007/ [Ar III] λ7135 uses lines with fairly high ionization potentials, and shows agreement between the models and observations over almost the entire length of the AGN locus. The diagram in Panel (f), [O I] λ6300/Hα vs.

[N I] λ5200/Hα uses lines with lower ionization potentials. In this case the predicted ratios for our adopted sequence of models all cluster at one point on this diagram, and the observed ratios fall at that same location except for the case of [O I] λ6300/Hα for the very lowest ionization subset.

3.3.6 Dusty Models

As described in §3.1, in addition to the dust-free models we also ran grids of dusty models, to test whether or not a dusty NLR could do an equally good job of reproducing the observations along the entire length of the AGN locus, again by tuning only a single free parameter. A dusty NLR model was also explored by F97 and preferred by G04a, making it natural to see if such a model is a viable alternative to a dust-free interpretation.

The abundances we adopted for modeling a dusty NLR are given in §3.1; they allow for depletion of refractory elements into grains at large radial distances from the central engine. As with our dust-free models, the He II λ4686/Hβ ratio was overpredicted using the F97 SED. We optimized the SED using the same process as discussed in §3.2 and arrived at an incident continuum characterized by $T_{\rm cut} \sim 1.5 \times 10^5$ K, $\alpha_{\rm UV} = -0.5$, $\alpha_{ox} = -1.4$, $\alpha_x = -1.0$, and $kT_{\rm IR} = 0.14$ eV (Figure 3.3).

Depending on the radius, our baseline abundance set changes due to the formation of grains, therefore there are actually slightly different metallicities within a single dusty grid. As with the dust-free models, there was the need for an increase in metallicity or selective nitrogen enhancement. We scaled the abundances using the empirically determined scaling relationships given in §3.4 and found that a metallicity of 1.4 $Z_\odot$ in the dust-free portion of the grid gave a satisfactory fit.

Table 3.3b provides the emission-line ratio predictions and their comparison to our subsets for our best dusty model. Our dusty model fits a few line ratios slightly better in the moderate ionization part of the sequence. In particular, the entire [O

II] λ7325/Hα sequence and the moderate ionization [O III] λ4363 / [O III] λ5007 subsets are fit within a factor of two.

However, our dust-free model fits all but the moderate ionization subsets of [O II] λ7325/Hα to within a factor of three. Furthermore, our dusty models still have the same problem as the dust-free models in that they predict that the [O III] λ4363 / [O III] λ5007 line ratio should get larger as the ionization level increases, while the opposite is observed to happen. The dusty models predict a systematically higher [O III] λ4363 / [O III] λ5007 emission line ratio than do the dust-free models, as a result of the gas being hotter due to photoelectric heating by dust (see Baldwin et al 1991), so the subsets are matched at a lower observed ionization level. Our dusty model similarly fails to reproduce the observed [N II] temperature at high ionization.

Our dusty models do not reproduce the lower ionization portion of some of the VO87 diagrams as well as our dust-free models and fail to account for the high ionization observations in a few ratios. Figure 3.13 shows some line ratios, which are not fit as well in the dusty case as in our dust-free model. Fig. 3.13a should be compared to Figure 3.8b and Figure 3.13b to Figure 3.11a. The dusty case is not ru--led out by these results, but the dust-free models give a marginally better fit at higher ionization.

3.4 Discussion

3.4.1 Physical Meaning of the AGN Locus

Analysis of the AGN region of the BPT diagram has historically been limited to well-identified emission-line galaxies displaying strong AGN properties. F97 studied these galaxies using LOC models, and Komassa & Schulz (1997) also studied luminous, high ionization Seyfert 2 galaxies using similar composite models having clouds spread over wide ranges in radial distance and density. In this paper, we have for the first

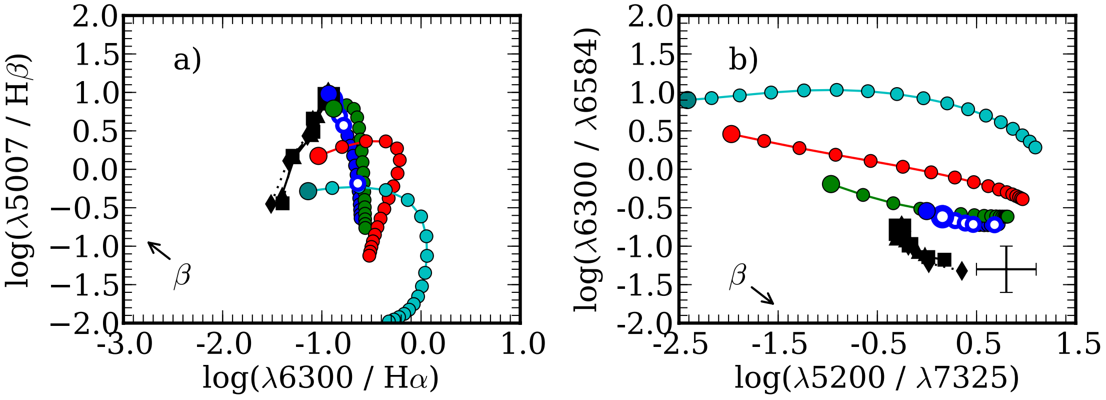

Figure 3.13 Line ratio diagrams for our dusty NLR models, displayed in the same manner as Figure 3.4. The AGN observations of some key line ratios, which are matched by our dust-free models, are not fit as well by the dusty models shown here. The hollow marker indicates our best set of free parameters in the dusty case.

time broadened this LOC-type analysis to include low ionization AGN, where the spectra become very similar to those of SF galaxies. Diagnostic diagrams that include weak lines can then provide valuable consistency checks for highly ionized AGN when developing physically meaningful interpretations of the AGN locus.

An ideal interpretation would be to find a single, tunable physical parameter which recreates the variation from high to low ionization along the AGN locus (first index i designating the aij subsets), as well as a second physical parameter responsible for moving galaxies off at right angles to the AGN locus (second index j). As we discuss below, we have found that variations in the radial weighting in the LOC model can account for the differences in the high and intermediate ionization AGN.

We note that we used a rather coarse interval of radial and density weightings to match the AGN observations so that their impact on the LOC integrations would be readily apparent from looking at line ratio diagrams. A finer spacing would yield slightly better fitting to all of the observations along the length of the AGN locus, but should not change any of our conclusions.

Higher - Moderate Ionization AGN

Figures 3.8-3.12 show that the higher ionization AGN are matched to within a factor of 2 by $\beta = -1.4$ models with either $\gamma = -0.75$ or $\gamma = -0.5$. The only emission-line ratios completely contrary to this statement are [O III] λ4364 / [O III] λ5007 and [O II] λ7325/Hα but even these ratios are in agreement to within a factor of 3 or 4. The ratio [Ar IV] λ4711/ [Ar III] λ7135 agrees with highest ionization locus point and [O II] λ7325/ [O I] λ6300 is approximately within a factor 2 of the highest ionization subsample. Although they do not agree for sequentially lower ionization observations, they again are within a factor of 3 or 4. The moderate ionization AGN, which correspond to the middle point along the AGN locus, are best fit by $\gamma = -0.5$ and $\beta = -1.4$. Indeed, every strong-line ratio in our sample agrees with this set of free parameters except for He I λ5876/Hβ. In addition to fitting ratios with strong lines, we have also incorporated many weak lines as consistency checks, and these also fit the higher to moderate ionization spectra. These results indicate that the progression along the AGN locus from high ionization to moderate ionization can be represented by a positive change in the radial weighting. Indeed, Figures 3.8-3.12 show this trend to be true for the majority of line-ratio diagrams presented. The change in radial weighting is in the sense that the galaxies with more luminous AGN (the ones higher up the AGN sequence) have more centrally concentrated NLRs.

However, there are still obvious discrepancies in [O III] λ4363/ [O III] λ5007, [N II] λ5755/λ6584 and [Ar IV] λ4711/ [Ar III] λ7135 for which we do not have an explanation. In particular, the [S II] λ6716/ [S II] λ6731 and [O III] λ4363/ [O III] λ5007 ratios indicate low density, high ionization gas defining the so called "temperature problem" in photoionization models (Komossa & Schulz 1997). As in F97, this problem has been solved for higher ionization AGN but there does not seem to be a relationship between a decrease in ionization and our free parameters. This is discussed in more detail below.

Low Ionization AGN

Several line ratios are successfully fitted over the entire length of the AGN sequence including the low-ionization cases. Specifically, [O III] λ5007/Hβ, [N II] λ6584/Hα, [O I] λ6300/ [O III] λ5007, [S II] λ6716/ [S II] λ6731, He II λ4686/ He I λ5876, [N I] λ5200/ [N II] λ6584, fit every observational point over the full range in ionization, and [O III] λ5007/ [Ar III] λ7135 and [N I] λ5200/Hα are very nearly within a factor of 2 for every subsample. However, there are still many line ratios that are not fit at low ionization. In addition to the [O III] λ4363/ [O III] λ5007, [N II] λ5755/λ6584 and [Ar IV] λ4711/ [Ar III] λ7135 ratios mentioned in the previous section, [O I] $\lambda6300/H\alpha$ also deviates from the trend that a more positive radial weighting corresponds to a lower ionization point on the locus.

We chose to vary the SED, metallicity, integration limits, density weighting and radial weighting, as these were the most likely parameters to provide a simple understanding of the AGN locus. Not counting the integration limits, we have used four free parameters to fit 24 different line ratios. The bottom rows in Tables 3.3a and 3.3b show the fraction of line ratios that are fitted to within a factor of two by our models. We fitted about 80 per cent of the observed ratios at the higher ionization end of the AGN sequence, but this drops to about 50 per cent (1113 ratios fitted) in the two lowest-ionization AGN subsets. The variation in the free parameters cannot completely account for the lowest ionization AGN, but varying other parameters could possibly produce an explanation still with the context of a photoionized, LOC-type model. The simulations in this paper ended when temperatures fell outside the range in which optical emission is strong. Other stopping conditions, such as cloud thickness, could be implemented to test their effects. We have also assumed a simple constant density model for our simulations. Constant density and constant pressure conditions have been implemented in other models (i.e. G04a, G04b) and using similar assumptions in our individual cloud models could produce better fits at the low ionization end of the AGN locus.

Another consideration is whether photoionization or shocks are the prevailing excitation mechanism for low ionization AGN. It is generally accepted that photoionization is responsible for exciting the NLR in luminous Seyfert galaxies. Early work suggested that shock heating was applicable in LINERS or radio galaxies (Dopita & Sutherland 1995, 1996) but this fails to reproduce the emission found in Seyferts and our lowest-ionization subsets. Shock models are not likely to explain the entire AGN locus.

Instead of non-stellar continua, a starburst could photoionize gas in the low ionization AGN. Alonso-Herrero et al. (2000) found that many LINERs can be explained by an aging starburst. While our low ionization subsets do not occupy the same region as LINERs in the VO87 diagrams, several starburst models in Alonso-Herrero et al. (2000) overlap with these subsets. Indeed, the low ionization AGN observations descend into a region of the BPT diagram that is also occupied by low ionization SF galaxies. We have assumed that adjusting a small number of parameters could account for the variation in both AGN and pure SF sequences; however, it is possible that there is considerable overlap in the physical properties in low ionization AGN and SF galaxies. A follow-up paper will address LOC models with multiple excitation mechanisms, to see if these fit the low-ionization end of the AGN sequence better than our current models. We also plan to address the SF locus in a future paper, which may also provide clues about the deeper nature of low ionization AGN.

Interpreting the Radial Distribution of Clouds

We studied the relationship between AGN spanning a wide range of ionization. We found that the differing properties of these AGN relate to the radial distribution of their NLR clouds, or more specifically, to the concentration of the clouds towards the central ionizing continuum source. Higher ionization AGN, such as Seyferts, have more centrally concentrated gas, while lower ionization "transition" AGN have their NLR spread out over more extended regions of the host galaxies. We are unable to comment on the nature of LINERs since our AGN subsets narrowly miss this region of the BPT diagram (Figure 3.1a), and clearly miss the region of LINERs identified by Kewley et al. (2006) on other diagrams including [S II]/Hα and [O I]/Hα. The above discussion is in terms of our results for dust-free models, but the dusty models lead to the same conclusions.

Table 3.1 shows that L([O III]) increases fairly strongly as the ionization level increases. However, this is just an ionization effect caused by the clouds being able on average to more efficiently produce [O III] emission. Kauffmann et al. (2003) found in their sample of SDSS AGN that L([O III]) is fairly constant as a function of distance from the star-forming locus, which they interpreted as support for the idea that in their sample the increase in ionization level at greater distances from the star-forming sequence represents a "mixing sequence" involving ionization both by starlight and by non-thermal AGN emission. Here we have found that L([O III]) does systematically depend on the position along the MFICS AGN sequence, which is roughly equivalent to the distance from the SF locus as measured by Kauffmann et al. (2003). We view this as an encouraging sign that we have cleaned up the Kauffmann et al. (2003) sample to produce one more dominated by just a single type of ionization and therefore better suited to studying the effects of additional variable parameters such as the size of the NLR.

A more fundamental result from Table 3.1 is that although the observed $L(\mathrm{H}\beta)$ is roughly constant along the entire length of the AGN sequence, the dereddened $L(\mathrm{H}\beta)$ values are higher for the lower-ionization objects and then decrease by a factor of about 5 between the low-ionization end of the AGN sequence and the high-ionization end. Since the NLR is in photoionization equilibrium, $L(\mathrm{H}\beta) \propto L_{\mathrm{ion}}$, assuming that the covering factor is the same for all AGN subsets. Therefore, we can infer from

$L(\mathrm{H}\beta)$ that the ionizing luminosity drops as the ionization level increases along the AGN locus. We could not measure the ionizing luminosity more directly, since even the high ionization subsets do not show any evidence of a non-thermal continuum, and X-ray measurements have not been made for the AGN in our subsets.

We deduce that the underlying physical trend is that the objects with more luminous central continuum sources have more extended NLRs. This suggests that the NLR might be a wind driven by radiation pressure. The decrease in ionization level in the more luminous objects is just an incidental result of their NLRs being more extended. The change in the radius weighting might represent a “clearing out” of the central regions as the AGN starts influencing the structure of the NLR. The usual scenario is that the AGN epoch begins after the ULIRG epoch and results in winds. The change in radius weighting from central to more distant might represent blowing out material from closer in, leaving distant material in place.

The Possible Role of Selection Effects

The above interpretation assumes that (1) the NLRs in all objects are photoionized by a central continuum source, and (2) the covering factors are the same from subset to subset. This interpretation does not explain the other strong trend in Table 1: the $E(B-V)$ values indicate that the low-ionization objects (the more extended NLRs) are more strongly reddened than are the high-ionization objects.

The luminosity correlation does not appear until the reddening correction has been applied. Could the luminosity correlation could be an artifact due to an incorrect reddening correction? We used $\mathrm{H}\alpha/\mathrm{H}\beta$ as our primary reddening indicator and assumed that the lines have their Case B intensities. Cloudy explicitly solves a many-level model of H I emission, including radiative transfer and collision processes (Luridiana et al. 2009), so our calculations result in explicit predictions of the $\mathrm{H}\alpha/\mathrm{H}\beta$ ratio. These are listed in Table 3. While the predicted Balmer decrements are slightly steeper than the Case B value that we used ($\log(\mathrm{H}\alpha/\mathrm{H}\beta) = 0.46$), there is little variation in the predicted Hα/Hβ ratio, so that the physics of the emission line formation could not create the effect we observe.

The basic SDSS galaxy sample is continuum-flux limited. As is described in Paper I, we selected emission-line galaxies from that sample using criteria that include a S/N ratio limit on the Hβ emission line and a very narrow redshift range, so our AGN sample is effectively Hβ-luminosity limited. For this reason, it is not surprising that the observed $L(\mathrm{H}\beta)$ given in Table 3.1 is constant across all of the subsamples. The strong trend in the dereddened $L(\mathrm{H}\beta)$ therefore comes strictly from the observed trend in the Hα/Hβ ratio from which we deduce $E(B-V)$. Can this Hα/Hβ trend be due to selection effects? For this to be true, we would need to either be systematically missing the high-ionization galaxies with the strongest Hα lines or the low-ionization galaxies with the weakest Hα lines. The latter seems more probable, but even for no reddening the Hα line is three times stronger than Hβ, so we do not see why such lines would be missed or incorrectly measured.

The actual subsamples used here reflect the AGN locus that was defined by the MFICA techniques described in Paper I. We are confident that we have correctly studied the physical properties of that sample.

3.4.2 [O III] and [N II] Temperatures

The major problem with these LOC models is that they do not reproduce the increase in the temperature-sensitive [O III] $\lambda4363/\lambda5007$ and [N II] $\lambda5755/\lambda6584$ ratios that is observed as one moves down the AGN sequence towards lower ionization, nor do the dust-free models reproduce the very high ratios that are reached. Our large galaxy sample has allowed this effect to be seen not only for the typical [O III] ratio but also for the [N II] ratio. Although neither ratio can be measured in the very lowest ionization case, Figure 3.2 shows that [O III] $\lambda4363$ is easily measured at all other cases and likewise, [N II] λ5755 is easily measured in our high moderate ionization subsets. In the low-density limit, the observed [O III] ratio for the high-ionization end of the AGN sequence gives a temperature of ~11,000 K and the observed [N II] ratio gives a temperature of ~9,000 K. The lowest-ionization subset for which the [O III] ratio can be measured (the a11 case) corresponds to a temperature of ~20,000 K in the low density limit. High temperatures have long been known to exist in some AGN (Shuder & Osterbrock 1981) and have also been discussed by Komossa & Schulz (1997) and Zhang, Liang & Hammer (2013).

The [O III] λ5007 and [N II] λ6584 lines become collisionally quenched at high densities, while [N II] λ5755 and [O III] λ4363 optimally emit. This could mean that the so called "temperature problem" is actually a density problem and that the [O III] and [N II] ratios are giving false temperatures. We used simple power laws to represent the radial and density distributions in our LOC models, but there could in principal be some other arrangement of the NLR that emphasizes high density gas. However, there are several problems with this scenario.

First, the [N II] λ5755 and [O III] λ4363 optimally emit in different regions of the LOC plane. So emphasizing a moderately high density (e.g. $\log(n_{\rm H}) \sim 6.5$) would solve the [N II] temperature problem but give an even worse fit to the [O III] temperature. Second, our low-density indicating line ratio, [S II] λ6716/ [S II] λ6731, fits the entire AGN sequence to within ~10 per cent and our high-density indicating line ratio, [S II] λ4070/ [S II] λ6720, fits the AGN sequence to within a factor of 2 or 3 down to all but the lowest ionization observed AGN subset. Finally, additional high density components would add substantial Balmer emission (since these lines emit strongly over a wide density range) which would result in underpredicting many key ratios (e.g. [O III] λ5007/Hβ, [S II] λ6720/ Hα, etc.). Indeed, Komossa & Schulz (1997) attempted to solve the "temperature problem" by emphasizing a high density component, only to find that it severely overestimated [O I] emission. Therefore, it is likely that the low ionization AGN really do contain low density gas with high T_e.

Figure 3.7 shows that [O III] λ4363 optimally emits at $\log(r) \sim 18.0$ while [O III] λ5007 optimally emits at $\log(r) \sim 19$. Similarly, [N II] λ5755 optimally emits at $\log(r) \sim 19.5$ while [N II] λ6584 optimally emits at $\log(r) \sim 21.0$. Therefore smaller values of the radial exponent (which correspond to less extended NLRs) should give larger [O III] and [N II] ratios and hence larger deduced T_e. However, the observations surprisingly show that the higher ionization cases have smaller [O III] and [N II] ratios even though the other line ratios indicate that higher ionization cases are the ones with the more concentrated NLRs (smaller fitted values of γ).

One possible explanation for the high temperatures is an increasing contribution of shock excitation at lower ionization. The shock models presented by Dopita & Sutherland (1995) do reach the high [O III] temperatures found in our subsets. However, their shock models that produce these high temperatures significantly overestimate the [O I] emission given in our lower ionization subsets. Most importantly, their shock models cannot reproduce the emission found in high excitation Seyfert galaxies, so our hope of unifying the low- and high-ionization AGN would have to be abandoned.

Another factor that could explain the high [O III] ratio in our low-ionization AGN is a decrease in metallicity. A decrease in metal abundances results in a decrease in cooling which raises the electron temperature. Komossa & Schulz (1997) studied this effect in luminous Seyfert 2 galaxies. Their models that resulted from scaling solar metal abundances by 0.3, which they favored, reproduce the [O III] ratio found in our low ionization subsets. This effect has an upper limit of log([O III] λ4363/ λ5007) ~ -1.3, but this is already larger than any [O III] ratio found in our subsets. However, studies with far larger samples than the one used by Komossa & Schulz (1997) have shown that Seyferts with subsolar metallicities are rare (Groves et al. 2006), so this explanation may be limited to low ionization AGN.

Photoelectric heating from grains can also increase the electron temperature enough to reproduce the temperature sensitive ratios found in the high-ionization Seyfert galaxies studied by Komossa & Schulz (1997) and G04b. Our dusty models have the same effect, producing an [O III] $\lambda4363/\lambda5007$ ratio that matches the moderate ionization subsets, but they do not accurately predict the highest ionization observations.

This problem might be ameliorated in models adding cosmic rays, shock excitation, turbulent heating or an increase in grain abundance in more extended regions of the NLR. Although a full study must be left for a future paper, we briefly explored one of these possibilities by running our dust-free and dusty model with a cosmic ray ionization rate 10^3 times greater than the Galactic background given by Indriolo et al. (2007). It is possible that AGN and starburst galaxies see a greater cosmic ray flux than other galaxies (Papadopoulos 2010). However, the extra heating by cosmic rays had a negligible effect on the [O III] and [N II] temperatures in both our dust free and dusty models, leaving the need for a deeper investigation of an additional component to address the temperature problem in low ionization AGN.

3.4.3 The Possibility of a Dusty Narrow Line Region

We were unable to find a set of free parameters for our dusty models that can account for systematic variations along the AGN locus. However, our results do not rule out the dusty models. Describing the NLR as either completely dusty or dust-free is likely to be a gross simplification for a complicated environment; it is indeed plausible that both dusty and dust-free regions exist.

A dusty, radiation pressure dominated NLR has previously been proposed by G04a and provides a different interpretation of the physical meaning behind the AGN locus. The basic premise behind that model is that radiation pressure exerted by the ionizing source upon grains, the photoelectric heating produced by the grains, and the ionizing photon absorption are non-negligible effects in the NLR. Similar effects occur in individual Galactic H II regions (e.g. the Orion Nebula; Baldwin et al. 1991). Aside from these effects, grains also deplete refractory elements and destroy resonance lines (e.g. Lyα λ1216).

In this case, the theoretical diagnostic diagrams computed by G04b indicate that for Z = $2Z_\odot$ a decrease in ionization along the AGN sequence represents a decrease in ionization parameter for a dusty, constant pressure NLR. The G04a models do not even consider the low ionization end of the AGN locus, nor do they fit the observed values for those cases. In addition, their interpretation was mostly limited to strong lines. For the weak line ratios that were included in this analysis, our dust-free models fit our subsets better than our dusty models and their dusty models clearly do not reproduce our subsets. In fact, their constant density, dust-free models are in better agreement with these lines.

Dusty models, as in G04b for example, are only capable of reproducing a narrow range of high ionization UV lines in NLR Seyferts (Nagao, Maiolino & Marconi 2006). In particular, dusty models for C IV λ1551/ He II λ1640 > 1.5 fail to match observations due to stagnation at low metallicity and high ionization parameter, while the dust-free models from F97 are successful. This suggests that at least part of the high ionization region of the NLR is dust free. One current physical picture envisions the NLR as a mixture of a dusty region responsible for lower ionization emission (e.g. [O III], [S II]) and a dust free component that emits coronal lines (e.g. [S VIII], [Fe X]) (Dopita et al. 2002).

Our analysis results in contradictory conclusions about the dust content. Komossa & Schulz (1997) favored a dust-free model mainly because their dusty model failed to predict strong, moderate ionization Fe line intensities (e.g. [Fe III] λ4658, [Fe VII] λ6087) due to highly depleted Fe abundances. F97 found that lower ionization regions were dusty and higher ionization regions dust free.

Low ionization lines may suggest that the gas is dusty. The [Fe III] line is not detected, with I([Fe III] λ4658)/I(Hβ) $< 0.020.04$. The predicted [Fe III]/Hβ ratios range from 0.05 for our highest ionization dust-free LOC model to 0.01 for our moderate ionization dusty model, which are too close to the observational limits to be conclusive. But at most, marginal depletion of Fe might be required to fit the observations. The [Ca II] $\lambda\lambda$7291, 7324 doublet is typically strong in dust-free regions (Kingdon, Ferland & Feibelman 1995). The [Ca II] λ7324 line is blended with [O II] λ7325, but we do not detect the [Ca II] λ7291 line. Our dust-free models predict that $I(\lambda 7291)/I(\mathrm{H}\beta) = 0.31$ for higher ionization AGN, and they also overpredict the [Ca II] λ7324/Hβ ratio at $I(\lambda 7324)/I(\mathrm{H}\beta) = 0.21$ since it is predicted to be larger than the [O II] λ7325/Hα emission line ratio. This indicates significant depletion of Ca onto dust.

On the other hand, high ionization lines suggest that the gas is dust free. The [Fe VII] λ6087 emission line is observed to be moderately strong in our higher-ionization subsets. The dust free model does correctly predict the [Fe VII] λ6087/Hα ratio over the range of ionization that it is observed, while the dusty model underpredicts this line by almost a factor of three.

All of this leaves the overall picture of the NLR's dust content unclear, and it likely that both high ionization dust-free and lower ionization dusty clouds exist in regions of the NLR. An ablating wind, as mentioned above, from inner regions could be dust-free and lead to a mixture of dust abundances.

F97 came across a similar problem. They found that low-ionization regions appeared to be dusty while high ionization region must be dust free to create strong high ionization Fe lines. The spectral diagnostics do not clearly indicate the ionization potential where the change occurs, so we cannot say whether any particular line might form in a dusty or dust free region. The results in Figure 3.13, which show that the intensity ratios involving low-ionization lines, such as I([N I] λ5200)/I([O II] λ7325) or I([O I] 6300)/I(Hα), fit the dust-free models better than the dusty models add to the confusion.

3.5 Conclusions

Spectral signatures of the dust content are inconclusive, as found in previous studies. It is likely that different regions have a different dust to gas ratio, perhaps because of their history. Luckily, the key spectral diagnostics used to reach the main conclusions of this paper are insensitive to whether or not our LOC models contain dust.

Our LOC models, in which only the radial extent of the gas is varied, successfully reproduce most of the BPT and VO87 diagnostic line ratios observed over the sequence of high- through moderate-ionization NLRs in narrow-lined AGN. This includes fitting the line ratios which depend most strongly on the abundances, gas density and spectral energy distribution. Our sequence of models also fit a number of the observed line ratios even for very low-ionization AGN. The most significant discrepancies between the observations and our models are that we cannot fit several important line ratios in the low-ionization objects, and in particular the models do not reproduce the high T_e implied by the large observed [O III] $\lambda4363/\lambda5007$ ratio.

We have shown that the high - moderate ionization AGN along the locus generated by MFICA represent a physically meaningful sequence in NLR properties. The most viable interpretation describes the sequence from high ionization to low ionization AGN as a change in the radial distribution of the NLR gas, which is proportional to changing the flux that is incident on each cloud. This finding states that higher ionization AGN contain optimally emitting clouds that are more concentrated towards the central continuum source than in lower ionization AGN, but that the density distribution is on average the same. Scaling from the Hβ luminosity, we have found that the central continuum source in low-ionization objects is more luminous than in high-ionization objects. The ionization sequence might be an age sequence, where the low-ionization objects are older and have systematically cleared out their central regions by radiation pressure.

The first index of the AGN locus can be understood by the radial distribution of clouds in the NLR, but the meaning behind the second index is most likely object-to-object scatter. The majority of diagnostic diagrams in Figure 3.8 show that the observed subsets corresponding to the two "wings" parallel to the AGN sequence ($j = 0$ and $j = 2$) are so similar to the central AGN locus ($j = 1$) that we cannot deduce any physical meaning from their differences. This supports describing the AGN sequence, from high at least through medium ionization, as a single-parameter sequence in the radial concentration of the NLR.

We arrived at these results by not only matching typical line ratio diagnostics based on the strongest emission lines but also by taking advantage of weaker lines for consistency checks. This allowed greater confidence in the temperature, density, abundances and ionizing continuum constrained from strong line ratios. We will continue this analysis with the SF sequence in a future paper where the physical properties of low ionization SF galaxies might overlap with those of low ionization AGN.

4 Theoretical Modeling of the Ionization Sequence in Star-Forming Galaxy Emission-Line Spectra

High ionization star forming galaxies are easily identified with strong emission line techniques such as the BPT diagram, but for ionization levels below log([O III]/Hβ) $\sim$ 0.3 they become confused with low-ionization AGN, making their physical interpretation difficult. Mean field independent component analysis (MFICA) is a novel approach to processing emission line spectra that can disentangle the AGN and starlight contributions to emission lines allowing the properties of pure AGN and pure starburst galaxies to be interpreted over a wide range of ionization. We applied MFICA to a large sample of low-z SDSS galaxies and created subsamples of pure star forming galaxies, resulting in a sequence of varying ionization. We used a locally optimally emitting cloud (LOC) model to fit emission line ratios that constrain the excitation mechanism, spectral energy distribution, abundances and physical conditions. Preliminary results in fitting diagrams that constrain the excitation mechanism indicate that the variation of starburst galaxies is due to a change in the radial distribution of clouds and confirms that MFICA is a powerful tool to assess differences in emission line properties solely due to starbursts. We briefly discuss future work that will decipher other properties in star forming galaxies.

4.1 Introduction

Starburst galaxies typically exhibit massive star formation, leading to an emission-line spectrum that is dominated by gas ionized by new O stars formed in molecular clouds. Early work by Baldwin, Phillips & Terlevich (1981), later expanded upon by Veilleux & Osterbrock (1987; hereafter VO87), showed that the intensity ratios of strong emission lines (known as "strong-line ratios") found in active galactic nuclei (AGN) and star forming (SF) galaxies can be used to classify the excitation mechanism in emission line galaxies. In particular, the plot of [O III] $\lambda5007$/ Hβ vs. [N II] $\lambda6584$/ Hα (hereafter the BPT diagram) has been remarkably successful at separating galaxies highly ionized by a central AGN from those ionized by intense starbursts. On the BPT diagram, SF galaxies fall in a well-defined region that spans approximately an order of magnitude in these ionization-sensitive line ratios.

One viable interpretation for explaining why SF galaxies exhibit such a wide range of ionization comes from differences in ionization parameter and metallicity (Kewley et al. 2001). The ionization parameter, U, is a convenient dimensionless number that describes the degree of ionization in a gaseous cloud and is defined as $U = \phi(\mathrm{H})/n_{\mathrm{H}}c$, where $\phi(\mathrm{H})$ is the ionizing photon flux and n_{H} is the hydrogen density. Optical line ratio diagrams found in Veilleux & Osterbrock (1987) were successfully reproduced over a large range in ionization by Kewley et al (2001). Subsequent work extended the analysis to include infrared line ratio diagnostics (Snijders, Kewley & van der Werf 2007) and low metallicity galaxies via the abundance sensitive [N II]/[O II] ratio (Levesque, Kewley & Larson 2010).

While this interpretation is valid at higher ionization, the fit at lower ionization becomes more uncertain due to possible entanglement with emission line properties resulting from an active galactic nucleus. Figure 4.1a shows the BPT diagram for the sample of galaxies used here (which is the same as was described in Paper I (Allen et al. 2013) and Paper II (Richardson et al. 2013). The solid and dashed

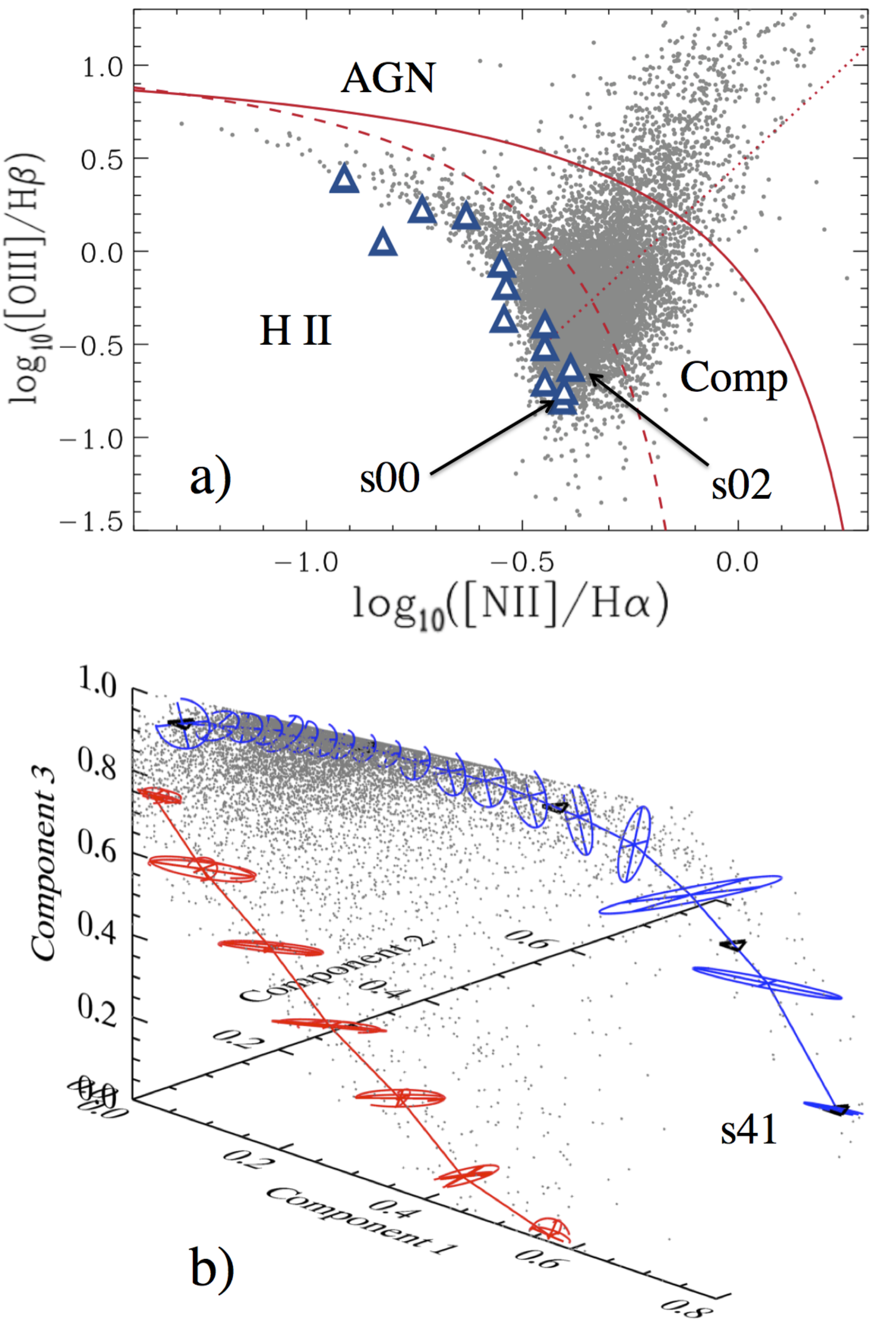

Figure 4.1 (Top panel) The BPT diagram for our sample of galaxies from Paper I. The red triangles show our sequences of pure SF picked out by MFICA with s4j representing the highest ionization observations. (Bottom panel) The 3-D MFICA classification diagram with axes representing the strengths of the first three MFICA components. In this representation the AGN locus appears as the red line, and the SF locus is the blue line.

lines represent classification curves from Kewley et al. (2001) and Kauffmann et al. (2003), and respectively define the upper and lower limits on the number of SF galaxies. The dotted line represents the Kauffmann et al. (2003) line that divides a class of low ionization objects (LINERs) from more classical AGN. The correct classification of AGN and SF galaxies is readily apparent at higher ionization due to the large degree of separation in [N II] $\lambda6584/$ Hα above log([O III/Hβ]) ~ 0.3. However below this threshold, the two "branches" of AGN and SF galaxies merge to form a region containing a mix of star-forming galaxies, AGNs and composite cases. The actual theoretical boundary between AGN and SF galaxies, and the degree of mixing between the two, is a matter of debate (Kewley et al 2001; Kauffmann et al. 2003; Kewley et al. 2006; Stasińska et al. 2006). Therefore, it is likely that previous models are limited in their interpretation of galaxies that lie inside the composite region. Furthermore, optical analysis has largely been limited to classical line ratio diagrams from Veilleux & Osterbrock (1987). Additional diagrams could provide additional constraints or consistency checks on models developed from strong line techniques.

In Allen et al. (2013) we showed that a variant of blind source separation, known as mean field independent component analysis (MFICA), successfully alleviates the restriction of tangled emission line components from AGN and starlight excitation. We direct the reader to Paper I and Paper II for a more detailed description of the MFICA procedure, but we provide a summary of it here. Using MFICA, we generated a series of continuum and emission line components using a small subset of our $\sim 10^4$ low redshift ($0.1 < z < 0.12$) galaxies sample from the Sloan Digital Sky Survey (SDSS) to match our full galaxy sample. The unique signatures of AGN and SF galaxies in our MFICA parameter space allowed the isolation of "pure" SF and AGN galaxies over a large range of ionization. Our sample size also enabled many weaker lines to be accurately measured by coadding spectra.

Figure 4.1b, taken from Figure 1b in Paper II, again shows the BPT diagram but in a more abstract sense with the axes representing components from MFICA. The degree of separation between both sequences is clear. All but the lowest ionization point of each sequence occupies a unique parameter space. This outlines the key point that a single parameter is responsible for the variation in the AGN and SF components in emission line galaxies.

In Paper II we took advantage of this degree of separation by performing plasma simulations with the spectral synthesis code Cloudy (Ferland et al. 1998) to reproduce AGN observations over a wide range of ionization with a locally optimally emitting cloud (LOC) model (Ferguson et al. 1997). This model states the cumulative observed emission from emission line galaxies is the result of selection effects stemming from various emission lines optimally emitted from a large number of gas clouds spanning a vast range in physical conditions. After integrating over clouds with a wide range of gas density and radial distance from the ionizing continuum source, weighting the gas clouds by power laws in these two parameters, we found that almost all of our higher to moderate ionization diagnostic line ratios could be represented by change in radial integration weighting. In several cases, especially for the classical line ratio diagrams, we fit the entire sequence of observations from Seyferts all the way down to low ionization nuclear emitting regions (LINERs). This finding emphasized the success of MFICA in isolating galaxies with only AGN activity. In addition, we also used weaker lines in diagnostic diagrams to act as consistency checks on our models.

In the present work, we perform a similar analysis for our subsets of SF galaxies. LOC models have successfully reproduced observations in the NLR (Ferguson et al. 1997) and BLR (Korista et al. 1997) of AGN and here, for the first time, we extend the use of LOC models to describe emission from SF galaxies. As was the case in Paper II for AGN galaxies, finding a physically meaningful parameter to reproduce variation of SF galaxies over the entire length of the SF locus is the goal of this work.

Our overall aim is to test the hypothesis that the range in ionization present in the SF sequence is either due to the variation in the central concentration of gas clouds (as in Paper II), starburst age or metallicity.

In §4.2, we describe five roughly equally spaced points along the MFICA SF locus. Then in §4.3 we describe our current LOC model and the preliminary results for classical diagrams that constrain excitation mechanisms. Finally, we outline future work in §4.4.

4.2 Observations

In Paper I, we showed that MFICA allows a degree of separation between SF galaxies and AGN that we can exploit here in order to define and interpret a pure sample of low-ionization star forming galaxies over a large range of ionization. Here, we present five subsamples of SF galaxies identified by MFICA that extend over the entire length of the SF locus. These subsamples correspond to "pure" SF galaxies where the emission lines are solely the result of starburst excitation. We also identify two parallel wing sequences of SF galaxies, on opposite sides of the central sequence. After the continuum components were fitted to each individual galaxy using MFICA, a composite emission line spectrum was generated at each locus point by co-adding the continuum subtracted spectra in each subsample. We adopt the same nomenclature as in Paper II by naming the points along the sequence in the format sij. The first index, i, indicates the ionization with $i = 4$ corresponding to high ionization starburst galaxies and $i = 0$ corresponding to low ionization SF galaxies. The second index, j, describes the position of the sequence orthogonal to the SF locus with $j = 1$ designating the central sequence, $j = 0$ the subsets positioned closest to galaxies with

Table 4.1: Properties of sij subsets

Subset	s00	s01	s02	s10	s11	s12	s20	s21	s22	s30	s31	s32	s40	s41	s42
$E(B-V)$	0.69	0.68	0.67	0.37	0.44	0.49	0.28	0.28	0.30	0.15	0.20	0.27	0.14	0.14	0.14
Component 1	0.00	0.02	0.05	0.00	0.01	0.02	0.00	0.04	0.10	0.18	0.24	0.30	0.53	0.52	0.52
Component 2	0.06	0.04	0.02	0.32	0.31	0.29	0.57	0.54	0.50	0.74	0.59	0.43	0.47	0.44	0.40
Component 3	0.93	0.90	0.87	0.68	0.67	0.65	0.42	0.41	0.39	0.05	0.16	0.27	0.00	0.02	0.06

AGN and $j = 2$ the subsets located on the opposite side.

Figure 4.1 displays these sequences on the traditional BPT diagram and our "3D" BPT diagram. Figure 4.1a shows the highest ionization SF galaxies are isolated, leaving little ambiguity about their excitation mechanism. However, the lowest ionization subsets descend into regions close to that of composite galaxies, leading to questions about whether AGN have contributions to emission lines seen in this low ionization SF subsets. However, as Figure 4.1b shows, MFICA has enabled the isolation of quite pure subsamples of galaxies. At the low ionization end of the SF sequence, there is minimal overlap with the AGN sequence.

Table 4.1 lists the MFICA component weights that define each of the subsamples along the SF sequence. From the large SDSS sample, we identified for each subsample the 50 galaxies which lie closest to the defining point of that subsample in terms of their MFICA component weights, and co-added their spectra to make an average subsample spectrum. Figure 4.2 displays several regions of the co-added spectra for our central sequence; the wing sequences are not displayed due to their close similarity to the central sequence.

As was done in Paper II for the AGN in the sample, the emission lines present in the co-added spectra of these SF galaxies were measured by subtracting a locally fitted continuum for each spectrum and then integrating the flux within each line profile. The [S II] doublet was separated by integrating to the lowest point in the blended region between the two lines. Strong Na D absorption can be seen in our lowest ionization subsets blending together with He I $\lambda5876$. We de-blended these lines by fitting the He I line with the profile from Hβ, yielding an uncertainty of around 10 per cent. Table 4.2a lists our observed emission line fluxes and Table 4.2b lists those same lines but dereddened assuming a standard galactic reddening curve with an $E(B-V)$ that gives a dereddened $I(\mathrm{H}\alpha)/I(\mathrm{H}\beta) = 2.86$, appropriate for Case B recombination lines with an electron temperature $T_e = 10^4$ K and an electron den-

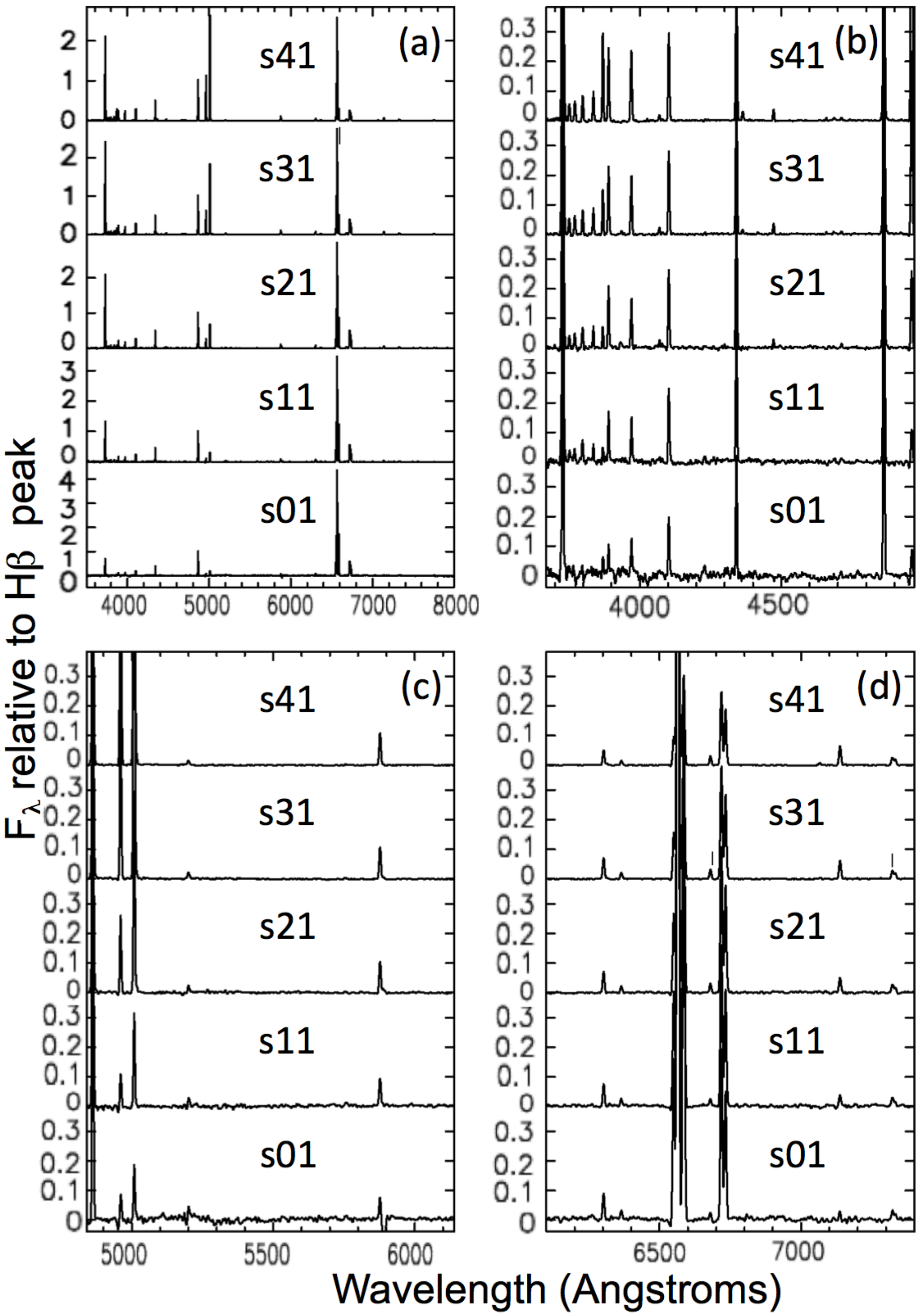

Figure 4.2 Observed, coadded spectra for the five subsamples that fall directly along central the SF locus. Panel (a) shows the full spectra. The other panels show enlargements that slightly overlap in wavelength. All flux values are shown in units of the peak Hβ intensity in the particular spectrum.

Table 4.2a: The measured emission line strengths for the SF locus. Measurements are relative to Hβ.

Ion	λ_{air}	s00	s01	s02	s10	s11	s12	s20	s21	s22	s30	s31	s32	s40	s41	s42
[O II]	3727	0.73	0.74	0.77	1.28	1.34	1.39	2.05	2.01	1.92	2.66	2.36	2.08	2.11	2.10	2.08
H I	3750	<0.03	<0.03	<0.04	0.04	0.03	0.03	0.04	0.03	0.05	0.05	0.04	0.04	0.04	0.04	0.04
H I	3771	<0.01	<0.01	<0.00	0.03	0.04	0.01	0.05	0.04	0.04	0.05	0.05	0.05	0.05	0.05	0.05
H I	3798	<0.00	<0.01	<0.02	0.05	0.06	0.04	0.05	0.06	0.06	0.06	0.06	0.06	0.06	0.06	0.06
H I	3835	<0.02	<0.03	<0.04	0.06	0.05	0.05	0.05	0.05	0.07	0.07	0.07	0.07	0.07	0.07	0.07
[Ne III]	3869	0.05	0.05	0.05	0.07	0.03	0.06	0.05	0.05	0.06	0.15	0.11	0.10	0.22	0.22	0.23
H I	3889	0.08	0.09	0.09	0.14	0.13	0.12	0.16	0.16	0.18	0.19	0.18	0.18	0.20	0.20	0.20
H I	3970	0.11	0.13	0.14	0.11	0.13	0.14	0.13	0.14	0.16	0.19	0.18	0.18	0.22	0.22	0.23
[S II]	4070	<0.05	<0.04	<0.01	<0.01	<0.02	0.03	0.03	0.03	0.02	0.03	0.02	0.02	0.02	0.02	0.02
H I	4102	0.18	0.18	0.16	0.20	0.21	0.21	0.21	0.21	0.23	0.24	0.23	0.24	0.25	0.25	0.25
[Fe V]?	4229	0.04	0.05	0.06	0.03	0.02	<0.01	<0.01	<0.01	<0.00	<0.01	<0.00	<0.01	<0.00	<0.00	<0.00
H I	4340	0.34	0.34	0.34	0.40	0.40	0.40	0.40	0.42	0.42	0.43	0.43	0.43	0.45	0.45	0.45
[O III]	4363	<0.00	<0.00	<0.00	<0.00	<0.00	<0.00	<0.00	<0.00	<0.01	0.01	0.01	0.01	0.03	0.03	0.03
He I	4471	<0.01	<0.00	<0.00	<0.02	<0.00	<0.00	0.03	0.02	0.02	0.03	0.03	0.03	0.03	0.03	0.03
He II	4686	<0.00	<0.00	<0.01	<0.01	<0.01	<0.00	<0.00	<0.00	<0.01	0.00	0.01	0.01	0.01	0.01	0.01

Table 4.2a (cont'd)

Ion	$\lambda_{\rm air}$	s00	s01	s02	s10	s11	s12	s20	s21	s22	s30	s31	s32	s40	s41	s42
[Ar IV]	4711	<0.01	<0.01	<0.01	<0.03	<0.02	<0.02	0.02	0.01	0.01	0.01	0.01	0.01	0.01	0.01	0.01
H I	4861	1.00	1.00	1.00	1.00	1.00	1.00	1.00	1.00	1.00	1.00	1.00	1.00	1.00	1.00	1.00
[O III]	4959	0.07	0.08	0.10	0.09	0.12	0.15	0.18	0.25	0.30	0.68	0.58	0.55	1.05	1.06	1.08
[O III]	5007	0.18	0.20	0.26	0.21	0.33	0.43	0.46	0.68	0.90	1.16	1.76	1.63	2.52	2.54	2.56
[N I]	5200	0.04	0.05	0.04	0.02	0.03	0.04	0.03	0.02	0.03	0.03	0.03	0.03	0.02	0.02	0.02
[N II]	5755	<0.01	<0.02	<0.01	<0.01	<0.02	<0.01	<0.01	<0.00	<0.01	0.00	0.00	0.01	0.00	0.00	0.00
He I	5876	0.09	0.09	0.09	0.09	0.11	0.12	0.12	0.12	0.13	0.12	0.13	0.14	0.13	0.13	0.13
[O I]	6300	0.10	0.10	0.11	0.07	0.08	0.11	0.09	0.08	0.09	0.09	0.09	0.09	0.06	0.06	0.06
[O I]	6363	0.03	0.03	0.05	0.02	0.03	0.03	0.03	0.02	0.03	0.03	0.03	0.03	0.02	0.02	0.02
[N II]	6548	0.70	0.69	0.71	0.43	0.48	0.51	0.32	0.33	0.34	0.14	0.20	0.28	0.13	0.13	0.13
H I	6563	5.86	5.79	5.74	4.21	4.49	4.77	3.82	3.83	3.92	3.34	3.51	3.78	3.31	3.30	3.29
[N II]	6584	2.32	2.30	2.36	1.51	1.61	1.71	1.10	1.11	1.11	0.50	0.66	0.89	0.41	0.41	0.40
He I	6678	0.02	0.02	0.03	0.03	0.03	0.04	0.03	0.04	0.04	0.04	0.04	0.04	0.04	0.04	0.04
[S II]	6716	0.77	0.78	0.79	0.66	0.72	0.78	0.71	0.64	0.59	0.51	0.50	0.49	0.33	0.33	0.32
[S II]	6731	0.59	0.59	0.59	0.50	0.53	0.59	0.52	0.49	0.45	0.38	0.38	0.39	0.26	0.26	0.25
[Ar III]	7135	0.02	0.03	0.04	0.04	0.05	0.05	0.06	0.06	0.07	0.07	0.08	0.09	0.09	0.09	0.09

Table 4.2a (cont'd)

Ion	$\lambda_{\rm air}$	s00	s01	s02	s10	s11	s12	s20	s21	s22	s30	s31	s32	s40	s41	s42
[O II]	7325	0.07	0.07	0.08	0.02	0.06	0.06	0.06	0.05	0.06	0.06	0.06	0.07	0.06	0.06	0.06

Table 4.2b: The dereddened emission line strengths for the SF locus. Measurements are relative to Hβ.

Ion	λ_{air}	s00	s01	s02	s10	s11	s12	s20	s21	s22	s30	s31	s32	s40	s41	s42
[O II]	3727	1.59	1.59	1.63	1.94	2.17	2.41	2.80	2.75	2.70	3.15	2.94	2.81	2.46	2.45	2.42
H I	3750	<0.06	<0.07	<0.08	0.06	0.05	0.05	0.05	0.04	0.06	0.05	0.05	0.06	0.05	0.05	0.05
H I	3771	<0.03	<0.02	<0.01	0.05	0.06	0.02	0.07	0.05	0.06	0.06	0.06	0.07	0.06	0.06	0.06
H I	3798	<0.01	<0.03	<0.04	0.07	0.10	0.06	0.07	0.07	0.08	0.08	0.08	0.08	0.07	0.07	0.07
H I	3835	<0.04	<0.06	<0.08	0.09	0.07	0.08	0.07	0.07	0.09	0.08	0.08	0.09	0.08	0.08	0.08
[Ne III]	3869	0.11	0.10	0.09	0.10	0.05	0.09	0.07	0.06	0.08	0.17	0.14	0.13	0.25	0.26	0.26
H I	3889	0.17	0.18	0.17	0.20	0.20	0.20	0.21	0.21	0.24	0.22	0.22	0.24	0.23	0.23	0.23
H I	3970	0.20	0.24	0.26	0.15	0.19	0.21	0.17	0.18	0.20	0.22	0.22	0.23	0.25	0.25	0.26
[S II]	4070	<0.08	<0.06	<0.02	<0.02	<0.02	0.04	0.04	0.04	0.03	0.04	0.03	0.03	0.02	0.02	0.02
H I	4102	0.30	0.30	0.28	0.27	0.29	0.31	0.27	0.26	0.29	0.27	0.27	0.30	0.28	0.28	0.28
[Fe V]?	4229	0.07	0.07	0.10	0.04	0.02	0.01	<0.01	<0.01	<0.00	<0.01	<0.00	<0.01	<0.00	<0.00	<0.00
H I	4340	0.49	0.50	0.49	0.50	0.51	0.52	0.46	0.49	0.50	0.47	0.48	0.50	0.49	0.48	0.48
[O III]	4363	<0.00	<0.01	<0.00	<0.00	<0.00	<0.00	<0.00	<0.00	<0.01	0.01	0.01	0.01	0.03	0.03	0.03
He I	4471	<0.01	<0.01	<0.00	<0.02	<0.00	<0.00	0.03	0.02	0.03	0.03	0.03	0.03	0.03	0.03	0.03
He II	4686	<0.00	<0.01	<0.01	<0.01	<0.01	<0.00	<0.00	<0.00	<0.01	0.00	0.01	0.01	0.01	0.01	0.01

Table 4.2b (cont'd)

Ion	λ_{air}	s00	s01	s02	s10	s11	s12	s20	s21	s22	s30	s31	s32	s40	s41	s42
[Ar IV]	4711	<0.01	<0.01	<0.01	<0.03	<0.02	<0.02	0.02	0.01	0.01	0.01	0.01	0.01	0.01	0.01	0.01
H I	4861	1.00	1.00	1.00	1.00	1.00	1.00	1.00	1.00	1.00	1.00	1.00	1.00	1.00	1.00	1.00
[O III]	4959	0.07	0.08	0.10	0.09	0.11	0.15	0.17	0.24	0.29	0.67	0.57	0.54	1.04	1.05	1.07
[O III]	5007	0.16	0.18	0.24	0.20	0.31	0.41	0.44	0.66	0.87	1.14	1.71	1.58	2.48	2.49	2.52
[N I]	5200	0.03	0.04	0.04	0.02	0.03	0.03	0.03	0.02	0.03	0.03	0.03	0.03	0.02	0.02	0.02
[N II]	5755	<0.01	<0.01	<0.01	<0.01	<0.01	<0.01	<0.00	<0.00	<0.01	0.00	0.00	0.01	0.00	0.00	0.00
He I	5876	0.06	0.05	0.05	0.07	0.08	0.09	0.10	0.10	0.10	0.11	0.11	0.11	0.12	0.12	0.12
[O I]	6300	0.05	0.05	0.06	0.05	0.06	0.07	0.07	0.06	0.07	0.08	0.07	0.07	0.06	0.06	0.06
[O I]	6363	0.01	0.02	0.03	0.01	0.02	0.02	0.02	0.02	0.02	0.03	0.02	0.02	0.02	0.02	0.02
[N II]	6548	0.34	0.34	0.36	0.29	0.31	0.31	0.24	0.25	0.25	0.12	0.16	0.21	0.11	0.11	0.11
H I	6563	2.86	2.86	2.86	2.86	2.86	2.86	2.86	2.86	2.86	2.86	2.86	2.86	2.86	2.86	2.86
[N II]	6584	1.12	1.13	1.17	1.02	1.02	1.02	0.82	0.83	0.81	0.43	0.53	0.67	0.35	0.35	0.35
He I	6678	0.01	0.01	0.02	0.02	0.02	0.02	0.02	0.03	0.03	0.03	0.03	0.03	0.03	0.03	0.03
[S II]	6716	0.36	0.37	0.37	0.44	0.44	0.45	0.52	0.47	0.42	0.44	0.40	0.36	0.28	0.28	0.28
[S II]	6731	0.27	0.27	0.28	0.33	0.33	0.34	0.38	0.35	0.32	0.33	0.31	0.29	0.22	0.22	0.22
[Ar III]	7135	0.01	0.01	0.02	0.03	0.03	0.03	0.04	0.04	0.05	0.06	0.06	0.06	0.07	0.07	0.07

Table 4.2b (cont'd)

Ion	λ_{air}	s00	s01	s02	s10	s11	s12	s20	s21	s22	s30	s31	s32	s40	s41	s42
[O II]	7325	0.03	0.03	0.03	0.01	0.03	0.03	0.04	0.04	0.04	0.05	0.05	0.05	0.05	0.05	0.05

sity $n_e = 10^2$ cm^{-3} (Osterbrock & Ferland 2006; hereafter AGN3). We compare our models below to the dereddened line strengths. Our large sample of pure SF galaxies has enabled the measurement of several weak lines that are not usually detectable in lower-quality spectra, including [S II] λ4070, [Ar IV] λ4711, [N I] λ5200, [Ar III] λ7135 and [O II] λ7325.

4.3 Preliminary Modeling Results

The LOC model is based on a grid of individual models at different densities and different distances from the source. After determining the spectral energy distribution (SED) and chemical abundances, the main free parameters correspond to the radial distribution of clouds from the ionizing source and the density distribution of those clouds.

We used version c10.00 of the plasma simulation code Cloudy to compute our LOC models. As in Paper II, and Ferguson et al. (1997), we assumed there is no attenuation of the incident continuum by ISM clouds. Our solar abundance set comes from Groves et al. (2004a), which were taken from a series of papers (Asplund et al. 2000; Asplund 2000, 2003; Allende Prieto et al. 2001, 2002); otherwise, our heavy element abundances come from the solar composition in Ferguson et al. (1997).

Typical starburst galaxies have luminosities $L_{\rm ion} = 10^{43.5}$ ergs s^{-1} so we used this value for our central ionizing source. Plasmas with $T_e < 4000$ K or $T_e > 10^5$ K do not principally contribute to optimal emission, therefore we use these conditions as limits on the Cloudy models used in our simulations.

We ran grids of simulations varying the distance from the source r, from 10^{16} cm to 10^{23} cm and the total hydrogen density, $n_{\rm H}$ from 10^0 cm^{-3} to 10^{10} cm^{-3}. The resolution of our grid resulted in 7171 total clouds evenly distributed in the log of our parameter space. Each simulation assumed constant total hydrogen density; however, the molecular and electron density were allowed to change with depth. We assumed that the ionizing source was isotropically emitting so that $\phi(\mathrm{H}) \propto r^2$. For our preliminary analysis, all of our simulation grids were dust-free.

The LOC model is based on the assumption that the emission we observe stems from selection effects; optimal emission line production occurs in different conditions for different emission lines and we only see the cumulative emission from many clouds. This spectrum is largely determined by radial and density distribution of clouds from the source. As in Paper II (see also Ferguson et al. 1997; Baldwin et al. 1995), our model defined the radial and density distributions of gas as $f(r) \propto r^{\gamma}$ and $g(n) \propto n_{\mathrm{H}\beta}$, respectively, where γ and β are free parameters. The total line luminosity is then simply,

$$L_{\mathrm{line}} \propto \int \int r^2 F(r, n_{\mathrm{H}}) r^{\gamma} n_{\mathrm{H}}^{\beta} dn_{\mathrm{H}} dr \tag{4.1}$$

(Paper II) where $F(r, n_{\mathrm{H}})$ is the flux of the line and $r^{\gamma} n_{\mathrm{H}}^{\beta}$ is the spatial distribution function. For simplicity, we chose the same integration limits as in Paper II, however we note that this only had small effects on the cumulative observed emission. Other properties, such as the SED, abundances and gas distributions had far more noticeable effects. Therefore gas with $\log(n_{\mathrm{H}}) > 8$ was not included due to collisional quenching, and gas with $\log(n_{\mathrm{H}}) < 2$ was not included due to low optical line intensities.

From here, the predicted emission can constrain the properties of these galaxies by utilizing line ratio diagnostics in the same manner as VO87, and many other subsequent papers. Our preliminary diagnostic diagrams will focus on classical line ratios that have been empirically determined to constrain the excitation mechanism in emission line galaxies.

4.3.1 Spectral Energy Distribution

We used the evolutionary synthesis code Starburst99 to generate synthetic starburst spectra for our simulations. Several factors influence the radiation field: metallicity, star formation history (SFH), and stellar population age and evolution. For simplicity, we chose to adopt the Padova track evolutionary sequence with AGB stars (Bressan et al. 1993) and Pauldrach / Hillier model atmospheres (Pauldrach et al. 2001; Hillier & Miller 1998) for all of our SEDs. We also assumed a Kroupa initial mass function (IMF; Kroupa 2001) with mass intervals of 0.1 $M_\odot$ to 0.5 $M_\odot$ and 0.5 $M_\odot$ to 100 $M_\odot$.

This leaves three additional properties of the SED, SFH, stellar population age and metallicity. Here we investigate the effects of varying the first two of these. We used two star formation histories for the incident radiation field of our simulations: instantaneous and continuous. Instantaneous starbursts assume that a population of massive stars formed with single burst of star formation while continuous starbursts continue to evolve until there is balance between newly born stars and the death of older stars. Our instantaneous starbursts assumed a fixed mass of 10^6 $M_\odot$, while our continuous starbursts assumed a star formation rate of 1 $M_\odot$ yr^{-1}.

Figure 4.3 displays the SEDs for our continuous (Figure 4.3a) and instantaneous (Figure 4.3b) starbursts as a function of age for solar metallicity. For a stellar population that has only undergone a single burst of star formation at 0 Myr, the hardness of the SED at high energies begins to decrease as a function of age due to hot OB stars evolving off the main sequence. Figure 4.3b illustrates this by showing that after 2 Myr (red line) the intensity of the FUV spectra drops off rapidly. This effect is less prominent in lower metallicity populations due to less ionizing photons being absorbed by metals in stellar atmospheres (Snijders et al. 2007). In our preliminary analysis, we have only considered a solar metallicity cluster of stars for both SFHs.

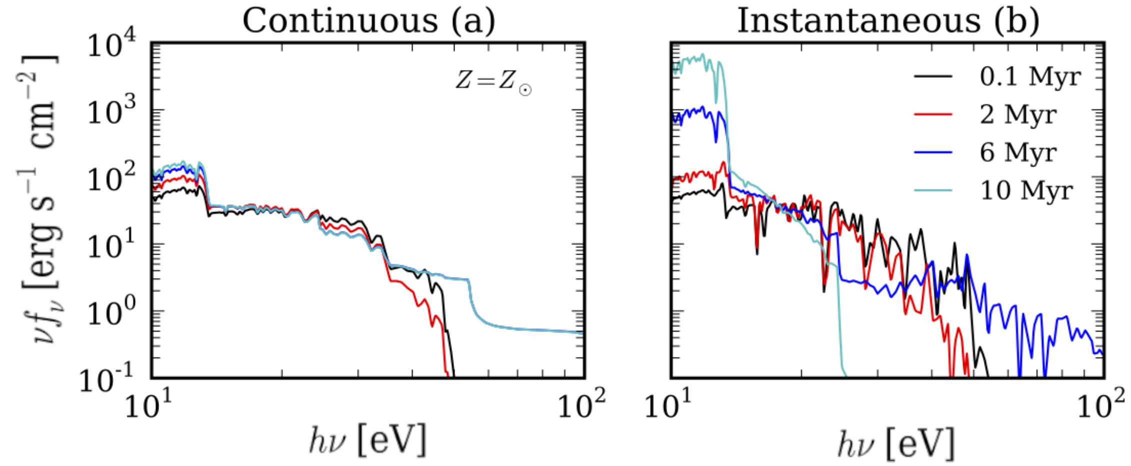

Figure 4.3 The SEDs for continuous (Panel a) and instantaneous (Panel b) star formation histories as a function of age for a cluster of solar metallicity stars. As the continuous starburst ages, the birth and death of stars eventually comes into equilibrium and the SED ceases to evolve. In contrast, instantaneous starburst undergo a single period of star formation, as evident by the sharp decrease in intensity past ∼25 eV for a 10 Myr cluster of stars.

4.3.2 Excitation Mechanism Diagrams

Using the SEDs given above we ran LOC integrations (following the same procedures as in Paper II) to compare our predicted emission line ratios to the observed values in our subsets. The VO87 diagnostic diagrams constrain the excitation mechanism and therefore designate the first order comparison needed to show that MFICA is correctly isolating SF galaxies. Figure 4.4 shows the predicted emission line ratios as colored circles connected by a solid line. Each set of circles represents a different density distribution in the range -1.8 $\leq \beta \leq$ -0.6 in increments of -0.4. The arrow in the corner indicates the direction of more negative β values. The circles within each set represent different radial distributions ranging from -2.0 $\leq \gamma \leq$ 2.0 in increments of 0.25. The largest circle in each set represents the most negative γ value. The white circle represents our current best fit to the highest ionization subset and is described below. The observations from the subsets along the central SF locus are also given

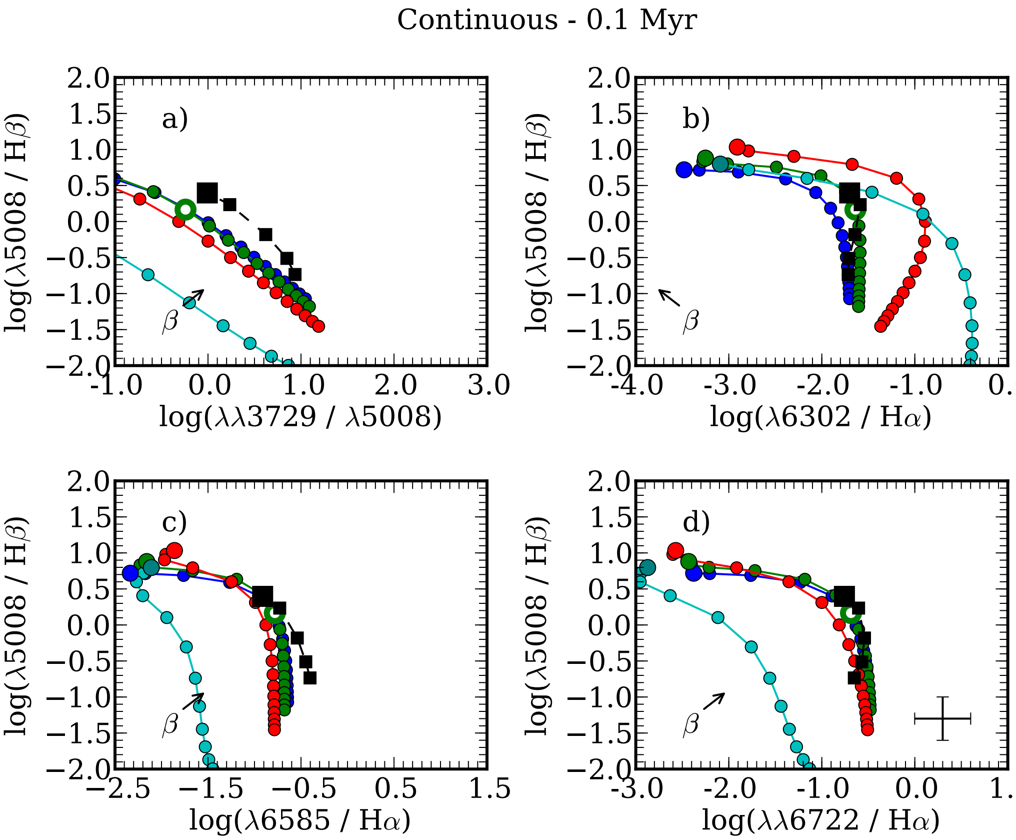

Figure 4.4 Diagnostic diagrams from VO87 for a continuous SFH as a function of age. Each quadrant represents a different starburst age. In each subpanel the squares connected by the dashed black line are the dereddened measurements from the co-added spectra that constitute the s41-s31-s21-s11-s01 sequence. We do not show the other SF sequences due to their similarity to the central sequence. The largest shape in the sequence indicates observations at the top of SF locus (s41). The colored lines with circles represent LOC integrations. The density-weighting indices in the LOC integrations, β, have more negative values along the direction of the arrow and are indicated by different colors. The radial weighting indices, β, become more negative as a function of increasing distance from the largest colored circle for each particular density weighting. The hollow circle indicates our best fitting set of free parameters that match the a41 subset (large black square) in the 0.1 Myr starburst. The cross in the lower right panel of each section indicates the range of acceptable error.

Figure 4.4 (cont'd)

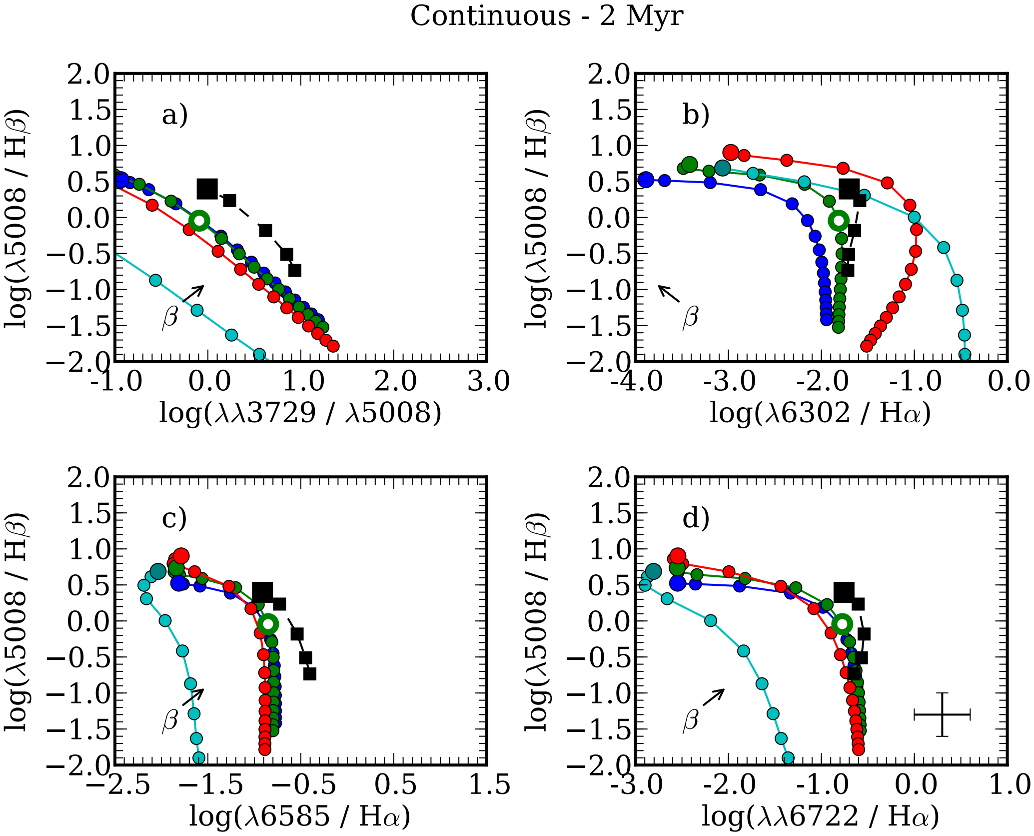

Figure 4.4 (cont'd)

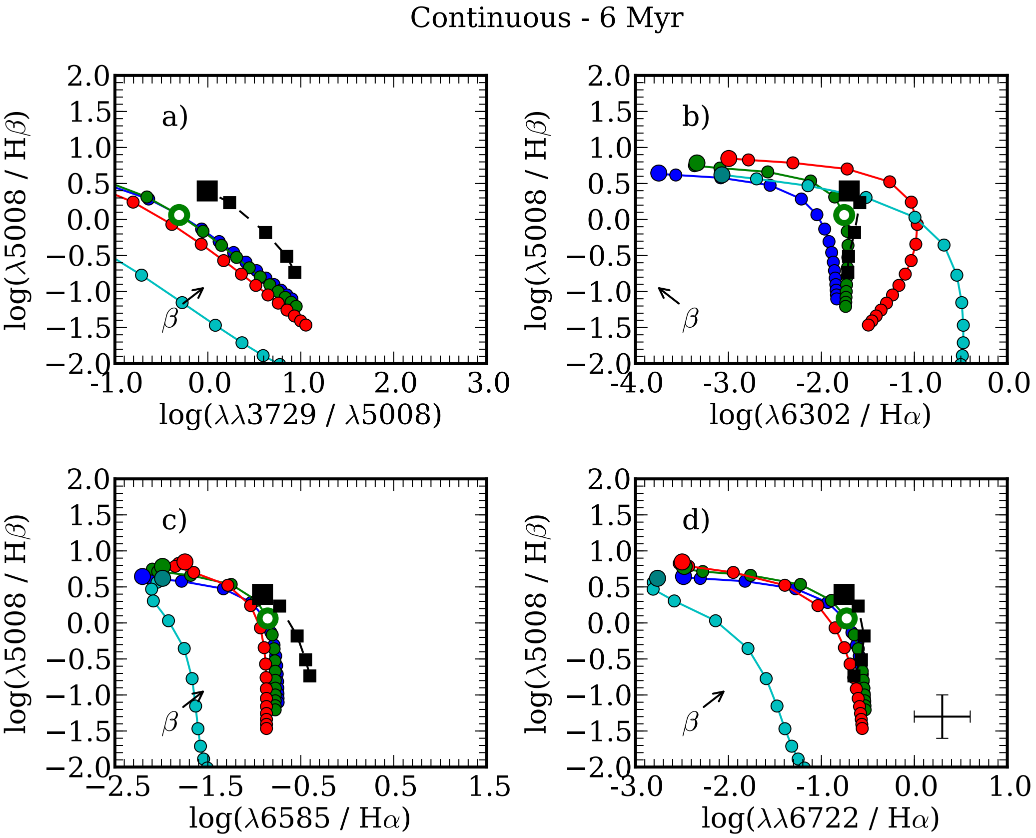

Figure 4.4 (cont'd)

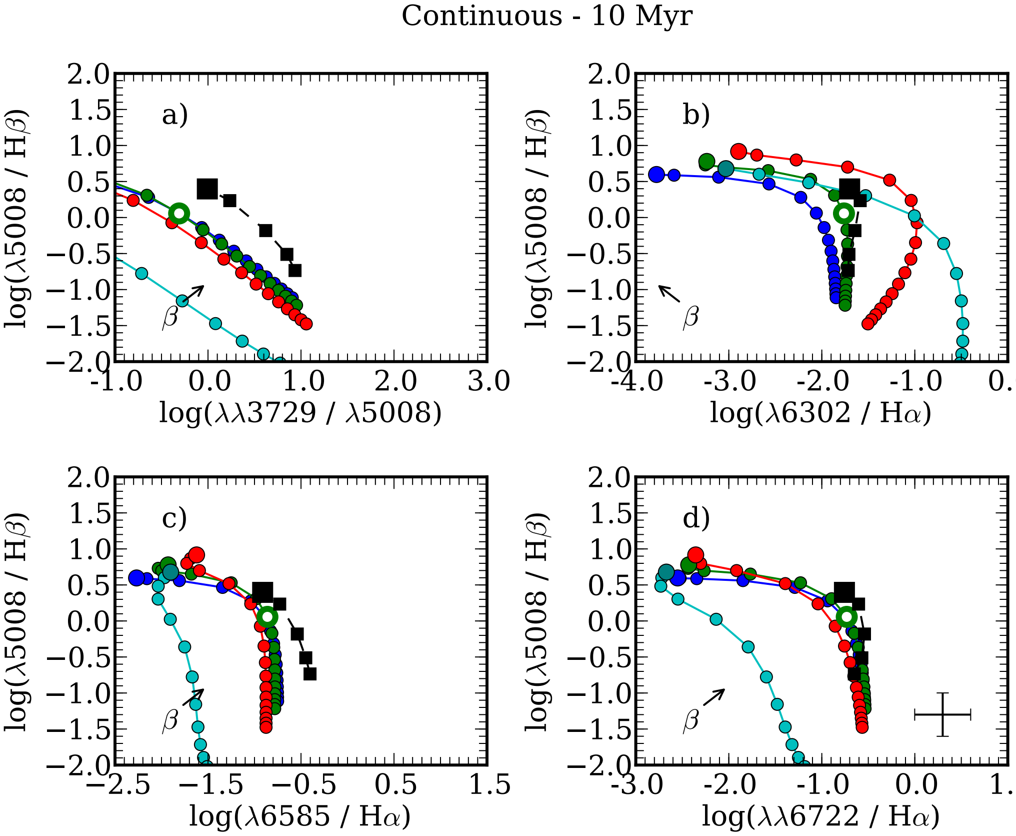

as black squares on these diagrams. We have chosen to only show the central locus on these diagrams since the wing loci are very similar to the central locus, as can be seen in Figure 4.2.

Figure 4.4 shows our VO87 diagrams for a starburst with a continuous SFH with each quadrant showing a different stellar population age. All emission line ratios decrease by ∼0.2 dex between 0.1 Myr and 2 Myr, except for [O II] / [O III], which increases.

Between these ages, the Balmer emission line equivalent widths, which are relatively flat across the LOC plane, decrease by a smaller amount than the maximum equivalent widths of the forbidden lines in these diagrams, thus most of the emission line ratios decrease. However, the [O II] λ3727 equivalent widths decrease more slowly than the [O III] λ5007 equivalent widths leading to a larger [O II] / [O III] ratio.

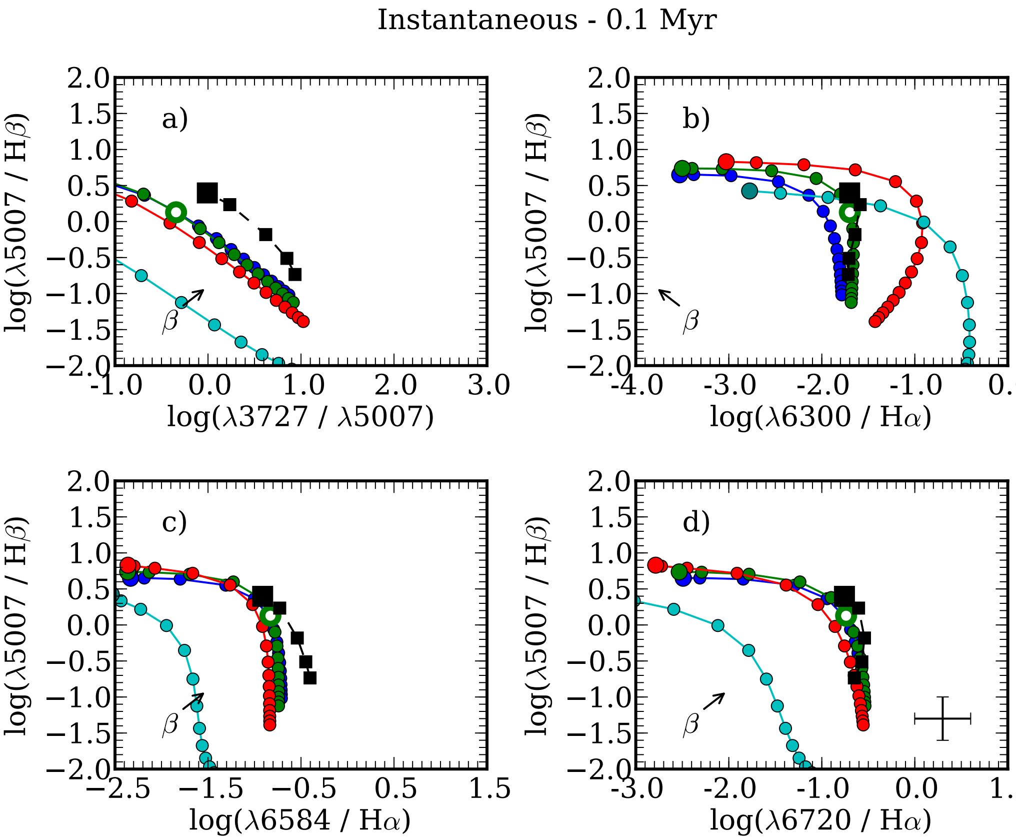

Figure 4.5 Diagnostic diagrams from VO87 for a instantaneous SFH as a function of age, displayed in the same manner as Figure 4.4.

Figure 4.5 (cont'd)

Instantaneous - 2 Myr

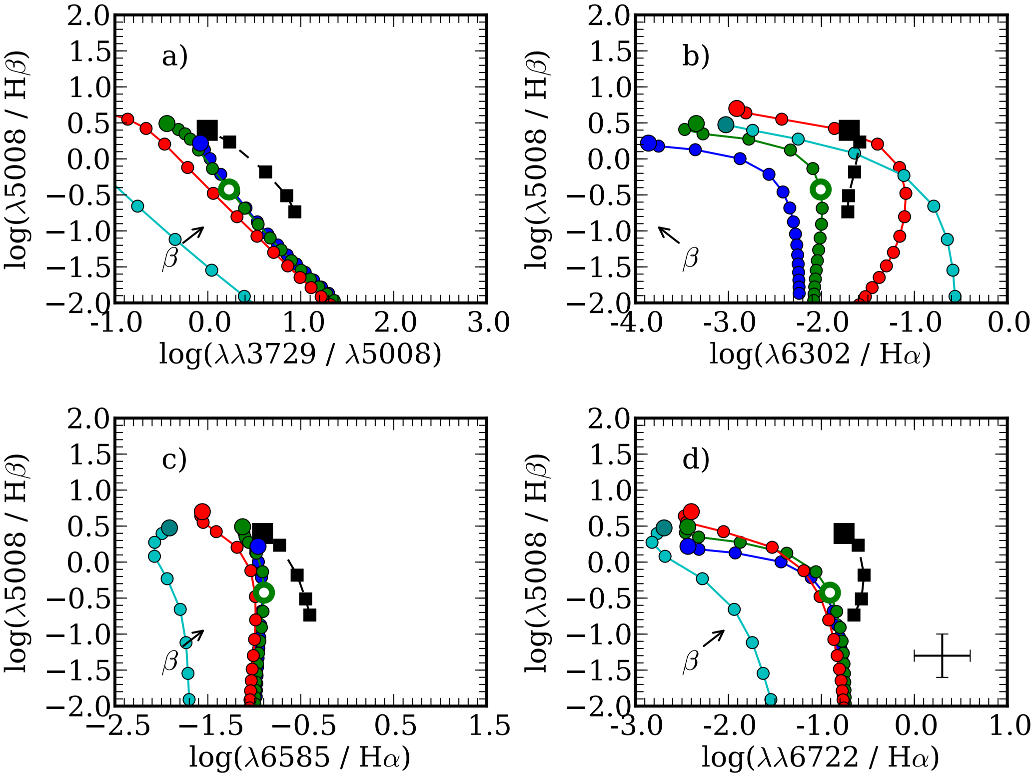

Figure 4.5 (cont'd)

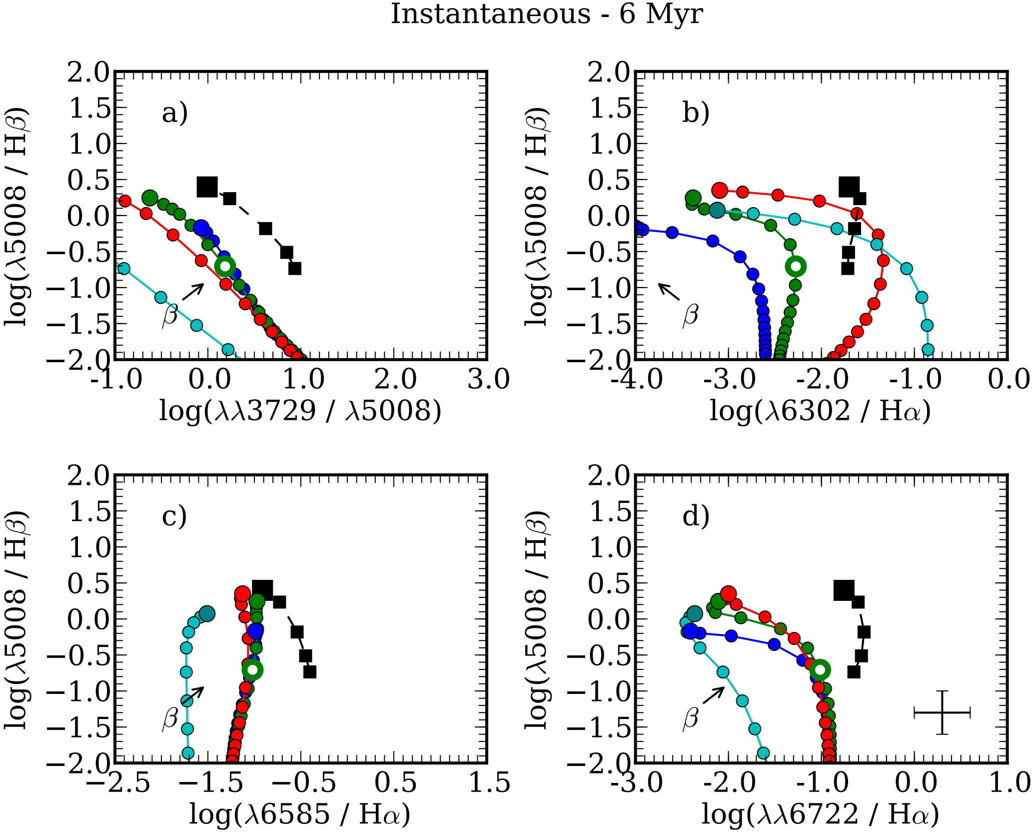

Figure 4.5 (cont'd)

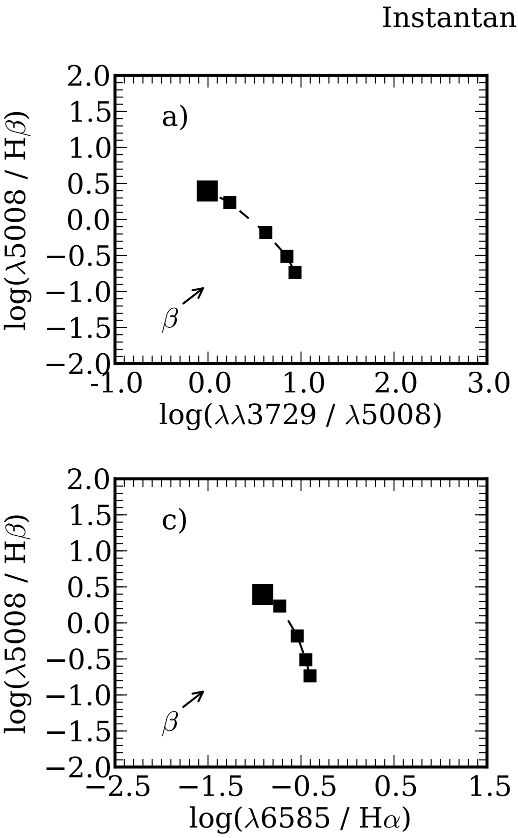

All emission line ratios slightly increase between 2 Myr and 6 Myr except for [O II] λ3727/ [O III] λ5007, which slightly decreases, and [N II] λ6584/ Hα which stays constant. Over this time interval, the Balmer emission line equivalent widths decrease faster than the maximum equivalent widths of [O III] λ5007, [S II] λ6720 and [O I] λ6300. Here, the [O II] / [O III] ratio decreases due to sharp decrease in [O II] emission at large radii. After 6 Myr, all emission line ratios stay constant since the starburst has reached equilibrium (Kewley et al. 2001), as emphasized by our 10 Myr panel in Figure 4.4a.

Figure 4.5 shows the same VO87 diagnostic diagrams as Figure 4.4a but this time for an instantaneous starburst. Between 0.1 Myr and 2 Myr, all line ratios decrease by approximately 0.2 dex except for [O III] λ5007/ Hβ and [O II] λ3727/ [O III] λ5007. In this age range, [O III] λ5007/ Hβ, on average, decreases by approximately

0.5 dex due to a sharp decrease in [O III] emission. This decrease is larger than that of [O II] λ3727 explaining why the [O II]/[O III] ratio increases between 0.1 Myr and 2 Myr.

Between 2 Myr and 6 Myr, all the emission line ratios in the VO87 diagrams decrease by ~0.2 dex due to a drastic decrease in forbidden line emission over the entire LOC plane. In contrast, the Balmer line emission also decreases, but by a substantially less amount, and the emission remains flat across the essentially the entire parameter space. Finally, as Figure 4.3b shows, at 10 Myr the starburst becomes so soft that only a negligible amount of forbidden line emission is produced. Our current best fit from the models comes from a continuous starburst (Figure 4.4) with an age of 0.1 Myr (1st quadrant). The white circle corresponds to γ = -0.5 and β = -1.4, and matches our highest ionization subset to within a factor of 2 for each of the diagrams shown.

4.4 Future Work

This thesis chapter represents a progress report for an ongoing investigation. The preliminary conclusions of this work are:

- Currently, our model that best fits the SF subsets results from a 0.1 Myr continuous starburst with a solar metallicity and LOC integration free parameters γ = -0.5 and β = -1.4
- This set of free parameters also happens to be very close to our best fit for the highest ionization AGN subset from Paper II (γ = -0.75, β = -1.4)
- We can hypothesize from both instantaneous and continuous starbursts that the variation in our subsets may not be a function of starburst age, at least for a dust-free solar metallicity model

- We can conclude, at a glance, that our main conclusion from Paper II, the radial concentration of clouds is the physical parameter responsible for the observed AGN ionization sequence, also seems to hold for our preliminary results with SF galaxies

In our preliminary analysis, we assumed that the incident radiation field originated from a star cluster with either an instantaneous or continuous SFH. We will broaden this analysis to encompass the SED from 30 Doradus (Selman et al. 1999), which results from a star cluster that undergoes three discrete periods of star formation and possesses an IMF slightly flatter than that of the Salpeter IMF (Salpeter 1955).

Here, we have also assumed that the NLR does not increase in metallicity as the starburst ages, which would be reasonable if the starburst is lighting up pre-existing gas around it. But an alternate possibility is that the NLR consists of gas produced by SNe within the starburst, in case its metallicity could evolve as the starburst ages. Our future work will include assessing the effects of starburst metallicity on the resulting LOC integrations for both SFHs. Multiple diagnostic diagrams that constrain the SED will provide insight into the incident continuum and we will include diagrams with lines as consistency checks on strong line ratios. Starbursts with lower metallicities have harder ionizing continua, making our observations of He II and Ar IV emission lines valuable due to their large ionization potential. After constraining the incident radiation field, we will also constrain the metallicity of the gas clouds by utilizing metallicity sensitive emission line ratios, in particular the [N II]/ [O II] ratio. We have standard indicators for electron temperature, [O III] λ4363/ [O III] λ5007, and low density gas, [S II] λ6716/ [S II] λ6731, but due to our large galaxy sample the [S II] λ6720/ [S II] λ4070 ratio also enables a check on any high density cloud components.

We will also examine the impact of dust grains by running dusty grids of simulations in the same manner as Paper II, as opposed to the dust-free case studied here. Photoelectric heating from grains will assist in the production of high ionization emission lines. Overall, the incorporation of dust into our models will likely have around a factor of 2 impact on the equivalent widths (Ferguson et al. 1997) and may influence the SED optimization (Richardson et al. 2013). Comparisons between dust-free and dusty models will determine whether a dust-free gas can successfully recreate the spectra seen in our subsample of starburst galaxies or whether dusty gas, as in Kewley et al. (2001) and Levesque et al. (2010), is a more accurate description.

We will search for connections between low ionization SF galaxies and low ionization AGN. In Paper II, we fit several low ionization AGN by adjusting the radial distribution of clouds, however many diagnostic ratios were not adequately fit at low ionization. Indeed, despite MFICA isolating pure sequences of AGN and SF galaxies, the small degree of cross talk between components could allow enough room for overlapping AGN and SF properties.

Finally, we will switch to running our simulations with the newest version of Cloudy (13.02; Ferland et al. 2013). This version features more robust molecular and chemistry solvers and updated atomic data. In addition, the c10.00 featured an error that caused the intensities of certain [S II] and [O II] to be incorrectly computed. This will only have a minor impact on the preliminary results presented here.

REFERENCES

REFERENCES

Abdo A. A. et al., 2011, Sci, 331, 739

Allen J. T., Hewett P. C., Richardson C. T., Ferland G. J., Baldwin J. A., 2013, MNRAS, 430, 3510

Allen M. G., Dopita M. A., Tsvetanov Z. I., 1998, ApJ, 493, 571

Allende Prieto C., Lambert D. L., Asplund M., 2001, ApJ, 556, L63

Allende Prieto C., Lambert D. L.; Asplund M., 2002, ApJ, 573, L137

Alonso-Herrero A., Rieke M. J., Rieke G. H., Shields J. C., 2000, ApJ, 532, 845

Asplund M., 2000, A&A, 359, 755

Asplund M., 2003, preprint (astro-ph/0302409)

Asplund M., Nordlund A., Trampedach R., Stein R. F., 2000, A&A, 359, 743

Atoyan A. M., Aharonian F. A., 1996, MNRAS, 278, 525

Baldwin J., Ferland G., Korista K., Verner D., 1995, ApJ, 455, L119

Baldwin J. A., Phillips M. M., Telervich R., 1981, PASP, 93, 5 (BPT)

Baldwin J. A., Ferland G. J., Martin P. G., Corbin M. R., Cota S. A., Peterson B. M., Slettebak A., 1991, ApJ, 374, 580

Baldwin J. A. et al., 1996, ApJ, 468, L115

Baldwin J. A., Hamann F., Korista K. T., Ferland G. J., Dietrich M., Warner C., 2003, ApJ, 583, 649

Binette L., Wilson A. S., Storchi-Bergmann T., 1996, A&A, 312, 365

Black J. H., van Dishoeck E. F., 1987, ApJ, 322, 412

Bottorff, M.C., Baldwin, J.A., Ferland, G.J., Ferguson, J.W., Korista, K.T. 2002, ApJ, 581, 932

Bradley L. D., Kaiser M. E., Baan W. A., 2004, ApJ, 603, 463

Bressan A., Fagotto F., Bertelli G., Chiosi C., 1993, A&AS, 100, 647

Buehler R. et al., 2012, ApJ, 749, 26

Cazaux S., Tielens, A. G. G. M., 2002, ApJ, 575, 29

Dalgarno A., Yan M., Liu W., 1999, ApJS, 125, 237

Davidson, K., 1978, ApJ, 220, 177

Davidson, K., 1979, ApJ, 228, 179

Davidson K., Fesen R. A., 1985, ARA&A, 23, 119

Dopita M. A., Sutherland R. S., 1995, ApJ, 455, 468

Dopita M. A., Sutherland R. S., 1996, ApJS, 102, 161

Dopita M. A., Groves B. A., Sutherland R. S., Binette L., Cecil G., 2002, ApJ, 572, 753

Draine, B., 2003, ApJ, 598, 1017

Duyvendak J. J. L., 1942, PASP, 54, 91

Elvis et al., 1994, ApJS, 95, 1

Fabian A. C., Johnstone R. M., Sanders J. S., Conselice C. J., Crawford C. S., Gallagher J. S. III, Zweibel E., 2008, Nat, 454, 7207

Ferguson J. W., Korista K. T., Baldwin J. A., Ferland G. J., 1997, ApJ, 487, 122 (F97)

Ferland G., 2011, in Colpi M., Gallo L., Grupe D., Komossa S., Leighly K., Mathur S., eds, Proc. Sci., Vol. NLS1, Narrow-Line Seyfert 1 Galaxies and Their Place in the Universe. SISSA, Trieste, p. 013

Ferland, G. J., Osterbrock D. E., 1986, ApJ, 300, 658

Ferland G. J., Fabian A.C., Johnstone R.M., 1994, MNRAS, 266, 399

Ferland G. J., Korista K. T., Verner D. A., Ferguson J. W., Kingdon J. B., Verner E. M., 1998, PASP, 110, 761

Ferland G. J., Fabian A. C., Hatch N. A., Johnstone R. M., Porter R. L., van Hoof P. A. M., Williams R. J. R., 2009, MNRAS, 392,1475

Ferland G. J, et al., 2013, Revista Mexicana de Astronomia y Astrosica, in press (arXiv:1302.4485)

Fesen R. A., Kirshner R. P., 1982, ApJ, 258, 1

Fesen R., Blair W. P., 1990, ApJ, 351, L45

Fesen R. A., Shull J. M, Hurford, A. P., 1997, AJ, 113, 354

Gallant Y. A., Arons J., 1994, ApJ, 435, 230

Glaccum W., Harper D. A., Loewenstein R. F., Pernic R., Low F. J., 1982, BAAS, 14, 612

Glassgold A., Langer W., 1974, ApJ, 193, 73

Gomez, H. L. et al., 2012, ApJ, 760, 96

Graham J. R., Wright G. S., Longmore A. J., 1990, ApJ, 352, 172 (G90)

Groves B. A., Dopita, M. A., Sutherland R. S., 2004, ApJS, 153, 9 (G04a)

Groves B. A., Dopita, M. A., Sutherland R. S., 2004, ApJS, 153, 75 (G04b)

Groves B. A., Heckman T. M., Kauffmann G., 2006, MNRAS, 371, 1559

Hamann F., Ferland G., 1999, ARA&A, 37, 487

Heckmann T. M., 1980, A&A, 87, 142

Hillier D., Miller D. L., 1998, ApJ, 496, 407

Hennessy G. S. et al., 1992, ApJ, 395, L13

Henney W. J., Williams R. J. R., Ferland G. J., Shaw G., O'Dell C. R., 2007, ApJ, 671, L137

Henry R. B. C., MacAlpine, G. M., 1982, ApJ, 258, 11

Hester J. J., 2008, ARA&A, 46, 127

Hester J. J., Graham J. R., Beichman C. A., Gautier T. N. III, 1990, ApJ, 357, 539

Ho L. C., Filippenko A. V., Sargent W. L. W., 1993, ApJ, 417, 63

Holt J., Tadhunter C. N., Morganti R., Emots B. H. C., 2011, MNRAS, 410, 1527

Hoshino M., Arons J., Gallant Y. A., Langdon A. B., 1992, ApJ, 390, 454

Indriolo N., Geballe T. R., Oka T., McCall B. J., 2007, ApJ, 671, 1736

Indriolo N., Fields B. D., McCall B. J., 2009, ApJ, 694, 257

Kauffmann G., et al., 2003, MNRAS, 346, 1055

Kewley L. J., Dopita M. A., Sutherland R. S., Heisler C. A., Trevena J., 2001, ApJ, 556, 121

Kewley L. J., Groves B., Kauffmann G., Heckman T., 2006, MNRAS, 372, 961

Kingdon J., Ferland G. J., Feibelman W. A., 1995, ApJ, 439, 739

Komossa S., Schulz H., 1997, A&A, 323, 31

Korista K., Baldwin J., Ferland G., Verner D., 1997, ApJS, 108, 401

Kroupa, P. 2001, MNRAS, 322, 231

Le Bourlot J., Pineau des Forets G., Roueff E., 1995, A&A, 297, 251

Levesque E., Kewley L. J., Larson K., 2010, AJ, 139, 712

Loh E. D., Baldwin J. A., Ferland G. J., 2010, ApJ, 716, L9 (Paper I)

Loh E. D., Baldwin J. A., Curtis Z. K., Ferland G. J., ODell C. R., Fabian A. C., Salomé P., 2011, ApJS, 194, 30 (Paper II)

Luridiana, V., Simón-Diaz, S., Cerviño, M., González Delgado, R.M., Porter, R.L., Ferland, G.J., 2009, ApJ, 691. 1712 Loh E. D., Baldwin J. A., Ferland G. J., Curtis Z. K., Richardson C. T., Fabian A. C., Salomé P., 2012, MNRAS, 421, 789 (Paper III)

MacAlpine, G. M., Satterfield, T. J., 2008, AJ, 136, 2152

Marsden P. L., Gillett F. C., Jennings R. E., Emerson J. P., de Jong T., Olnon F. M., 1984, ApJ, 278, L29

Mathews W. G., Ferland G. J., 1987, ApJ, 323, 456

Mayall N. U., Oort J. H., 1942, PASP, 54, 95

Miller J. S., 1973, ApJ, 180, L83

Mori K., Burrows D.N., Hester J.J., Pavlov G.G., Shibata S., Tsunemi H. 2,004, ApJ, 609, 186

Nagao T., Maiolino R., Marconi A., 2006, A&A, 447, 863
Osterbrock D. E., Ferland G. J., 2006, Astrophysics of Gaseous Nebulae & Active Galactic Nuclei, 2nd edn. University Science Press, Mill Valley, CA (AGN3)

Papadopoulos, P., 2010, ApJ 720, 226

Pequignot D., Dennefeld M., 1983, A&A, 120, 249

Pellegrini E. W., Baldwin J. A., Brogan C. L. Hanson M. M., Abel N. P., Ferland G. J., Nemala H. B., Shaw G., Troland, T. H. 2007, ApJ, 658, 1119

Richardson C. T., Baldwin, J. A. Ferland G. J., Loh E. D., Kuehn C. A., Fabian A. C., Salomé P., 2013, MNRAS, 430, 1257

Richardson C. T., Allen J. T., Baldwin J. A., Hewett P. C., Ferland G. J., 2013, MNRAS (submitted)

Salpeter E. E., 1955, ApJ, 121, 161

Sankrit R. et al., 1998, ApJ, 504, 344

Satterfield, T. J., Katz, A. M., Sibley, A. R., MacAlpine, G. M., Uomoto, A., 2012, AJ, 144, 27

Selman F., Melnick J., Bosch G., Terlevich R., 1999, A&A, 347, 532

Shaw G., Ferland G. J., Abel N. P., Stancil P. C., van Hoof P. A. M., 2005, ApJ, 624, 794

Shuder J.M., Osterbrock D.E. 1981, ApJ, 250, 55

Snijders L., Kewley L. J., van der Werf P. P., 2007, ApJ, 669, 269

Spinoglio L., Malkan M. A., 1992, ApJ, 399, 504

Spitzer L., 1978, Physical Processes in the Interstellar Medium (New York: John Wiley & Sons, Inc.)

Stasińska G., Cid Fernandes R., Mateus A., Sodré L., Asari N. V., 2006, MNRAS, 371, 972

Steffen A. T., Strateva I., Brandt W. N., Alexander D. M., Koekemoer A. M., Lehmer B. D., Schneider D. P., Vignali C., 2006, AJ, 131, 2826

Sternberg A., Neufeld, D. A., 1999, ApJ, 516, 371

Storchi-Bergmann T., Pastoriza M. G. 1990, PASP, 102, 1359

Sturm E., Lutz D., Verma A., Netzer H., Sternberg A., Moorwood A. F. M., Oliva E., Genzel R., 2002, A&A, 393, 821

Tanaka M., 2012, PASJ, 64, 36

Tanaka M., 2012, PASJ, 64, 37

Tavani M. et al., 2011, Sci, 331, 736

Temim T. et al., 2006, AJ, 132, 1610

Temim T., Sonneborn G., Dwek E., Arendt R.G., Gehrz R., Slane P., Roellig T.L., 2012, ApJ, 753, 72

Tielens A. G. G. M., 2005, The Physics and Chemistry of the Interstellar Medium, (Cambridge, UK: Cambridge University Press)

Tielens A. G. G. M., Hollenbach D., 1985, ApJ, 291, 722

Trimble V., 1968, AJ, 73, 535

Trimble V., 1973, PASP, 85, 579

Veilleux S., Osterbrock D. E., 1987, ApJS, 63, 295 (VO87)

Verner E. M., Verner D. A., Korista K. T., Ferguson J. W., Hamann F., Ferland G. J., 1999, ApJS, 120, 101

Webber W. R. 1998, ApJ, 506, 329

Wu C. C., 1981, ApJ, 245, 581

Young J. S., Scoville, N.Z., 1991, ARA&A, 29, 581

Zamorani et al., 1981, ApJ, 245, 357

Zhang Z., Liang Y., Hammer F., 2013, preprint (arXiv:1302.3013)